

# **Carbon nanotube – supported bimetallic nanocatalysts for the electro-oxidation of alcohols in alkaline media**

by

**Tendamudzimu Ramulifho**

A thesis submitted in fulfilment of the  
requirements for the degree

of

**Masters of Science**

In the Faculty of Natural and Agricultural Sciences  
Department of Chemistry  
University of Pretoria

December 2010

Supervisor: Dr. K. I. Ozoemena  
Co-supervisor: Dr. L. Van Der Merwe

## **DECLARATION**

I, Tendamudzimu Ramulifho declare that the thesis, which I hereby submit for the Masters degree in Chemistry at the University of Pretoria, is my own work and has not previously been submitted by me for a degree at this or any other tertiary institution.

SIGNATURE: ..... DATE: .....

## **DEDICATION**

To my parents

Mr Julius & Mrs Victoria Ramulifho

for your unconditional love and support

## Acknowledgements

---

### **ACKNOWLEDGEMENTS**

First, I would like to thank God for giving me strength and wisdom during the duration of my MSc studies.

I would also like to thank my supervisor, Dr Kenneth Ozoemena, for his guidance and support over the course of my MSc studies.

A special thanks to Dr Mmalewane Modibedi, for her support and advice throughout my studies.

I am grateful to Dr Liezel van der Merwe for her support.

I would like to show my gratitude to everyone at the Council of Scientific and Industrial Research (CSIR), Material Science and Manufacturing, Energy and Processes unit, for their assistance and guidance.

I would like to express my deepest appreciation to the CSIR for giving me the opportunity to be part of the Masters Studentship programme.

A special thanks to the CSIR National Centre for Nano-structured Materials for allowing me access to their characterization techniques.

Finally, I would like to thank my fiancé Livhuwani Nemusombori, for his support, encouragement, unconditional love and for always being there for me.

## ABSTRACT

An electrocatalyst plays an important role in the alcohol oxidation reaction in fuel cells. Palladium based electrocatalysts are one of the promising candidates for alcohol oxidation in direct alcohol alkaline fuel cells. This study reports the preparation of metal nanoparticles (Pd, Ni, and Sn) supported on sulfonated multi-walled carbon nanotubes (SF-MWCNTs) using a microwave-assisted solvothermal method. The physical properties of the prepared electrocatalysts were investigated using several techniques such as TEM, EDX, XRD, FTIR and Raman spectroscopy. The electrocatalytic behaviour of the SF-MWCNT-Pd and its mixtures (i.e., SF-MWCNT-PdSn<sub>mix</sub> and SF-MWCNT-PdNi<sub>mix</sub>) towards ethanol and ethylene glycol oxidation in alkaline medium were investigated. The results show that the mixed Pd-based catalysts gave better electrocatalytic activity than their alloy nanoparticles or Pd alone. The SF-MWCNT platform gave better electrocatalytic performance compared to the unsulfonated and commercial vulcan carbon. Detailed electrochemical studies (involving cyclic voltammetry, chronoamperometry, chronopotentiometry, and impedance spectroscopy) prove that the electrocatalytic oxidation of ethanol at the SF-MWCNT-PdNi<sub>mix</sub> platform is more stable, occurs at lower potential, and gives lower Tafel slopes, with faster charge-transfer

## Abstract

---

kinetics compared to its SF-MWCNT-PdSn<sub>mix</sub> counterpart. The results also revealed that SF-MWCNT-PdNi<sub>mix</sub> is more tolerant to CO poisoning than the SF-MWCNT-PdSn<sub>mix</sub> during ethanol oxidation in alkaline medium. However, the SF-MWCNT-PdSn<sub>mix</sub> electrocatalyst showed better electrocatalytic behaviour for ethylene glycol oxidation in alkaline medium; with high current response, better stability and low Tafel slopes. Both (SF-MWCNT-PdNi<sub>mix</sub> and SF-MWCNT-PdSn<sub>mix</sub>) electrocatalysts showed comparable behaviour towards CO poisoning during ethylene glycol oxidation in alkaline medium. The results obtained provide some important insights into the electrochemical response of microwave synthesised Pd-based bimetallic catalysts for potential application in direct alcohol alkaline fuel cell technology.

## Table of contents

---

<b>TABLE OF CONTENTS</b>	<b>Page</b>
Declaration	i
Dedication	ii
Acknowledgements	iii
Abstract	v
Table of Contents	vii
List of Abbreviations	xiii
List of symbols	xv
List of Figures	xvii
List of Schemes	xxv
List of Tables	xxvi
<b>Chapter One: Introduction</b>	<b>1</b>
<b>1.1</b> General Overview	<b>2</b>
<b>1.2</b> Objectives	<b>4</b>
<b>1.3</b> Thesis layout	<b>5</b>

## Table of contents

---

<b>Chapter Two:</b> Literature Review	6
<b>2.1</b> Fuel cells	7
2.1.1 Introduction	7
2.1.2 Operating Principles of Fuel Cells	8
2.1.3 Fuel Cell Electrochemistry	9
2.1.4 Fuel Cell Types	13
2.1.5 Fuel Cell applications	15
<b>2.2</b> Direct Alcohol Alkaline Fuel Cell	17
2.2.1 Introduction	17
2.2.2 Operating Principles of Direct Alcohol Alkaline Fuel Cell	20
2.2.3 Catalysts for Alcohol Oxidation in Direct Alcohol Alkaline Fuel Cells	22
2.2.4 Support Materials for Electrocatalysts	33
<b>2.3</b> Electrocatalysts Preparation Methods	36
2.3.1 Introduction	36
2.3.2 Microwave Synthetic Method	36

## Table of contents

---

<b>2.4</b>	<b>Microscopic and Spectroscopic Catalysts Characterization</b>	
	Techniques	39
2.4.1	X-ray powder Diffraction	39
2.4.2	Transmission Electron Microscopy	41
2.4.3	Energy Dispersive X-ray Spectroscopy	42
2.4.4	Raman Spectroscopy	43
2.4.5	Fourier Transform Infrared Spectroscopy	45
<b>2.5</b>	<b>Electrochemical Characterization</b>	<b>46</b>
2.5.1	Cyclic Voltammetry	50
2.5.2	Chronoamperometry	57
2.5.3	Chronopotentiometry	59
2.5.4	Linear Sweep Voltammetry	60
2.5.5	Electrochemical Impedance Spectroscopy	61
<b>2.6</b>	<b>Chemically Modified Electrodes</b>	<b>65</b>
<b>CHAPTER THREE:</b>	<b>Experimental</b>	<b>68</b>
<b>3.1</b>	<b>Introduction</b>	<b>69</b>
<b>3.2</b>	<b>Chemicals and Materials</b>	<b>71</b>
<b>3.3</b>	<b>Instrumental Conditions</b>	<b>73</b>
3.3.1	Fourier Transform Infrared Spectroscopy	73
3.3.2	Transmission Electron Microscopy	73

## Table of contents

---

3.3.3 Energy Dispersive X-ray Spectroscopy	73
3.3.4 Raman Spectroscopy	74
3.3.5 X-ray Diffraction	74
3.3.6 Electrochemical characterization conditions	75
<b>3.4</b> Functionalization of Multi-walled Carbon Nanotubes	76
3.4.1 Purification and Oxidation of the Multi-walled Carbon Nanotubes	76
3.4.2 Sulfonation of the Multi-walled Carbon Nanotubes	77
<b>3.5</b> Catalysts Syntheses	78
<b>3.6</b> Electrode Modification	80
<b>3.7</b> CO-Stripping Measurements	82
<b>CHAPTER 4: Results and Discussions</b>	83
<b>4.1</b> Spectroscopic and Microscopic Characterization	86
4.1.1 Characterization of the Multi-walled Carbon Nanotubes	86
4.1.1.1 X-ray Diffraction Analysis	86
4.1.1.2 Raman Spectroscopy Analysis	87
4.1.1.3 Fourier Transform Infrared Analysis	89
4.1.1.4 Transmission Electron Microscopy Images	91

## Table of contents

---

4.1.2	Characterization of the electrocatalysts	92
4.1.2.1	X-ray Diffraction analysis	92
4.1.2.2	Transmission Electron Microscopy Analysis	95
4.1.2.3	Energy Dispersive X-ray Analysis	97
<b>4.2</b>	<b>Electrochemical Characterization</b>	<b>100</b>
4.2.1	The Effect of the Support on the Catalytic Performance	100
4.2.2	The Effect of the Method of Preparing the Bi-metallic Electrocatalysts	101
4.2.3	Electrochemically Active surface Area Determination	104
<b>4.3</b>	<b>Electrocatalysis towards Ethanol Oxidation in Alkaline Medium</b>	<b>111</b>
4.3.1	Comparative Electrocatalytic Oxidation of Ethanol in Alkaline Medium	112
4.3.2	Long - Term Stability Curves of the Electrocatalysts	116
4.3.3	Chronopotentiometric Analysis on the Electrocatalysts	118
4.3.4	The Effect of Carbon Monoxide Poisoning during Ethanol Oxidation	119
4.3.5	The Effect of the Sweep Rate on the Current Density	121
4.3.6	Tafel Analysis	123
4.3.7	Electrochemical Impedance Analysis	126

## Table of contents

---

4.3.8 Effect of Varying the Concentration of KOH or Ethanol on the Voltammetric Behaviour	131
<b>4.4</b> Electrocatalysis towards Ethylene Glycol Oxidation in Alkaline Medium	139
4.4.1 Comparative Electrocatalytic Oxidation of Ethylene Glycol in Alkaline Medium	140
4.4.2 Long - Term Stability Curves of the Electrocatalysts	142
4.4.3 Chronopotentiometric Analysis on the Electrocatalysts	144
4.4.4 The effect of Carbon Monoxide Poisoning during Ethylene Glycol Oxidation	146
4.4.5 The Effect of the Sweep Rate on the current density	147
4.4.6 Tafel Analysis	149
4.4.7 Electrochemical Impedance Spectroscopy Analysis	151
4.4.8 Effect of varying the Concentration of the KOH or Ethylene Glycol on the Voltammetric Behaviour	156
<b>CHAPTER FIVE:</b> Conclusions and Recommendations	165
<b>CHAPTER SIX:</b> References	170
<b>Appendix:</b> Oral and poster presentations resulting from this thesis	193

## **LIST OF ABBREVIATIONS**

A	=	Electrode surface area
AFC	=	Alkaline fuel cell
Ag/AgCl	=	Silver/silver chloride reference electrode
CA	=	Chronoamperometry
CE	=	Counter Electrode
CHP	=	Combined Heat and Power
CME	=	Chemically Modified Electrode
CNT	=	Carbon Nanotube
CPE	=	Constant Phase Element
CV	=	Cyclic Voltammetry
CV	=	Cyclic Voltammogram
DAAFC	=	Direct Alcohol Alkaline Fuel Cell
EASA	=	Electro – Active Surface Area
EDX	=	Energy-Dispersive X-Ray
EG	=	Ethylene Glycol
EIS	=	Electrochemical Impedance Spectroscopy
EOR	=	Ethanol Oxidation Reaction
EtOH	=	Ethanol
FC	=	Fuel Cell
FTIR	=	Fourier Transform Infrared

## List of abbreviations

---

GCE	=	Glassy Carbon Electrode
IMH	=	Intermittent Microwave Heating
IR	=	Infra-Red
LSV	=	Linear Sweep Voltammetry
MOFC	=	Molten Carbonate Fuel Cell
MWAS	=	Microwave – Assisted Solvothermal Synthesis
MWCNT	=	Multi-Walled Carbon Nanotube
PAFC	=	Phosphoric Acid Fuel Cell
PEMFC	=	Proton Exchange Membrane Fuel Cell
$R_{ct}$	=	Charge transfer resistance
RE	=	Reference Electrode
$R_s$	=	Solution Resistance
SOPC	=	Solid Oxide Fuel Cell
SWCNT	=	Single –Walled Carbon Nanotubes
TEM	=	Transmission Electron Microscopy
UV	=	Ultraviolet
Vis	=	Visible
WE	=	Working Electrode
XRD	=	X-ray Diffraction
$Z_{im}$	=	Imaginary impedance
$Z_{re}$	=	Real impedance
$Z_w$	=	Warburg Impedance

## **LIST OF SYMBOLS**

$\alpha_A$	=	Transfer coefficient for the anodic reaction
$\alpha_C$	=	Transfer coefficient for the cathodic reaction.
$\lambda$	=	Wavelength
$C$	=	Molar concentration of analyte
$C$	=	Capacitance
$C_{dl}$	=	Double-layer capacitance
$D$	=	Diffusion coefficient
$E$	=	Potential
$E_i$	=	Starting potential
$E_f$	=	Final potential
$E_p$	=	Peak potential
$E_{pa}$	=	Anodic peak potential
$E_{pc}$	=	Cathodic peak potential
$E_e$	=	Equilibrium potential
$E^{\circ}$	=	Standard potential
$E^{\circ'}$	=	Formal redox potential
$f$	=	Frequency
$F$	=	Faraday constant
$h$	=	Plank's constant
Hz	=	Hertz

## List of symbols

---

$i_{pa}$	=	Anodic peak current
$i_{pc}$	=	Cathodic peak current
$j$	=	standard exchange current
$j_0$	=	standard exchange current
$I_{pa}$	=	Anodic peak current
$I_{pc}$	=	Cathodic peak current
$K$	=	Kelvin
$n$	=	Number of electron
$\eta$	=	Over potential
$[O_x]$	=	The bulk concentration of the oxidizing species
$r$	=	Radius of electrode
$R$	=	Universal gas constant
$[R_{ed}]$	=	The bulk concentration of the reducing species
$T$	=	Temperature (K)
$v$	=	Scan rate
$V$	=	Volts

## **LIST OF FIGURES**

Figure 2.1:	Schematic diagram of a hydrogen fuelled fuel cell	<b>9</b>
Figure 2.2:	Schematic diagram of a direct alcohol alkaline fuel cell	<b>21</b>
Figure 2.3:	Conceptual diagram of (a) SWCNT and (b) MWCNT	<b>34</b>
Figure 2.4:	Anton Paar 3000 microwave system	<b>37</b>
Figure 2.5:	Schematic diagram of X-rays diffraction in a crystalline material	<b>40</b>
Figure 2.6:	Raman spectrum of (A) synthesized MWCNT, (B) N <sub>2</sub> + Ar plasma treated MWCNTs	<b>44</b>
Figure 2.7:	A diagram if (a) The simplest experimental setup for performing electrochemical experiments, (b) A Schematic representation of a three electrode potentiostat	<b>47</b>
Figure 2.8:	Schematic representation of the three modes of mass transport	<b>49</b>
Figure 2.9:	Potential-time excitation signal in cyclic voltammetric experiment	<b>50</b>
Figure 2.10:	Typical cyclic voltammogram for a reversible	

## List of figures

---

Process	<b>51</b>
Figure 2.11: A potential wave form depicting Chronoamperometry	<b>57</b>
Figure 2.12: Typical linear potential sweep and resulting $i$ -E curve	<b>60</b>
Figure 2.13: Sinusoidal Current Response in a Linear System	<b>62</b>
Figure 2.14: Nyquist plot of a Randles Cell	<b>63</b>
Figure 2.15: Modified Randles equivalent circuit	<b>64</b>
Figure 3.1: Schematic diagram of a modified GCE electrode	<b>81</b>
Figure 4.1: Comparative XRD patterns of (a) MWCNT, AF-MWCNT and (c) SF-MWCNT	<b>86</b>
Figure 4.2: Raman spectra of MWCNT, AF-MWCNT and SF-MWCNT	<b>88</b>
Figure 4.3: FTIR spectra of MWCNT, AF-MWCNT and SF-MWCNT	<b>90</b>
Figure 4.4: TEM images of (a) MWCNTs, (b) AF-MWCNTs and (c) SF-MWCNTs	<b>91</b>
Figure 4.5: Comparative XRD patterns of SF-MWCNT-Pd, SF- MWCNT-Ni and SF-MWCNT-Sn	<b>93</b>
Figure 4.6: Comparative TEM images of SF-MWCNT-Pd, SF-MWCNT-Ni and SF-MWCNT-Sn	<b>96</b>

## List of figures

---

- Figure 4.7: EDX patterns of SF-MWCNT-Pd, SF-MWCNT-Ni and SF-MWCNT-Sn **98**
- Figure 4.8: Cyclic voltammograms of C-PdSn, AF-MWCNT-PdSn and SF-MWCNT-PdSn in 0.5 M KOH + 0.5 M ethanol solutions **101**
- Figure 4.9: Cyclic voltammograms of C-PdSn, AF-MWCNT-PdSn and SF-MWCNT-PdSn in 0.5 M KOH + 0.5 M ethanol solutions **103**
- Figure 4.10: Cyclic voltammograms of SF-MWCNT-Pd, SF-MWCNT-PdNi<sub>mix</sub> and SF-MWCNT-PdSn<sub>mix</sub> in 0.5 M KOH solution **105**
- Figure 4.11: CO Stripping voltammograms of SF-MWCNT-PdNi<sub>mix</sub> and SF-MWCNT-PdSn<sub>mix</sub> in 0.5 M KOH solution **108**
- Figure 4.12: Cyclic voltammograms of SF-MWCNT-Pd, SF-MWCNT-PdNi<sub>mix</sub> and SF-MWCNT-PdSn<sub>mix</sub> in 0.5 M KOH solution **112**
- Figure 4.13: Chronoamperometric curves of SF-MWCNT-Pd, SF-MWCNT-PdSn<sub>mix</sub> and SF-MWCNT-PdNi<sub>mix</sub> in 0.5 M ethanol + 0.5 M KOH aqueous solutions at a fixed potential of -0.2 V **117**

## List of figures

---

- Figure 4.14: Chronopotentiometric curves of SF-MWCNT-Pd, SF-MWCNT- PdSn<sub>mix</sub> and SF-MWCNT- PdNi<sub>mix</sub> in 0.5 M ethanol + 0.5 M KOH aqueous solutions at (a) 1 mA cm<sup>-2</sup> and (b) 3 mA cm<sup>-2</sup> **118**
- Figure 4.15: Comparison of the influence of CO on SF-MWCNT PdSn<sub>mix</sub> and SF-MWCNT- PdNi<sub>mix</sub> electrodes in 0.5 M ethanol + 0.5 M KOH aqueous solutions in the presence and absence of saturated CO **120**
- Figure 4.16: CVs of (a) SF-MWCNT-Pd, (b) SF-MWCNT-PdNi<sub>mix</sub> and (c) SF-MWCNT-PdSn<sub>mix</sub> in 0.5 M KOH + 0.5M EtOH solutions at different scan rates **122**
- Figure 4.17: Dependence of the peak current density obtained from the forward CV scan on the scan rate in 0.5 M KOH + 0.5 M ethanol solutions on SF-MWCNT-Pd, SF-MWCNT- PdNi<sub>mix</sub> and SF-MWCNT-PdSn<sub>mix</sub> electrocatalysts **123**
- Figure 4.18: (a) A quasi-steady-state curve of ethanol oxidation on the SF-MWCNT-Pd, SF-MWCNT-PdNi<sub>mix</sub> and SF-MWCNT- PdSn<sub>mix</sub> electrocatalysts in 0.5 M KOH + 0.5 M ethanol solutions. (b) The Tafel plot of ethanol oxidation on the SF-MWCNT-Pd, SF-MWCNT-PdNi<sub>mix</sub> and SF-MWCNT-PdSn<sub>mix</sub> electrocatalysts in 0.5 M KOH + 0.5 M ethanol solutions. **125**

## List of figures

---

- Figure 4.19: Nyquist plots obtained during the oxidation of the ethanol oxidation at (a) SF-MWCNT-Pd, (b) SF-MWCNT-PdNi<sub>mix</sub> and (c) SF-MWCNT-PdSn<sub>mix</sub> electrodes and (d) is the equivalent circuit used in fitting the electrochemical impedance circuit **127**
- Figure 4.20: The bode plots (log Z (a), phase angle (b) vs log f) obtained for the SF-MWCNT-Pd, SF-MWCNT-PdNi<sub>mix</sub> and SF-MWCNT-PdSn<sub>mix</sub> electrodes in 0.5 M KOH + 0.5 M ethanol solutions at different potentials **128**
- Figure 4.21: Linear sweep voltammograms and Tafel plots for ethanol oxidation reaction on the SF-MWCNT-PdNi<sub>mix</sub> and SF-MWCNT-PdSn<sub>mix</sub> electrodes in 0.5 M KOH solution containing ethanol solutions of various concentrations **132**
- Figure 4.22: The log - log plot of current density vs ethanol concentration in 0.5 M KOH obtained at different potentials on SF-MWCNT-PdNi<sub>mix</sub> and SF-MWCNT-PdSn<sub>mix</sub> electrocatalysts **134**
- Figure 4.23: Linear sweep voltammograms and Tafel plots of ethanol oxidation reaction on the SF-MWCNT-PdNi<sub>mix</sub> and SF-MWCNT-PdSn<sub>mix</sub> electrocatalysts in 0.5 M EtOH solution containing KOH solutions of various concentrations **136**
-

## List of figures

---

- Figure 4.24: The log-log plot of the current density vs KOH concentration in 0.5 M EtOH obtained at different potentials on SF-MWCNT-PdNi<sub>mix</sub> and SF-MWCNT-PdSn<sub>mix</sub> electrocatalysts **138**
- Figure 4.25: Cyclic voltammograms of SF-MWCNT-PdNi<sub>mix</sub> and SF-MWCNT-PdSn<sub>mix</sub> in 0.5 M KOH + 0.5 M EG solutions **141**
- Figure 4.26: Chronoamperometric curves of SF-MWCNT-Pd, SF-MWCNT-PdSn<sub>mix</sub> and GCE-SF-MWCNT-PdNi<sub>mix</sub> in 0.5 M EG + 0.5 M KOH aqueous solutions at a fixed potential of -0.2 V **143**
- Figure 4.27: Chronopotentiometric curves of SF-MWCNT-Pd, SF-MWCNT-PdSn<sub>mix</sub> and SF-MWCNT-PdNi<sub>mix</sub> in 0.5 M ethanol + 0.5 M KOH aqueous solutions at (a) 1 mA cm<sup>-2</sup> and (b) 3 mA cm<sup>-2</sup> **144**
- Figure 4.28: Comparison of the influence of CO on SF-MWCNT-PdSn<sub>mix</sub> and SF-MWCNT-PdNi<sub>mix</sub> electrodes in 0.5 M ethanol + 0.5 M KOH aqueous solutions in the presence and absence of saturated CO **147**

## List of figures

---

- Figure 4.29: CVs of (a) SF-MWCNT-Pd, (b) SF-MWCNT-PdNi<sub>mix</sub> and (c) SF-MWCNT-PdSn<sub>mix</sub> in 0.5 M KOH + 0.5M EG solutions at different scan rates **148**
- Figure 4.30: Dependence of the peak current density obtained from the forward CV scan on the scan rate in 0.5 M KOH + 0.5 M EG solutions on SF-MWCNT-Pd, SF-MWCNT-PdNi<sub>mix</sub> and SF-MWCNT-PdSn<sub>mix</sub> electrocatalysts **149**
- Figure 4.31: (a) A quasi-steady-state curve of the ethanol oxidation on the SF-MWCNT-Pd, SF-MWCNT-PdNi<sub>mix</sub> and SF-MWCNT-PdSn<sub>mix</sub> electrocatalysts in 0.5 M KOH + 0.5 M EG solutions. (b) The Tafel plot of the ethanol oxidation on the SF-MWCNT-Pd, SF-MWCNT-PdNi<sub>mix</sub> and SF-MWCNT-PdSn<sub>mix</sub> electrocatalysts in 0.5 M KOH + 0.5 M EG solutions. **150**
- Figure 4.32: Nyquist plots obtained during the oxidation of the ethanol oxidation at (a) SF-MWCNT-Pd, (b) SF-MWCNT-PdNi<sub>mix</sub> and (c) SF-MWCNT-PdSn<sub>mix</sub> electrodes and (d) is the equivalent circuit used in fitting the electrochemical impedance circuit **152**
- Figure 4.33: The bode plots (log Z (a), phase angle (b) vs log f) obtained for the SF-MWCNT-Pd, SF-MWCNT-PdNi<sub>mix</sub> and

## List of figures

---

- SF-MWCNT-PdSn<sub>mix</sub> electrodes in 0.5 M KOH + 0.5 M EG solutions at different potentials **153**
- Figure 4.34: Linear sweep voltammograms and Tafel plots for ethanol oxidation reaction on the SF-MWCNT-PdNi<sub>mix</sub> and SF-MWCNT-PdSn<sub>mix</sub> electrodes in 0.5 M KOH solution containing EG solutions of various concentrations **157**
- Figure 4.35: The log – log plot of current density vs EG concentration in 0.5 M KOH obtained at different potentials on SF-MWCNT-PdNi<sub>mix</sub> and SF-MWCNT-PdSn<sub>mix</sub> electrocatalysts **159**
- Figure 4.36: Linear sweep voltammograms and Tafel plots of ethanol oxidation reaction on the SF-MWCNT-PdNi<sub>mix</sub> and SF-MWCNT-PdSn<sub>mix</sub> electrocatalysts in 0.5 M EG solution containing KOH solutions of various concentrations **161**
- Figure 4.37: The log-log plot of the current density vs KOH concentration in 0.5 M EG obtained at different potentials on SF-MWCNT-PdNi<sub>mix</sub> and SF-MWCNT-PdSn<sub>mix</sub> electrocatalysts **164**

## **LIST OF SCHEMES**

- Scheme 1: Schematic of the preparation SF-MWCNT-M (M = Pd, Ni or Sn) electrocatalysts using fast microwave-assisted method **78**
- Scheme 2: Schematic of the preparation of the two methods of preparing bi-metallic electrocatalysts **102**
- Scheme 3: Schematic diagram of the overall mechanism of EG oxidation in alkaline media **139**

## **LIST OF TABLES**

Table 2.1: Summary of major differences of FC types	<b>14</b>
Table 2.2: Typical fuel cell applications	<b>16</b>
Table 2.3: Summary of work that has been done on alcohol oxidation in alkaline medium	<b>28</b>
Table 2.4: The diagnostic criteria to cyclic voltammetric processes	<b>56</b>
Table 3.1: List of used chemical and materials	<b>71</b>
Table 4.1: Composition of the prepared electrocatalysts	<b>99</b>
Table 4.2: Electrochemically active surface area of the catalysts	<b>107</b>
Table 4.3: Comparison of the electrochemical performances of ethanol oxidation on the SF-MWCNT-Pd, SF-MWCNT-PdSn <sub>mix</sub> and GCE-SF-MWCNT-PdNi <sub>mix</sub> nanocomposites measured in 0.5 M ethanol + 0.5 M KOH solutions	<b>116</b>
Table 4.4: Impedimetric data for ethanol oxidation on the SF-MWCNT-Pd, SF-MWCNT-PdSn <sub>mix</sub> and SF-MWCNT-PdNi <sub>mix</sub> electrodes measured in 0.5 M ethanol + 0.5 M KOH solutions	<b>130</b>

## List of tables

---

- Table 4.5: Tafel slopes of the SF-MWCNT-PdNi<sub>mix</sub> and SF-MWCNT-PdSn<sub>mix</sub> electrocatalysts at 0.5 M KOH and different ethanol concentrations **133**
- Table 4.6: Reaction orders with respect to OH<sup>-</sup> and EtOH for SF-MWCNT-PdNi<sub>mix</sub> and SF-MWCNT-PdSn<sub>mix</sub> electrocatalysts **135**
- Table 4.7: Tafel slopes of the electrocatalysts at constant 0.5 M EtOH and various KOH concentrations **137**
- Table 4.8: Comparison of the electrochemical performances of ethylene glycol on the SF-MWCNT-Pd, SF-MWCNT-PdSn<sub>mix</sub> and SF-MWCNT-PdNi<sub>mix</sub> electrodes measured in 0.5 M EG + 0.5 M KOH solutions **142**
- Table 4.9: Impedimetric data for ethanol oxidation on SF-MWCNT-Pd, SF-MWCNT-PdSn<sub>mix</sub> and SF-MWCNT-PdNi<sub>mix</sub> measured in 0.5 M ethylene glycol + 0.5 M KOH solutions **155**
- Table 4.10: Tafel slopes of the SF-MWCNT-PdNi<sub>mix</sub> and SF-MWCNT-PdSn<sub>mix</sub> electrocatalysts at 0.5 M KOH and different ethylene glycol concentrations **158**
- Table 4.11: Reaction orders with respect to OH<sup>-</sup> and EG for SF-MWCNT-PdNi<sub>mix</sub> and SF-MWCNT-PdSn<sub>mix</sub> electrocatalysts **160**
- Table 4.12: Tafel slopes of the electrocatalysts at constant 0.5 M EG and various KOH concentrations **163**
-

# **CHAPTER ONE**

## **INTRODUCTION**

# 1 INTRODUCTION

## 1.1 General Overview

Energy in the form of electricity has become one of the basic needs of life. The world population keeps increasing resulting in extensive use of our primary source of energy, fossil fuels. This is causing the fossil fuels to deplete at a rapid rate and has negative environmental impacts. The urgent need to move towards environmental friendly and efficient power production has given scientists the opportunity to research and develop alternative power sources. Electrochemical energy conversion systems are considered to be the most suitable power source for portable electronic applications such as mobile phones, digital cameras and laptops [1, 2].

Fuel cells (FCs) are one of the electrochemical energy conversion systems that have received enormous interest. Much work has been done on direct alcohol fuel cells operating in acidic medium. However, less studies has been done on direct alcohol fuel cells (DAFCs) operating in alkaline medium. The alkaline medium enables the use of less expensive non-platinum electrocatalysts, non-noble metals and enhances activity of the catalysts [3,4]. However, the success of developing an efficient direct alcohol alkaline fuel cell (DAAFC) is

## Chapter 1: Introduction

---

determined by the performance of its components namely: the anodic and cathodic electrocatalysts and the membrane.

This project describes the experimental design, synthesis, and investigation of structural properties and electrochemical behaviour of the Palladium supported on sulfonated multi-walled carbon nanotubes (Pd/SF-MWCNTs), Palladium/Nickel supported on multi-walled carbon nanotubes (PdNi/SF-MWCNTs) and Palladium/Tin supported on multi-walled carbon nanotubes (PdSn/SF-MWCNTs) electrocatalysts as potential anode electrocatalysts for alcohols oxidation in DAAFC.

## Chapter 1: Introduction

---

### 1.2 Objectives

The objectives of the research project are as follows:

- (i) To identify Palladium-based bimetallic (Pd-M) electrocatalysts for the electro-oxidation of alcohols in Direct Alcohol Alkaline Fuel Cell (DAAFC)
- (ii) To synthesise Pd, Ni and Sn electrocatalysts supported on multi-walled carbon nanotubes,
- (iii) To investigate the structural properties of Pd/SF-MWCNT, PdSn/SF-MWCNT and PdNi/SF-MWCNT electrocatalysts using spectroscopic and microscopic techniques, and
- (iv) To investigate the electrocatalytic behaviour of Pd/SF-MWCNT, PdSn/SF-MWCNT and PdNi/SF-MWCNT electrocatalysts towards ethanol (EtOH) and ethylene glycol (EG) oxidation in alkaline medium.

## Chapter 1: Introduction

---

### **1.3 Thesis layout**

Chapter one gives a general overview of the project and outlines the research carried out in this thesis. The background and research that have been done on FC, DAAFC, support materials and characterization techniques are presented in chapter two. Chapter three presents the experimental section. Chapter four provides the results and discussion of the structural and electrochemical studies. Chapter five presents the concluding remarks on the overall study with suggestions on future studies. Chapter six presents the list of reference materials used.

## **CHAPTER TWO**

### **LITERATURE REVIEW**

## 2 LITERATURE REVIEW

### 2.1 Fuel Cell

#### 2.1.1 Introduction

A fuel cell is an electrochemical energy conversion system. It converts the chemical energy from a fuel directly into electrical energy [5]. A fuel cell does not have any internal moving parts and its operation can be compared with that of a battery. However, a battery is only able to store energy for a while whereas a fuel cell is able to produce electricity continuously as long as it is supplied with the fuel and an oxidant [6]. A fuel cell has three main components, namely; an ion conducting electrolyte, a cathode and an anode [7]. The ion conducting electrolyte is situated at the heart of a fuel cell and is squeezed between the anode and cathode which are coated with the electrocatalyst [8]. The function of the ion conducting electrolyte is to allow ions to migrate across it and also serves as a barrier for gas diffusion [7]. Christian Frierich Schonbein, Professor at the University of Baíe, discovered the principle of the fuel cell from 1829-1868. In 1839, Sir William Grove, a British lawyer and physicist, created the first cell type based on reversing the electrolysis of water [9]. Since then, a lot of advances has been made on fuel cells.

## Chapter 2: Literature review

---

### **2.1.2 Operating principles of fuel cells**

Electrochemical reactions occur within the fuel cell as it is an electrochemical cell. During its operation, electrochemical reactions occur at the surface of the electrocatalyst at the interface between the electrolyte and the membrane [8]. A variety of fuels can be used such as hydrogen. In hydrogen fuelled fuel cell (Figure 2.1), the hydrogen fuel is allowed to flow into the anode where the electrocatalyst particles present in the anode helps to oxidize the hydrogen into protons and electrons. The ion conducting electrolyte allows only protons to pass to the cathode. The electrons movements occurs around the electrolyte and through an external circuit to the cathode, thus producing electric current that can be used to do work such as to powering a laptop. At the cathode, the electrocatalyst particles help the oxygen to react with electrons taken from the electrode and the hydrogen ions from the electrolyte forming water [10].

## Chapter 2: Literature review

---

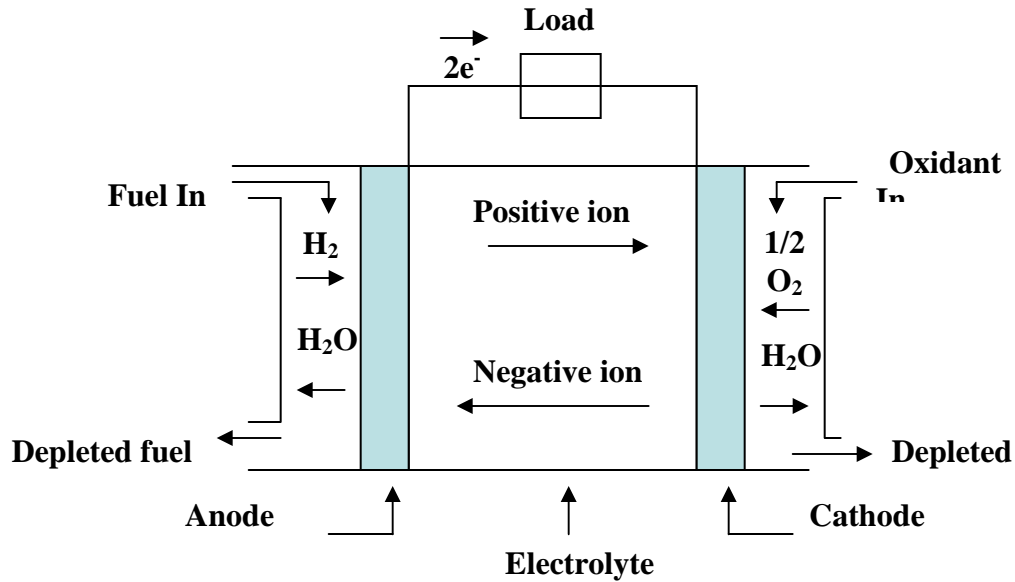


**Figure 2.1:** Schematic diagram of a hydrogen fuelled fuel cell [5]

### 2.1.3 Fuel cell electrochemistry

A fuel cell is governed by electrochemical reactions and involves charge transfer reactions. Equations 2.1 and 2.2 show the two main reactions that can occur, which involves either the oxidation or the reduction of species [8]:



where  $O_x$  = Oxidized species,  $R_{ed}$  = reduced species and  $n$  = number of electrons transferred.

## Chapter 2: Literature review

---

The oxidation and reduction reactions occur at equal rates for an electrode at equilibrium with no external current generated. The general charge transfer reaction is given by equation 2.3



The Nernst equation (equation 2.4) governs an electrochemical reaction that occurs at equilibrium conditions with no external current generated.

$$E_e = E^0 + \frac{RT}{nF} \ln \frac{[O_x]}{[R_{ed}]} \quad (2.4)$$

where  $E_e$  = equilibrium potential;  $E^0$  = standard potential of the reaction;  $F$  = Faraday's constant ( $96485 \text{ C mol}^{-1}$ );  $[O_x]$  and  $[R_{ed}]$  = the bulk concentrations of the reaction species.

Mixed potential and parasitic processes can cause a fuel cell to have a voltage lower than the thermodynamic value even at equilibrium conditions [11]. This behaviour results in an open circuit voltage lower than that of the Nernst value.

## Chapter 2: Literature review

---

When a cell is performing an electrical work, an overpotential ( $\eta$ ) occurs due to a deviation in voltage from the open circuit voltage when the current is flowing through the cell. The finite rate of the reaction at the electrodes normally causes the deviation of the potential from the equilibrium value [11].

The electrical current observed on the electrode during an electrochemical experiment is dependent on the electrode potential. This dependence can be described by the Butler-Volmer equation (2.5) which is one of the fundamental relationships in fuel cell electrochemistry. The Butler-Volmer equation is fundamental to the electrode kinetics. The standard exchange current ( $i_0$ ) of a redox reaction occurring at one electrode is given by the Butler-Volmer equation [11]:

$$i = i_0 \left[ \exp\left\{\frac{(1-\alpha_A)F\eta}{RT}\right\} - \exp\left\{\frac{-\alpha_C F\eta}{RT}\right\} \right] \quad (2.5)$$

where  $i$  = standard exchange current ;  $i_0$  = standard exchange current;  $\alpha_A$  and  $\alpha_C$  = transfer coefficients for the anodic and cathodic reaction, respectively;  $\eta$  = overpotential;  $R$  = universal gas constant and  $T$  = temperature (K).

## Chapter 2: Literature review

---

The Butler-Volmer equation takes different forms depending on the electrochemical reaction occurring. It may be written as equation (2.5a) for a reversible reaction [12]:

$$i = i_0 \frac{F\eta}{RT} \quad (2.5a)$$

The Butler-Volmer equation takes this form when the reaction has low overpotential values where  $\frac{\alpha F\eta}{RT} \ll 1$  and large  $i_0$  is observed.

The Butler-Volmer equation for irreversible reactions simplifies into two equations (2.5b and 2.5c). This occurs in reactions with small  $i_0$  values and high overpotential values. Equation 2.5b applies at high  $\eta$  for oxidative (anodic) reactions where  $i_{red}$  is negligible whereas equation 2.5c applies at high  $\eta$  for reductive (cathodic) reactions where  $i_{ox}$  is negligible.

$$\ln i = \ln i_0 - \frac{(1-a)F}{RT} \eta \quad (2.5b)$$

$$\ln(-i) = \ln i_0 - \frac{\alpha F}{RT} \eta \quad (2.5c)$$

## Chapter 2: Literature review

---

Equation 2.5b and 2.5c are also known as Tafel equations for the anodic and the cathodic currents, respectively.

### **2.1.4 Fuel cell types**

One of the advantages of fuel cells is the ability to use variety of fuels, electrolyte materials and electrolyte. This makes it easy to classify them according to these components [13]. The choice of electrolyte and fuel determines the electrode reactions and the type of ions that carry the current across the electrolyte [5]. The choice of the type of fuel is influenced by the desired operating temperature of a fuel cell. Many fuel cell types are still on the development stages [14]. The table below provides an overview of the key characteristics of the main fuel cell types.

## Chapter 2: Literature review

**Table 2.1:** Summary of major differences of FC types [15]

<b>Fuel cell type</b>	<b>Operating temperature</b>	<b>Fuel type</b>	<b>Electrical efficiency</b>	<b>Application</b>
Molten Carbonate Fuel Cell (MCFC)	~ 550 – 700°C	Most hydrocarbon based fuels	~ 50 to <70 %	Large (100's of kW to mW) stationary power generation
Solid Oxide Fuel Cell (SOFC)	~ 450 – 1000°C	Most hydrocarbon based fuels	~ 45 to <70 %	Small (<1kW) to large (mW) stationary power generation
Alkaline Fuel Cell (AFC)	~ 150 – 200°C	Pure Hydrogen	~ 40 %	Space exploration
Phosphoric Acid Fuel Cell (PAFC)	~ 100 – 220°C	Pure Hydrogen	~ 35 to 40 %	Buses, trucks & large stationary applications
Proton Exchange Membrane Fuel Cell (PEMFC)	~ 80°C	Pure Hydrogen, direct methanol	~ 30 to 35 %	Passenger cars & mobile Applications

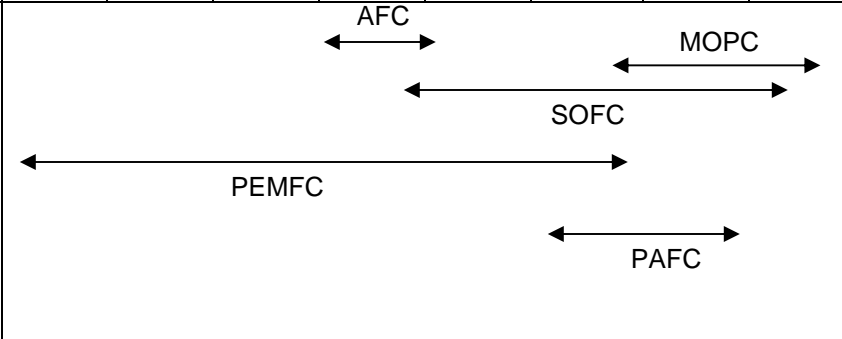
### **2.1.5 Fuel cell applications**

Fuel cells may be used in many applications with a broad range of power needs as their sizes are determined by the desired power out [16]. The power output ranges from a fraction of watt to hundreds of kilo-watts [8]. Their applications are divided into two main categories, namely; stationary or mobile applications. The stationary applications include systems such as the combined heat and power for both residential and commercial needs while the mobile applications include transportation systems and portable electronic devices [16].

Table 2.2 illustrates some typical fuel cell applications for different fuel cell types.

## Chapter 2: Literature review

**Table 2.2:** Typical fuel cell applications [10]

<b>Typical applications</b>	Portable electronics equipment			Cars, boats, and domestic CHP			Distributed power generation, CHP, and buses		
<b>Main advantages</b>	Higher energy density to batteries, faster recharging			Potential for zero emissions, higher efficiency			Higher efficiency, less pollution, quiet operation		
<b>Power (W)</b>	1	10	100	1K	10K	100K	1M	10M	
<b>Application range for fuel cell class</b>	 <p>The diagram illustrates the application ranges for five fuel cell classes across a logarithmic power scale from 1W to 10M. PEMFC covers the lowest power range (1W to 100W). AFC covers 100W to 10K. PAFC covers 100K to 1M. SOFC covers 10K to 10M. MOPC covers 100K to 10M.</p>								

Note: CHP – Combined Heat and Power

## 2.2 Direct Alcohol Alkaline Fuel Cell

### 2.2.1 Introduction

The development of direct alcohol fuel/air cells has attracted much interest during the past two decades [17]. A lot of work has focused on methanol as a fuel in order to develop a direct methanol alcohol fuel cell (DMFC) [18]. However, fundamental problems in the fuel design are making it difficult to reach the commercialization stages [19].

Below are some of the problems limiting the performances of DMFC [19]

- (i) Low electrocatalyst activity,
- (ii) The inability of the anode electrocatalyst to resist poisoning from strongly adsorbed intermediates that are formed during the methanol oxidation reaction,
- (iii) Methanol cross-over from the anode to the cathode through the Nafion® type membranes.

Researchers have gone further to find alternative low molecular weight alcohols in order to overcome these problems. The other alcohols of interest are ethanol and ethylene glycol [3]. The two alcohols stand a good chance as alternatives to methanol as they can be produced from

## Chapter 2: Literature review

---

renewable materials and are less toxic than methanol. Large amounts of ethanol can be produced from sugar containing raw materials using the fermentation process [20]. Ethylene glycol can be produced from bio-mass. Some of its advantages is its high reactivity and the ability to be easily handled [21,22].

The electrolyte membrane determines the environment in which an alcohol fuel cell can be used. The direct ethanol fuel cells (DEFCs) can be divided into two types, namely; the acid-type DEFCs and the alkaline-type DEFCs [23] . Researchers are failing to reach the commercialization stages of the acid-type DEFCs even though they show good performances [24]. The use of large amounts of platinum electrocatalyst is increasing the cost of acid-type DEFCs. The platinum electrocatalyst is susceptible to poisoning by carbon monoxide (CO) [24] . The alkaline environment in the alkaline-type DEFCs presents an opportunity to use platinum-free electrocatalysts for the alcohol oxidation and the oxygen reduction reactions; hence much interest is now on DAAFC [24]. A direct alcohol alkaline fuel cell is a type of fuel cell that uses an alcohol as a fuel operating in an alkaline medium [3]. Below are some of the advantages of operating in alkaline conditions.

## Chapter 2: Literature review

---

### **Advantages of operation in alkaline conditions: [25]**

- The ability to use both noble and non-noble metals to prepare the electrocatalysts,
- Enhanced kinetics at both electrodes with low overpotential values at the anode during the alcohol oxidation,
- Minimal alcohol crossover from the anode to the cathode side due to the electro-osmotic drag of the hydrate hydroxyl ions,
- Easier water management,
- Lower susceptibility of the materials towards corrosion due to the alkaline environment.

### 2.2.2 Operating principles of direct alcohol alkaline fuel Cells

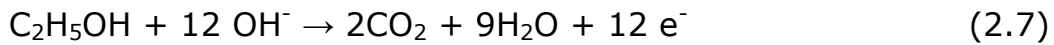
The operating principles of all fuel cell types are similar. However, the type of electrolyte determines the type of ions that will be available and mobile. This can either be protons or hydroxyl anions. In direct alcohol alkaline fuel cell the hydroxyl ( $\text{OH}^-$ ) anions are available and mobile [10]. A single DAAFC (Figure 2.2) consists of three main components like any other fuel cell. There are the anode and cathode electrodes with an alkaline electrolyte in between. The alcohol fuel (e.g. ethanol, ethylene glycol) is electrochemically oxidized at the anode electrocatalyst to produce electrons which travel through an external circuit to the cathode electrocatalyst where they react with oxygen to form water [26]. The alcohol crossover problem which is dominant in DMFC is suppressed in DAAFC. In DAAFC, the hydroxyl anions move from cathode to the anode unlike in DMFC where the protons move from the anode to the cathode making the cell more vulnerable to alcohol crossover [27].

In the direct ethanol alkaline fuel cell, the reaction of the electrons, oxygen and water at the cathode produces  $\text{OH}^-$  ions as shown by equation 2.6. The hydroxyl ions then move to the anode side through the anion exchange membrane. On the anode side they react with

## Chapter 2: Literature review

---

ethanol forming carbon dioxide, water and electrons via equation 2.7 [28].



The net reaction is given by equation 2.8

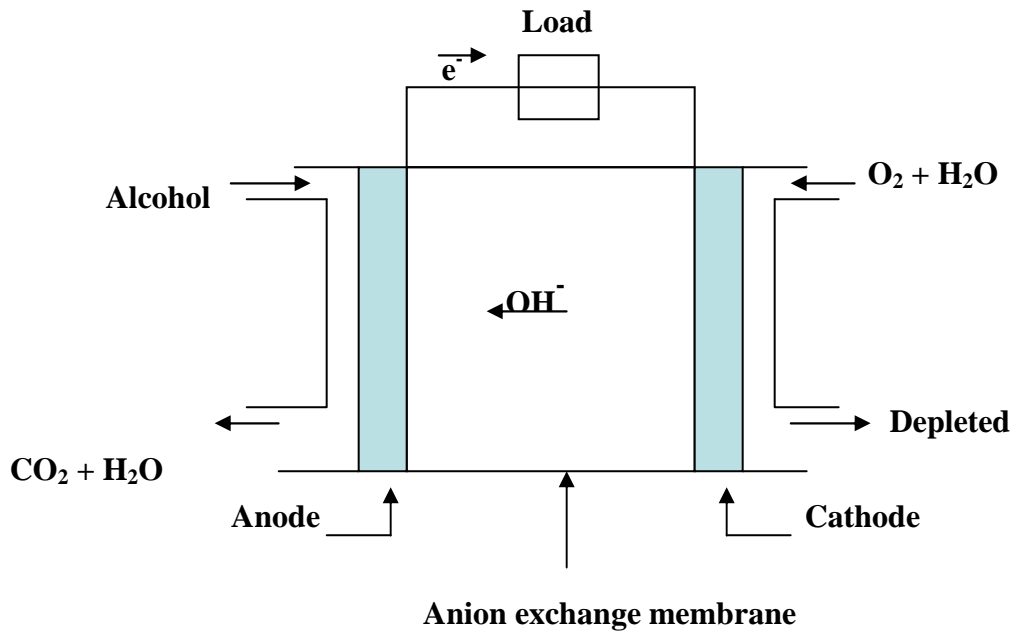


**Figure 2.2:** Schematic diagram of a direct alcohol alkaline fuel cell

### **2.2.3 Catalysts for alcohol oxidation in direct alcohol alkaline fuel cells**

An electrocatalyst is one of the most important components in a fuel cell. An electrocatalyst is a substance that is able to speed up the rate of an electrochemical reaction and is retained after the reaction. It provides a different pathway to the electrochemical reaction with lower activation energy [29]. The performance of a fuel cell or a fuel cell system is dependent on the activity of the anode and cathode electrocatalysts [30]. The activity of the electrocatalyst is dependent on the materials used in developing the electrocatalyst. The nature and structure of the electrode material also play a vital role in the adsorption and electro-oxidation of most organic fuels [19]. It is important to use materials which are compatible with each other when developing the electrode [30].

The current DAFC system is highly dependent on platinum based electrocatalysts. However, the platinum and platinum based electrocatalysts are only stable in acidic conditions. It has been shown that the performances of alcohol oxidation in alkaline medium are much better than in acidic medium and the alkaline environment offers a wider choice of metals to use to prepare the electrocatalyst [4, 31].

## Chapter 2: Literature review

---

Palladium seems to be one of the promising metals for applications in direct alcohol fuel cell. Research has shown that palladium is more abundant in the earth's crust than platinum and gold [4]. It can oxidize a large variety of alcohols in an alkaline environment and is more active for the ethanol oxidation reaction (EOR) in alkaline medium [3,25]. Its activity towards ethanol oxidation is higher compared to that of the platinum electrocatalyst [32].

Mazumder and Sun [33] reported an oleylamine-mediated synthesis of monodispersed Pd nanoparticles for catalytic oxidation of formic acid under fuel cell reaction conditions. They produced Pd nanoparticles with  $\sim 40\%$  greater surface area and four times as stable than the commercially available Pd particles. They used weak binding amino ligands to keep the palladium nanoparticles separate and at the same size as they're attached to the carbon platform. They were able to increase the available area on the platform and raised the efficiency of the reaction by keeping the particles separate and uniform [33].

It is believed that the activity of the electrocatalyst can be enhanced by using two or three metals when preparing the electrocatalyst to form a binary or a ternary electrocatalyst. The work done by Chen *et al.* [4] have shown a negative shift of ca. 0.15 V on the onset potential

## Chapter 2: Literature review

---

due to the incorporation of Ru and Au on a Pd electrocatalyst. The Pd-Ru electrocatalyst showed a high activity towards ethanol oxidation with a current density which was four times higher than that of Pt-Ru electrocatalyst in the range of 0.3 – 0.4 V [4]. They also showed the feasibility of obtaining anodic currents during the alcohol oxidation in alkaline medium at potentials higher than 0.6 V (RHE) using an Au electrocatalyst. Their results showed an activity sequence of ethanol > ethylene glycol > methanol towards alcohol oxidation on the Pd electrocatalyst when comparing the current density at the same potential. The activity sequence on the Pd-Ru electrocatalyst was found to be as follows: ethanol > ethylene glycol > methanol [4]. The Pd-Ru electrocatalyst with an atomic ratio of 1:1 showed the best activity.

Shen and Xu [34] investigated the electro-oxidation of methanol, ethanol, glycerol and ethylene glycol on  $\text{CeO}_2$ ,  $\text{Co}_3\text{O}_4$ ,  $\text{Mn}_3\text{O}_4$ ,  $\text{Mn}_3\text{O}_4$  and NiO promoted Pd/C electrocatalyst in alkaline media by cyclic voltammetry (CV), chronopotentiometry (CP) and electrochemical impedance spectroscopy (EIS) [34]. Their results showed that the Pd/C electrocatalyst promoted with nanocrystalline oxides such as  $\text{CeO}_2$ ,  $\text{Co}_3\text{O}_4$ ,  $\text{Mn}_3\text{O}_4$ ,  $\text{Mn}_3\text{O}_4$  and NiO are superior to the Pt-based electrocatalyst in terms of the activity and the CO poisoning

## Chapter 2: Literature review

---

resistance. The activity towards ethanol oxidation was higher compared to that of methanol oxidation in alkaline medium. Their work showed that the addition of nanocrystalline oxides into the Pd/C electrocatalyst immensely improved the reaction kinetics of the ethanol oxidation reaction. This was manifested by a negative shift on the onset potential of 300 mV on the Pd-NiO/C electrocatalyst during ethanol electro-oxidation when compared with that of the Pt/C electrocatalyst under the same experimental conditions.

The oxides are believed to form  $\text{OH}_{\text{ad}}$  species easily as Ru does in the PtRu electrocatalyst. The CO-like poisoning species can then be transformed to  $\text{CO}_2$  and other products at lower potentials, which can easily dissolve in water, releasing more active sites on the electrocatalyst for further electrochemical reaction [35]. Hu *et al.* [36] prepared NiO promoted Pt/C and Pd/C electrocatalysts by an intermittent microwave heating (IMH) method and tested the electrocatalyst's susceptibility towards CO poisoning during the ethanol oxidation reaction [36]. The Pd-NiO/C electrocatalyst showed a higher activity towards ethanol oxidation and less poisoning than the Pt-NiO/C electrocatalyst.

Liu *et al.* [37] used titanium-supported Pd nanoparticles to study the kinetics of ethanol oxidation in alkaline medium [37]. The cyclic

## Chapter 2: Literature review

---

voltammograms of ethanol oxidation in 1.0 M KOH solution containing 1.0 M ethanol on Pd/Ti electrode with the sweep rate of  $5 \text{ mV s}^{-1}$  and the potential range of  $-0.9$  to  $0.1 \text{ V}$  showed two well-defined current peaks on the forward and reverse scans. The onset potential, the peak potential and peak current density for ethanol oxidation were  $-0.65 \text{ V}$ ,  $-0.20 \text{ V}$  and  $6.4 \text{ mA cm}^{-2}$ , respectively.

The alkaline environment enables the usage of non-noble transition metals such as nickel, copper based materials to catalyse the electro-oxidation of alcohols [38]. Jafarian *et al.* [39] studied the electro-catalytic oxidation of methanol on a Ni-Cu alloy with atomic ratio of 60/40 having previously undergone 50 potential sweep cycles in the range of  $0 - 600 \text{ mV vs. (Ag/AgCl)}$  in  $1.0 \text{ M NaOH}$  using CV, chronoamperometry (CA) and EIS. They observed large anodic peaks both in the anodic and early stages of the cathodic direction of potential sweep around  $420 \text{ mV vs. (Ag/AgCl)}$ . The Ni-Cu alloy electrocatalyst showed a higher electro-catalytic surface towards methanol oxidation when compared to that of a pure nickel electrode [39].

Tarasevich *et al.* [40] prepared 15 wt% RuNi/C electrocatalyst containing Ni amount of 20 – 40 % from Vulcan XC 72,  $\text{RuOHCl}_3$  and  $\text{NiSO}_4$  salts. The electrocatalyst consisted of dispersed metallic

## Chapter 2: Literature review

---

ruthenium decorated by nickel oxides and showed a higher ethanol oxidation activity in the alkaline medium. They showed that the electrocatalyst's performance was comparable with the available data of dispersed PtRu electrocatalyst towards methanol electro-oxidation in alkaline medium. A specific activity of  $150 \text{ A g}^{-1}$  at  $E = 0.5 \text{ V}$  was observed. It was also observed that the KOH concentration and the electrolyte temperature affect the rate of the alcohol oxidation. The rate of the alcohol oxidation increased as the KOH concentration or temperature was increased [40].

Gold is also considered to be a good electrocatalyst for alcohol oxidation in alkaline medium. It has the ability to prevent the formation and adsorption of poisoning species such as CO. Thus, a low alcohol activity on a gold electrocatalyst would not be due to the consequence of CO poisoning phenomena as it is on the Platinum electrocatalyst. The loss of activity on the Platinum electrocatalyst due to the CO poisoning phenomenon has been proven by using the in situ infrared (IR) reflectance spectroscopy [41].

Other metals that have been used for electrocatalyst synthesis for direct alcohol fuel cell application include; RuM [42] where (M= Co, Fe, Ni) [43], Pd [34] and Pd (Ni-Zn)/C [44]. Table 2.3 summarizes the

## Chapter 2: Literature review

---

other work that has been done on alcohol oxidation in alkaline medium.

**Table 2.3:** Summary of work that has been done on alcohol oxidation in alkaline medium.

<b>Modified electrode</b>	<b>Synthetic method</b>	<b>Electrode fabrication</b>	<b>Base + alcohol</b>	<b>Reference</b>
Pd-Zeolite-graphite	Immersion technique	Drop-dry	0.5 M NaOH +0.5 M EtOH	[45]
Pd disk	-	-	0.1 M KOH + (1.0 M EtOH or 2- propanol)	[46]
Pd/MWCNT-GCE	Impregnation reduction	Drop-dry	2.0 M KOH+ ( EtOH, MeOH or glycerol)	[47]
Pd/MWCNT-graphite rod Pd/C-graphite rod Pd/ACF-graphite rod (Activated carbon fiber)	Intermittent microwave heating (IMH)	Drop-dry	1.0 M KOH + 1.0 M EtOH	[48]

## Chapter 2: Literature review

Pd-Au substrate	Electrochemical deposition		1.0 M KOH + 0.5 M EtOH	[49]
Pd/C Pd-(Ni-Zn)/ C-GCE Pd-(Ni-Zn-P)/ C-GCE	Redox transmetalation process involving the spontaneous deposition of palladium onto Ni-Zn alloys	Drop-dry	2.0 M KOH + 10% EtOH	[44]
Pd disk	-	-	1.0 M KOH + 1.0 M EtOH	[24]
Pd/nanowire/GCE	Electron beam irradiation	Dip-dry	1.0 M KOH + 1.0 M EtOH	[50]
Pd/MWCNT-GCE Pd/MWCNT/Ni-GCE	chemical reduction using NaBH <sub>4</sub>	Drop-dry	1.0 M KOH + 1.0 M EtOH	[51]
CNT-Ni substrate	CNT grown by pyrolysis of granular polyethelyene in the atmosphere	-	0.1 M KOH + 1.0 M EtOH	[52]

## Chapter 2: Literature review

---

	in Ni plate substrate			
Au-Zeolite-graphite	Immersion technique	Drop-dry	0.5 M NaOH + 0.5 M EtOH	[53]
PdPt/Ti (foil)	Electrochemical deposition	-	1.0 M KOH + 1.0M EtOH	[54]
Pd/CMS/carbon rod	Chemical reduction using NaBH <sub>4</sub>	Drop-dry	1.0 M KOH + 1.0 M EtOH	[55]
Pd/C/graphite rod PdCeO <sub>2</sub> /C-graphite rod PdNiO/C-graphite rod	Microwave heating technique	Drop-dry	1.0 M KOH + 1.0 M EtOH	[35]
PdRu/Ni (foil)	Co-deposition	-	1.0 M NaOH + 1.0 M EtOH	[56]
Au (grid)-GCE	-	-	0.1 M NaOH+ 0.1 M EtOH	[41]
Pd-In <sub>2</sub> O <sub>3</sub> /CNT-GCE	Chemical reduction using	Drop-dry	0.5 M NaOH+ 1.0 M EtOH	[57]

## Chapter 2: Literature review

---

	NaBH <sub>4</sub>			
Pd/Ti(foil)	-	Electrodeposition	0.1 M KOH + 0.1 M EtOH	[37]
PdAu-GCE	nano-Au seed mediated epitaxial growth method	Drop + dry	1.0 M KOH + 1.0 M EtOH	[58]
Au-Co	Electrochemical deposition	-	0.2 M NaOH + 10 mM EtOH	[59]
Ni hollow spheres-PTFE carbon electrode	Stober method	-	1.0 M KOH + 1.0 M EtOH	[60]
Pd-WC/C	Intermittent microwave heating (IMH)	Drop + dry	1.0 M KOH + 1.0 M EtOH	[61]
Pd/TiO <sub>2</sub> /C (graphite rod)	Mild hydrothermal method	Drop + dry	1.0 M KOH + 1.0 M EtOH	[62]
PdAu/C-GCE PdSn/C-GCE	Chemical reduction using NaBH <sub>4</sub>	-	0.25 M KOH + 1.0 M EtOH	[63]

## Chapter 2: Literature review

---

S-MWCNT/Pd-CGE	Chemical reduction using NaBH <sub>4</sub>	Drop + dry	0.2 M KOH + 0.5 M EG	[64]
Pd-(Ni-Zn)/ C-GCE Pd-(Ni-Zn-P)/ C-GCE	Redox transmetalation process involving the spontaneous deposition of palladium onto Ni-Zn alloys	Drop-dry	2.0 M KOH + 5 wt% EG	[2]
Pd/CMS-carbon rod	Chemical reduction using NaBH <sub>4</sub>	Drop-dry	1.0 M KOH + 1.0 M (ethylene glycol, methanol, ethanol)	[65]

### 2.2.4 Support materials for electrocatalysts

A large amount of research has been done to lower the electrocatalyst cost in order to commercialize fuel cells. This includes the use of platinum-free metal electrocatalyst. Researchers are also putting efforts in developing conducting supports alternative to carbon black. The main goal is to develop supports that will be able to increase the electro conductivity, activate the metal particles, enhance the stability of the electrocatalyst and improve the electrocatalyst dispersion [47]. Support materials play an important role on the performances of electrocatalysts for fuel cells. A material is supposed to have a high surface area, be electrical and thermal conductive, should be stable in the fuel cell conditions and should be porous enough to allow the reactants to flow in order to be considered as a support material for a fuel cell electrocatalyst [25].

The different materials that have been studied as electrocatalysts supports include carbon blacks [66,67] carbon nanotubes (CNTs) [47,68,69], microspheres [55], tungsten carbides [70-72], carbon nanofibers [73], TiO<sub>2</sub> nanotubes [62], carbon nanocoils, carbon spheres and hollow graphitic nanoparticles [47] [60]. The carbon nanotubes are attracting increasing interest as efficient support materials for electrocatalysts [69,74-82] due to their high mechanical

## Chapter 2: Literature review

strength, good conductivity, and high surface areas. There are two main types of carbon nanotubes (Figure 2.3) namely; single walled (SWCNT) and multi walled carbon nanotubes (MWCNT).

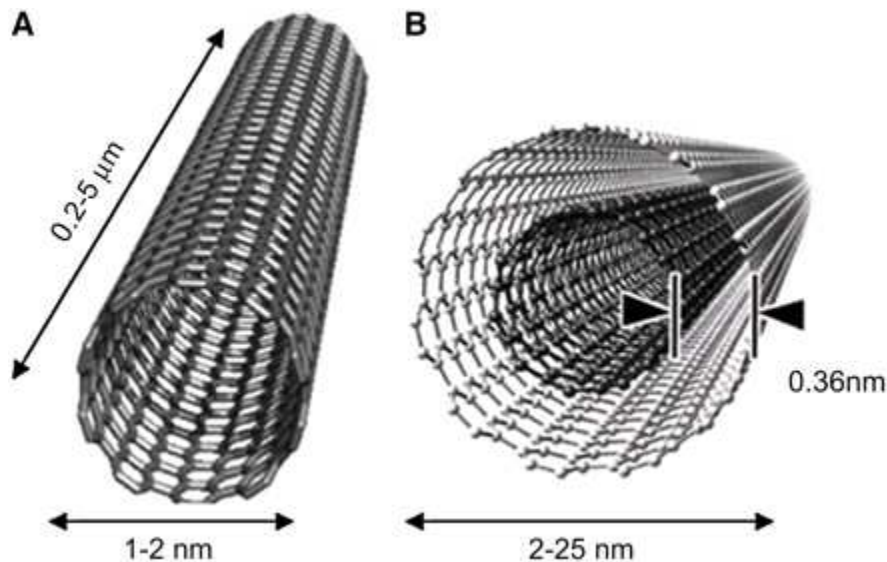


**Figure 2.3:** Conceptual diagrams of (a) SWCNT and (b) MWCNT taken from [83, 84]

The difference between the two types of carbon nanotubes is in the number of graphene sheets and their arrangements. Only one graphene sheet rolled into a cylinder is used in preparing a SWCNT is whereas a MWCNT is made of many graphene sheets coaxially rolled into a cylinder [85] . Saito *et al.* [86] have reported that SWCNTs can be either metallic or semi conducting depending on the tube and the

## Chapter 2: Literature review

---

helicity. The studies done by Kasumov *et al* [87] demonstrated that MWCNT have a relatively higher conductivity than SWCNT due to their larger outer shells as compared to that of SWCNT using scanning tunneling spectroscopy (STS) studies. The MWCNT were therefore chosen as a support material for the electrocatalysts in this work.

However, for the MWCNTs to be effectively used as support materials, they need to be functionalised in order to be easily dispersible in solvents. Some notable methods of functionalizing CNTs include acid treatments [57,88-90] and sulfonation processes [64,91] .

### **2.3 Electrocatalyst Preparation Methods**

#### **2.3.1 Introduction**

The different methods that can be used in preparing an electrocatalyst are very diverse and each electrocatalyst may be produced via different routes. The methods that can be used in preparing the electrocatalyst have great influence on the structure, size, morphology, and hence the electrocatalytic properties of the electrocatalyst. Various methods can be used to prepare fuel cell electrocatalysts, these methods include electrochemical deposition [49,54,59,92], co-impregnation-reduction method [93], chemical reduction [47,55,57,63,65,94], microwave synthetic method [5,48,61,95-98], impregnation reduction [47], electron beam irradiation [49], immersion technique [45,53], the Bönemann method [99], water in oil microemulsion method [100,101], ultrasonic irradiation [27,102,103] and alcohol reduction processes [104].

#### **2.3.2 Microwave synthetic method**

The microwave-assisted solvothermal synthesis (MWAS) is a very attractive synthetic method for the preparation of nano-electrocatalysts [95, 97, 98]. This method makes use of a microwave to generate heat energy that accelerates a desired chemical reaction.

## Chapter 2: Literature review

---

Microwaves are oscillating electromagnetic energy with frequencies in the 300 MHz – 300 GHz range [105]. When the reaction mixture is exposed to a microwave radiation, the microwave induces the rotation of the dipoles within the liquid which forces the polar molecules to align themselves and relax in the field of oscillating electromagnetic radiations. This causes the liquid to become hot. The thermal gradients inside the microwave vessels are minimized and reaction kinetics is increased as the heat produced within the liquid is not transferred from the vessel as in the other conventional systems [106,107]. Figure 2.4 shows the microwave system used in this work.



**Figure 2.4:** Anton Paar Multiwave 3000 microwave system

## Chapter 2: Literature review

---

In this method, EG is commonly used and plays many roles. These roles include, acting as a solvent for the metal salts, reducing agent for the metal salts, and a growth medium for the metal particles [108,109]. EG can be rapidly heated by microwave radiations due to its high dielectric constant (41.4 at 298 K) and dielectric loss. The microwave synthetic method is faster, cleaner, simpler and more energy-efficient than the conventional chemical reduction systems [98,110]. In this work, microwave synthetic method was used to synthesise electrocatalysts supported on MWCNTs.

### **2.4 Microscopic and Spectroscopic Catalyst Characterization Techniques**

In order to obtain important properties of a synthesized electrocatalyst, one needs to characterize the electrocatalyst. There are two main techniques of catalysts characterization namely; physical and electrochemical characterization techniques. Many ex situ physical characterization techniques can be used in characterizing a fuel cell electrocatalyst [111]. This chapter presents a brief background on the different microscopic and spectroscopic techniques used to characterize the prepared electrocatalysts.

#### **2.4.1 X-Ray powder diffraction**

Powder X-ray diffraction (XRD) technique is used to determine the crystallite structure of a material [112]. During analysis, high speed electrons collide with the metal target to produce X-rays. The sample must be sufficiently crystalline in order to diffract X-rays [113]. Figure 2.5 shows X-ray diffractions on a crystalline material. When X-ray radiation is directed on a sample, the X-rays are scattered by electrons present on the sample resulting in maximum and minimum diffracted intensity. The maximum signal obeys the Bragg's law which is given by equation 2.9.

## Chapter 2: Literature review

---

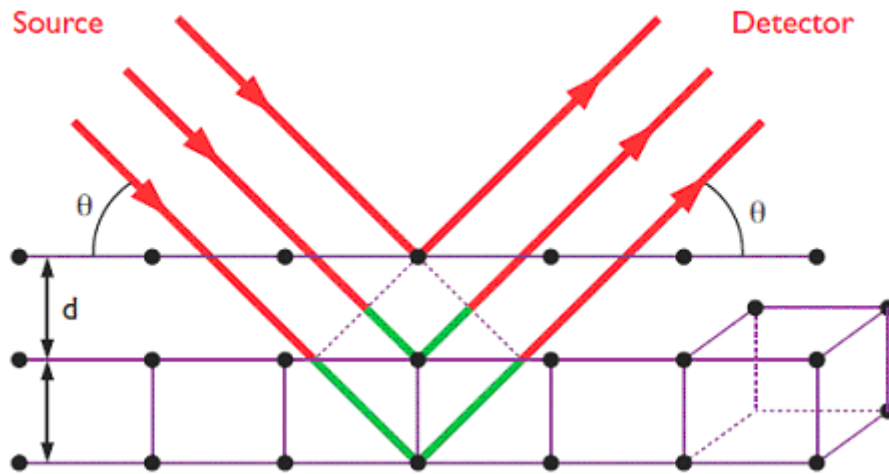


**Figure 2.5:** Schematic diagram of X-rays diffraction in a crystalline material taken from [114].

Bragg's law

$$n\lambda = 2d \sin \Theta \quad (2.9)$$

where  $n = \text{integer}$ ;  $\lambda = \text{x-ray wavelength}$ ;  $d = \text{distance between crystal lattice planes}$  and  $\theta = \text{diffraction angle}$ .

Bragg's law is satisfied when the path length difference of x-rays is equal to  $n\lambda$ , The diffraction angle  $\theta$  is half the angle between the incident and diffracted x-rays [114]. The angle of diffraction differs for

## Chapter 2: Literature review

---

various planes within a crystal. Thus, every element or compound has its own unique diffraction pattern. The x-ray diffraction pattern is obtained as the intensity of the detected x-rays against the angle  $\theta$ . The crystallite size determination is based on the quantification of the broadening of the diffraction peaks [115]. Many researchers use the Scherrer equation to determine crystallite size of metals in a fuel cell electrocatalyst. However, there are many other methods that can be used in crystallite size determination. The alternative methods include the Hall-Williamson approach and the Fourier method of Warren-Averbach [115]. The Scherrer equation is applicable when the peak broadening is only dependent on the crystallite size and diffractometer characteristics, this occurs when the microstrains and defects are negligible [116]. In this work, the XRD technique was used to determine the crystallite structure of the prepared electrocatalysts.

### **2.4.2 Transmission electron microscopy**

Transmission Electron Microscopy (TEM) is a technique that is used to produce the images of the samples. The images produced are used to study the characteristics of the samples such as morphology. The TEM technique can also be used to complement the XRD in particle size determination. The working principles of a transmission electron

## Chapter 2: Literature review

---

microscope are similar to that of an optical microscope. However, the quality of the images differs. The TEM produces images with higher resolutions than an optical microscope [117]. During analysis, a narrow beam of electrons is concentrated onto an ultra-thin sample surfaces, an image is produced as a result of the interaction between the electrons and the sample atoms [117,118]. The image is then magnified and then focused onto a fluorescent screen. In this work, the TEM technique was used to study the structure of the prepared electrocatalysts.

### **2.4.3 Energy dispersive x-ray spectroscopy**

Energy dispersive x-ray (EDX) spectroscopy is a technique that is used to identify the elements present in a sample. One can do the EDX measurement immediately after a TEM or Scanning Electron Microscopy (SEM) analysis as the two instruments are usually integrated. In operation, an electron beam is passed through a sample; the atoms in the sample generate x-rays which are detected to produce a spectrum. The energy of each x-ray is attributed to the element which produced it [119,120]. In this work the EDX technique was used to confirm the metal particles present on each electrocatalyst.

## Chapter 2: Literature review

---

### 2.4.4 Raman spectroscopy

Raman spectroscopy is a useful technique for the characterization of different materials that can be used as support materials for a fuel cell electrocatalyst. This technique is used to study vibrational, rotational and other low-frequency modes in molecules [121]. Raman spectroscopy makes use of a scattering laser light source. During the analysis, the laser light release photons onto the sample, the sample adsorbs some of the photons and re-emits some producing a scattered radiation of different wavelengths [122]. A phenomenon known as the Raman shift occurs as the frequency of the re-emitted photons is shifted up and down when compared to the original light frequency. Useful information about the vibrational, rotational and other low frequency transitions molecules can be obtained from this shift [123]. Raman spectroscopy technique is similar to FTIR; the main difference is on the radiation frequency used. Raman spectroscopy makes use of a single frequency of radiation while FTIR uses a radiation which covers a wide range of frequencies [124]. Below is a typical Raman spectrum of MWCNTs taken from [125].

## Chapter 2: Literature review

---

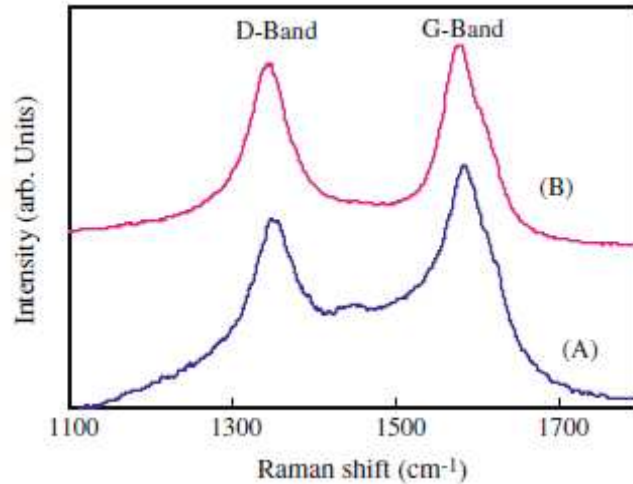


**Figure 2.6:** Raman spectra of (A) synthesized MWCNT, (B)  $N_2 + Ar$  plasma treated MWCNTs taken from [125].

Two principal bands are observed on the Raman spectrum of MWCNT, namely the D and the G bands. These bands provide information on the defects or the purity of the carbon nanotubes. The G band is associated with the stretching mode in the graphite plane due to the in-plane vibration of the  $sp^2$  carbon atoms while the D band is the disorder band which is due to the defects in the nanotubes [126,127]. The D band occurs between  $1330-1360\text{ cm}^{-1}$  and the G band at  $\sim 1580\text{ cm}^{-1}$  [103,128]. The D/G ratio is used to determine the quality of the carbon nanotubes. A large quantity of structural defects is indicated by similar intensities [129]. In this work the technique was used to sense the structural disorders on the multi walled carbon nanotubes due to the functionalization processes.

## Chapter 2: Literature review

---

### **2.4.5 Fourier transform infrared spectroscopy**

Fourier transform infrared (FTIR) spectroscopy is used to identify functional groups present on the surfaces of materials [130,131]. The technique relies on the absorption of an infrared irradiation beam by molecules within a sample, which causes the chemical bonds within the molecules to vibrate [132]. Each functional group within a molecule will have different bond energies resulting in infrared absorption at different wavelengths. The total bond energy within a molecule is given by the sum of the electronic, vibrational, rotational and translational energies [132]. In principle, an infrared irradiation beam covering a wide range of frequencies is passed through a sample; the sample absorbs some of the infrared radiation and transmits some resulting in the vibration of chemical bonds within the molecules, a signal is sent to the detector resulting in an infrared spectrum [118]. In this work, FTIR was used to confirm the presence of the sulfonic groups incorporated on the surface of the MWCNTs.

## Chapter 2: Literature review

---

### 2.5 Electrochemical Characterization

Electrochemistry is used in this work to investigate the electrocatalytic behaviour of the prepared electrocatalysts. An electrochemical experimental setup consists of a potentiostat, an interface and a computer. An electrochemical cell depicted in figure 2.7, is used during electrochemical measurements. An electrochemical experimental setup consists of a potentiostat, a working electrode (WE), a reference electrode (RE) and a counter electrode (CE) [118]. The function of the WE is to provide an interface across which a charge can be transferred and the RE defines the potential at the WE [118]. A potentiostat is an instrument that is used to measure the current flow between the WE and the CE. It is also used to control the potential of the WE with respect to the RE. Figure 2.7 shows a diagram of an electrochemical experiment setup in a three electrode system.

Chapter 2: Literature review

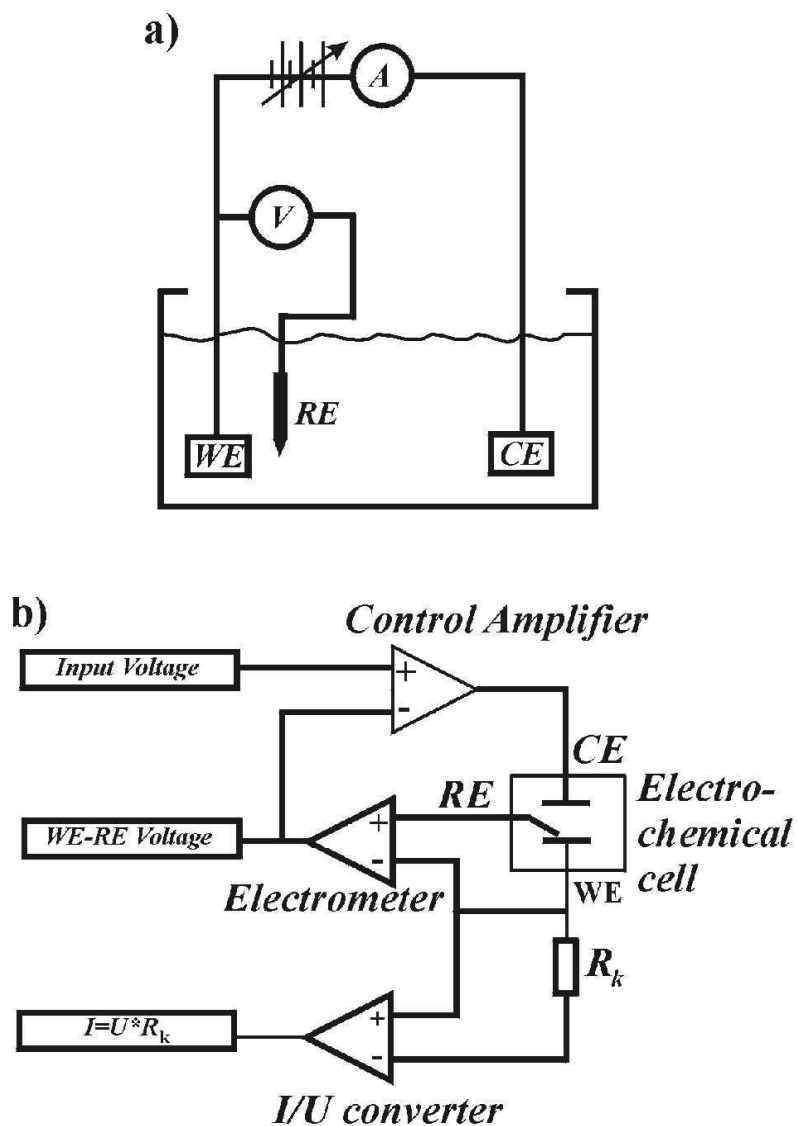


**Figure 2.7:** A diagram of (a) The simplest experimental setup for performing electrochemical experiments. (b) A schematic representation of a three electrode potentiostat taken from [133].

## Chapter 2: Literature review

---

The manner in which the materials move from the bulk solution to the electrode surface during an electrochemical measurement is of great importance. This phenomenon is known as the mass transport. Three different basic mass transport mechanisms occurs during an electrochemical experiment and these are diffusion, migration and convection [134] (depicted in Figure 2.8).

**Diffusion** occurs when molecules moves randomly from a region of where they are highly concentrated to regions where they are low concentrated [135]. The difference in the concentration causes a concentration gradient which determines the rate at which a molecule can diffuse. It is difficult to avoid diffusion as it is common in all voltammetry experiments as the concentration gradient often occurs. The geometry and size of an electrode are important in determining the flux at the electrode, which then determines the current response for diffusion only electrochemical experiments [136].

**Convection** is a type of mass transport which occurs when the molecules move as a result of an induced bulk motion in the solution such as stirring. Sometimes it occurs naturally due to density gradients and vibrations [136].

## Chapter 2: Literature review

**Migration** occurs when molecules moves down an electric gradient. This type of mass transport can be prevented by introducing an ionic charge carrier [136].

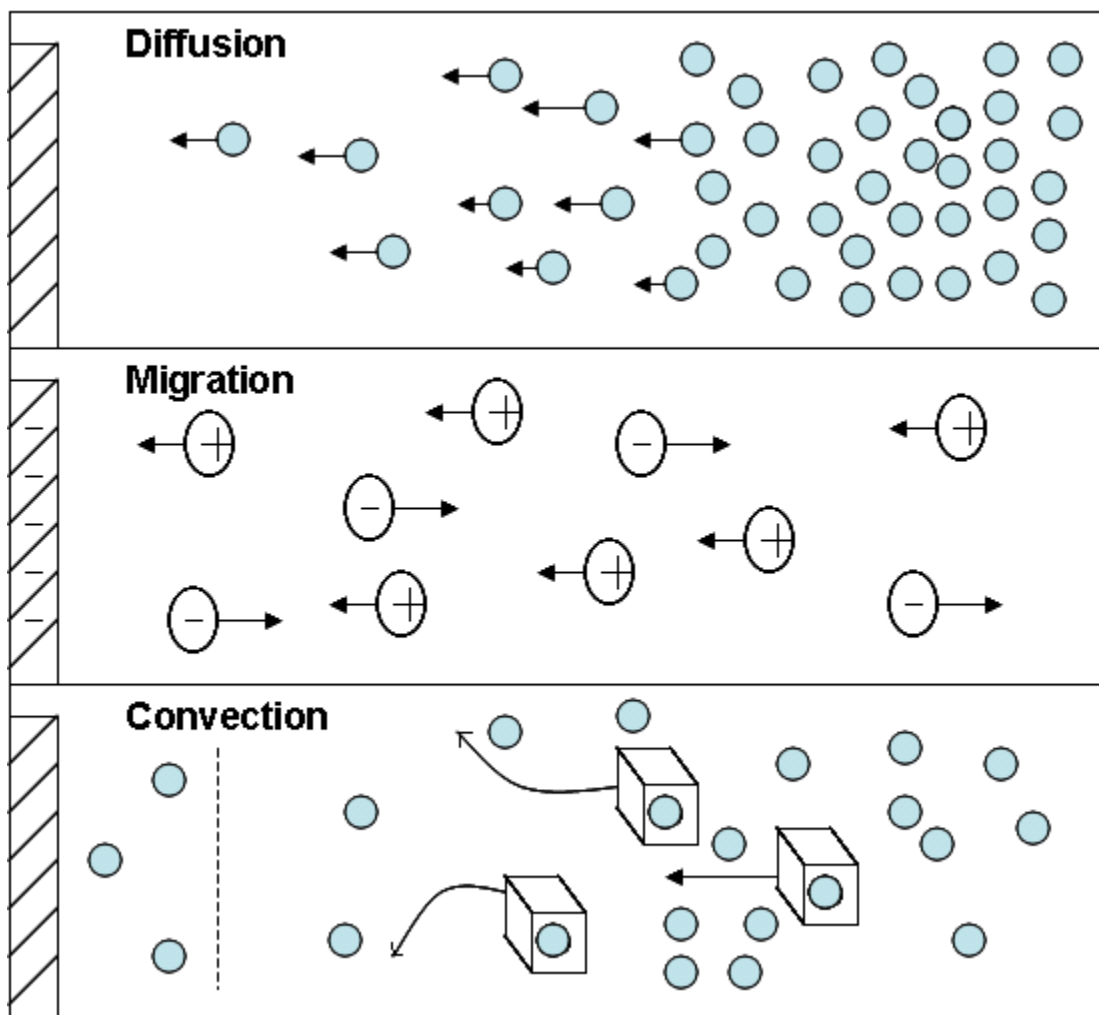


**Figure 2.8:** Schematic representation of the three modes of mass transport taken from [134].

This section below gives an overview of the electrochemical techniques employed.

## Chapter 2: Literature review

---

### 2.5.1 Cyclic voltammetry

The standard tool for the electrochemical characterization of a fuel cell electrocatalyst is a CV. A CV experiment is often the first experiment performed during electrochemical studies. The potential of the working electrode is scanned linearly in an unstirred solution using a triangular waveform (Figure 2.9).

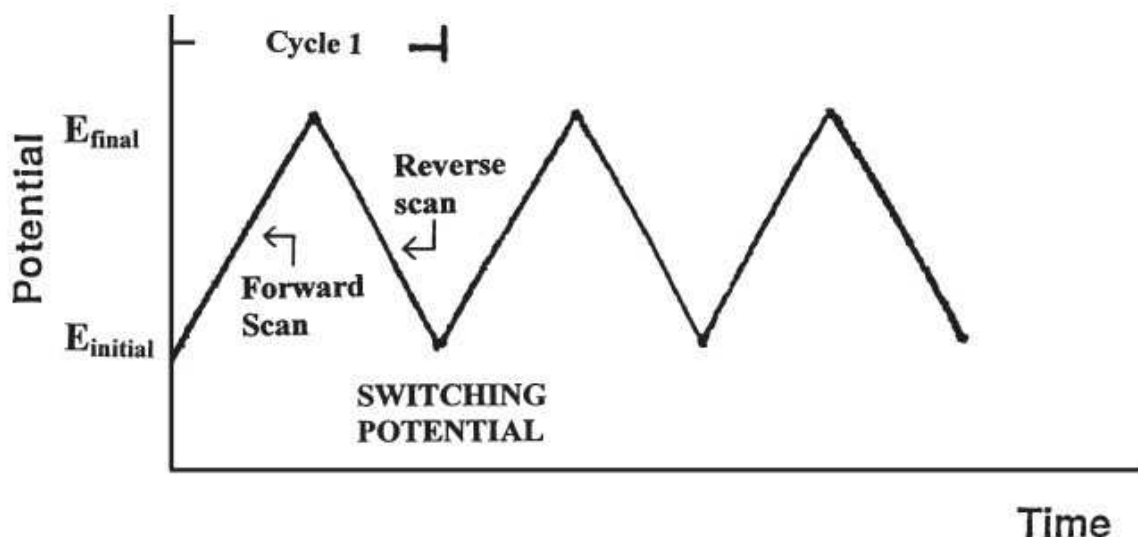


**Figure 2.9:** Potential-time excitation signal in a cyclic voltammetric experiment taken from [134].

The Initial ( $E_i$ ) and final ( $E_f$ ) potential values are chosen before scanning the WE. This is unknown as the potential window. The Working electrodes' potential is then scanned linearly from the initial potential to the final potential. The direction of the scan is reversed when the final potential is reached. The potential is then scanned

## Chapter 2: Literature review

backwards towards the initial potential value forming a cyclic voltammogram. A cyclic voltammogram is a plot of the current observed against the potential (Figure 2.10), the plot can be used to determine the reactions which are occurring on the surface of the working electrode [118]. One or two peak currents are observed on redox active species after scanning the potential of the WE. The potentials at which the peak currents occurs are known as the peak potentials,  $E_p$ . This can either be the anodic peak potential ( $E_{pa}$ ) or the cathodic peak potential ( $E_{pc}$ ). The two peak currents are the anodic peak current, ( $I_{pa}$ ) and the cathodic peak current ( $I_{pc}$ ).

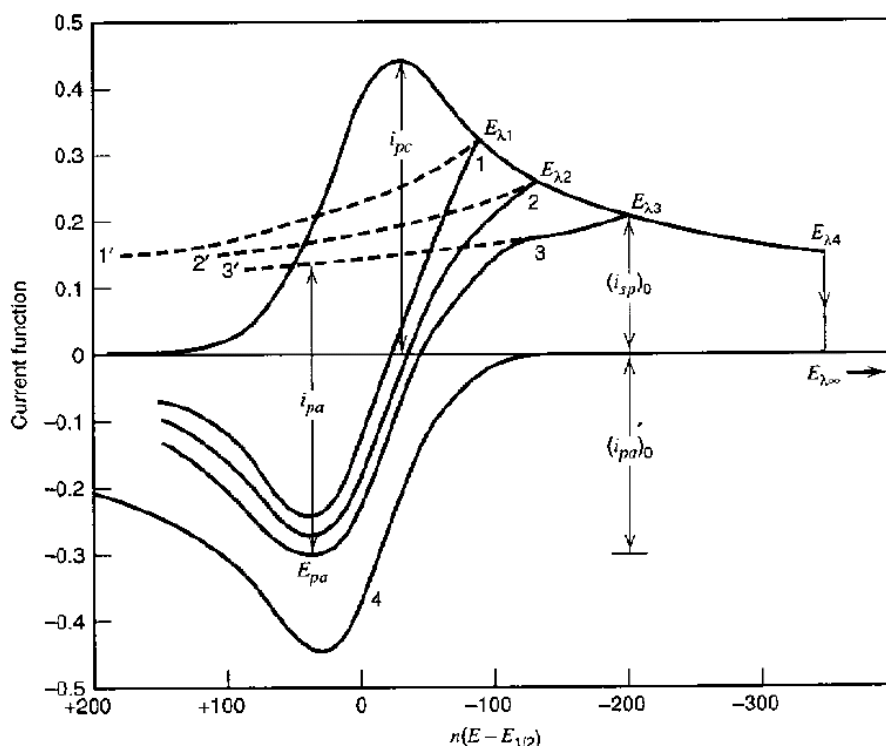


**Figure 2.10:** Typical cyclic voltammogram for a reversible process taken from [137].

## Chapter 2: Literature review

---

Cyclic voltammetry process can be reversible, quasi-reversible or irreversible depending on the analyte.

### Reversible process

A reversible process is characterized by two peaks, namely the forward oxidation peak and the reverse reduction peak. The process obeys the Nernst reaction in which the electron transfer is fast and the concentrations of the oxidized and reduced species are assumed to be in equilibrium as shown in equation 2.10. Figure 2.10 shows a typical CV of a reversible process. The  $I_{pa}/I_{pc}$  value of a reversible process is equal to one. The magnitude of the  $I_p$  is directly proportional to the square root of the scan rate,  $\nu$ . The value of the peak separation ( $\Delta E_p$ ) of an ideal reversible process is independent of  $\nu$ . However, in real systems; this value slightly increases with increasing  $\nu$  due to the solution resistance ( $R_s$ ) between the RE and WE [138].



The peak separation of a reversible process is given by equation 2.11.

$$\Delta E_p = [E_{pa} - E_{pc}] = \frac{2.303RT}{nF} = \frac{59}{n} mV \quad \text{at } 25 \text{ } ^\circ\text{C} \quad (2.11)$$

## Chapter 2: Literature review

---

where  $\Delta E_p$  = change in peak potential;  $E_{pa}$  and  $E_{pc}$  = the anodic and cathodic peak potentials;  $R$  = universal gas constant;  $T$  = temperature (K) ;  $n$  = number of electron; and  $F$  = Faraday's constant.

The formal potential ( $E^0$  or  $E_{1/2}$ ) of a reversible process is given by equation 2.12

$$E^0 = E_{1/2} = \frac{E_{pc} + E_{pa}}{2} \quad (2.12)$$

where  $E_{pa}$  and  $E_{pc}$  are the anodic and cathodic peak potentials, respectively.

The Randles–Sevcik equation (at 25 °C) is used to determine the type of mass transport governing a reversible process (equation 2.13).

$$i_p = (2.69 \times 10^5) n^{3/2} A C^0 D^{1/2} \nu^{1/2} \quad (2.13)$$

where  $i_p$  = peak current ;  $A$  = electrode area ;  $D$  = diffusion coefficient ;  $C^0$  = concentration and  $\nu$  = scan rate.

A process is characterized as planar diffusion controlled if the peak current is directly proportional to the square root of the scan rate [139].

## Chapter 2: Literature review

---

### **Irreversible process**

Only one redox process occurs during an irreversible process. The forward oxidation peak is normally observed during an irreversible process. This peak is usually associated with the oxidation of freshly absorbed species on the electrode during alcohol electro-oxidation. However, a reverse oxidation peak is also observed in some instances due to the oxidation of species which were not completely oxidized during the forward scan, slow electron exchange or slow chemical reactions at the electrode surface [140].

The peak current,  $I_p$  for an irreversible process is given by equation 2.14

$$i_p = (2.99 \times 10^5) n [(1 - \alpha)n]^{1/2} ACD^{1/2} \nu^{1/2} \quad (2.14)$$

where  $\alpha$  = rate of electron transfer,  $A$  = electrode area ( $\text{cm}^2$ ),  $c$  is the concentration of the active species ( $\text{mol cm}^{-3}$ );  $D$  = diffusion coefficient ( $\text{cm}^2 \text{s}^{-1}$ ); and  $\nu$  = scan rate ( $\text{V s}^{-1}$ ).

### **Quasi-reversible process**

## Chapter 2: Literature review

---

A quasi-reversible process is an intermediate process between the reversible and irreversible systems. This process occurs when the relative rate of electron transfer cannot sustain the Nernst equilibrium at the electrode surface when compared to that of mass transport. The current observed during a quasi-reversible process is controlled by both the mass transport and charge transfer kinetics [134,141]. The  $I_p$  is directly proportional to the  $v^{1/2}$ . However, this occurs in a non-linear manner and the value of  $\Delta E$  is greater than  $59/n$  mV [137].

The diagnostic criteria for the reversible, irreversible and quasi-reversible cyclic voltammetric processes are summarized on table 2.4.

## Chapter 2: Literature review

**Table 2.4:** The diagnostic criteria for cyclic voltammetric processes [137,141,142].

Parameter	Cyclic Voltammetry Process		
	Reversible	Irreversible	Quasi-reversible
$E_p$	Independent of $v$	Shifts cathodically by $30 / \alpha n$ mV for a 10 -fold increase in $V$	Proportional to $v$
$E_{pc}-E_{pa}$	$\sim 59 / n$ mV at 25 °C and independent of $v$	-	May approach $60 / n$ mV at low $v$ but increases as $v$ increases
$I_p / v^{1/2}$	Constant	Constant	Virtually independent of $v$
$I_{pa} / i_{pc}$	Equals 1 and independent of $v$	No current on the reverse side	Equals 1 only for $\alpha = 0.5$

## Chapter 2: Literature review

---

### 2.5.2 Chronoamperometry

Chronoamperometry is an electrochemical technique similar to cyclic voltammetry. However, the potential of the WE in a chronoamperometry experiment is stepped as depicted in figure 2.11 and not scanned. The potential of the WE is stepped from an initial potential to a final potential and the resulting current is recorded as a function of time. The experiment is normally conducted in an unstirred solution so that the experiment can be diffusion controlled. The starting potential is set at a value where no reaction occurs, then stepped to a potential where a reaction occurs and current is observed [143]. The initial observed current is high, but it rapidly decreases as the species on the surface of the electrode are completely oxidized or reduced.

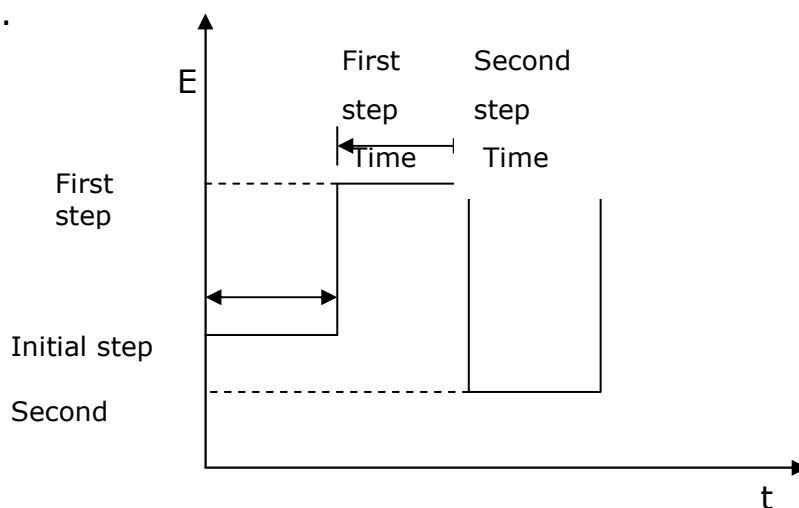


**Figure 2.11:** A potential wave form depicting chronoamperometry

## Chapter 2: Literature review

---

The relationship between the current observed and the reaction time of a reaction which is controlled by linear diffusion is described by the Cottrell equation (equation 2.15)

$$i = nFACD^{1/2}\pi^{-1/2}t^{-1/2} \quad (2.15)$$

where  $n$  = number of electrons transferred / molecule;  $F$  = Faraday's constant;  $A$  = electrode area;  $D$  = Diffusion coefficient;  $C$  = concentration and  $t$  = time.

The Cottrell plot is a plot of  $i$  versus  $t^{-1/2}$ . The current decrease during a chronoamperometric experiment is proportional to the reciprocal of the square root of the reaction time. This behaviour confirms that the physical diffusion is the mode of mass transport responsible for transporting the analyte species onto the electrode surface [143] . In this work, the chronoamperometry technique was use to investigate the stability of the electrodes at a constant potential.

### 2.5.3 Chronopotentiometry

Chronopotentiometry (CP) is an electrochemical technique which measures potential against time at a constant current. An unstirred solution is used during a chronopotentiometric experiment to limit the mass transport to diffusion. A constant current is applied on the WE electrode during the experiment, resulting in a decrease in the concentration of the oxidizing species on the electrode surface and a change in potential. The quantitative analysis can be done by relating  $\tau_{1/2}$  to  $C_{ox}$  using the Sand equation (2.16) [119].

$$\tau_{1/2} = \frac{\pi^{1/2} n F A D^{1/2} C_{ox}}{2i} \quad (2.16)$$

where  $\tau_{1/2}$  is the half life (s);  $n$  = number of electrons;  $F$  = Faraday's constant;  $A$  = electrode area;  $D$  = Diffusion coefficient; and  $C_{ox}$  = concentration of oxidizing species [136].

CP in fuel cells is usually used to determine the susceptibility of the catalyst poisoning due to the presence of intermediates (carbonaceous species) [32,36,48]. Xu *et al*, [32] used chronopotentiometry technique to determine the susceptibility of a catalyst towards poisoning by intermediates. They showed that the Pt-CeO<sub>2</sub>/C

## Chapter 2: Literature review

---

electrocatalyst was more active and resistant to poisoning by intermediates produced during the electrochemical oxidation of alcohols (methanol, glycerol and ethylene glycol) than the Pt/C electrocatalyst.

### 2.5.4 Linear sweep voltammetry

Linear sweep voltammetry (LSV) depicted in figure 2.12, is an electrochemical technique which measures the current at the WE as a function of time. The analyte species are either oxidized or reduced as the potential between the WE and RE is swept linearly resulting in a current response on the WE.

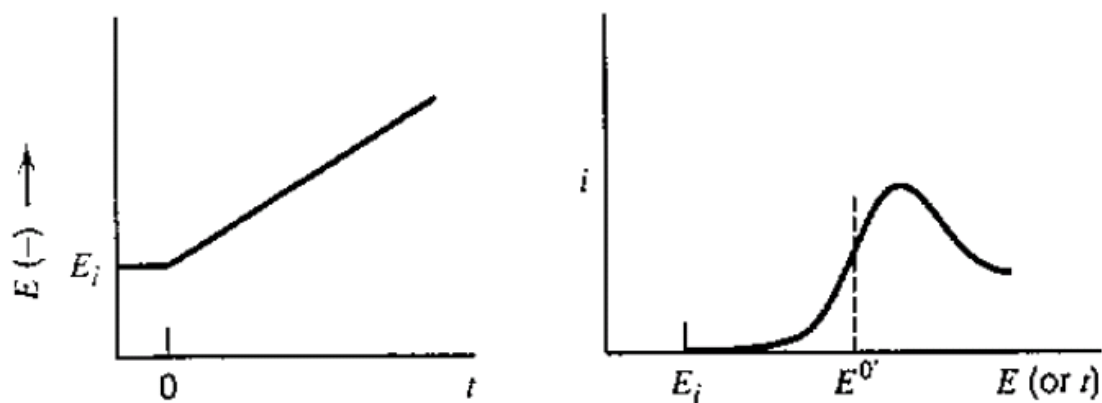


**Figure 2.12:** Typical linear potential sweep and resulting  $i$ - $E$  curve [120].

## Chapter 2: Literature review

---

A LSV experiment is closely related to a CV experiment. The main difference is on the way the potential is controlled. In a LSV experiment the potential is scanned from the initial value to a final value whereas in a CV experiment the potential is cycled. In this work, a quasi-steady state linear sweep voltammetry is used in order to extract Tafel slope.

### 2.5.5 Electrochemical Impedance Spectroscopy (EIS)

EIS is a more sensitive technique for studying the charge and mass transport kinetics and charging processes which occurs between the electrode surface and the interface of the system when compared to cyclic voltammetry [144,145]. EIS has been shown to be a more responsive electrochemical technique for the studies of the electrochemical kinetics of alcohol electro-oxidation processes in fuel cells [146,147]. A small amplitude ac (sinusoidal) excitation signal is applied on the electrode and the resultant current or voltage is measured as depicted in figure 2.13. The excitation signal applied covers a wide range of frequencies [148]. The sinusoidal voltage and current are given by equation 2.17 and 2.18 respectively.

$$E(t) = E \sin(\omega t) \quad (2.17)$$

$$I(t) = I \sin(\omega t + \phi) \quad (2.18)$$

## Chapter 2: Literature review

---

$$w = 2\pi f \tag{2.19}$$

where  $E(t)$  = the potential at time  $t$ ,  $\omega$  = radial frequency ( $\text{rad s}^{-1}$ ) given by equation 2.19 (in radians/second);  $I(t)$  = response signal at time  $t$  and  $\phi$  = the phase shift.

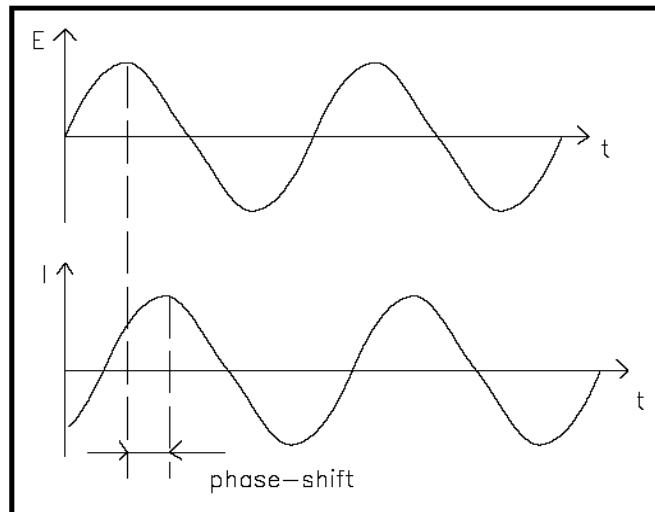


**Figure 2.13:** Sinusoidal current response in a linear system [149]

Impedance is represented as a complex number (equation 2.20)

$$Z = \frac{E}{I} = Z' + jZ'' = Z_{real} + jZ_{imaginary} \tag{2.20}$$

One of the advantages of EIS is the ability to run a measurement without disturbing the analytes' properties extensively due to the usage of small amplitude of the excitation signal. EIS is normally used

## Chapter 2: Literature review

---

to study the electrode kinetics, reaction mechanism of many systems and in the characterization of batteries, fuel cells, and corrosion phenomena [144]. Two plots are obtained during an EIS experiment, these are the Nyquist (plot of imaginary impedance versus real impedance) and Bode (plot of log magnitude of impedance and phase angle versus log of frequency) plots. Randles cell depicted in figure 2.14; is one of the simplest cells.

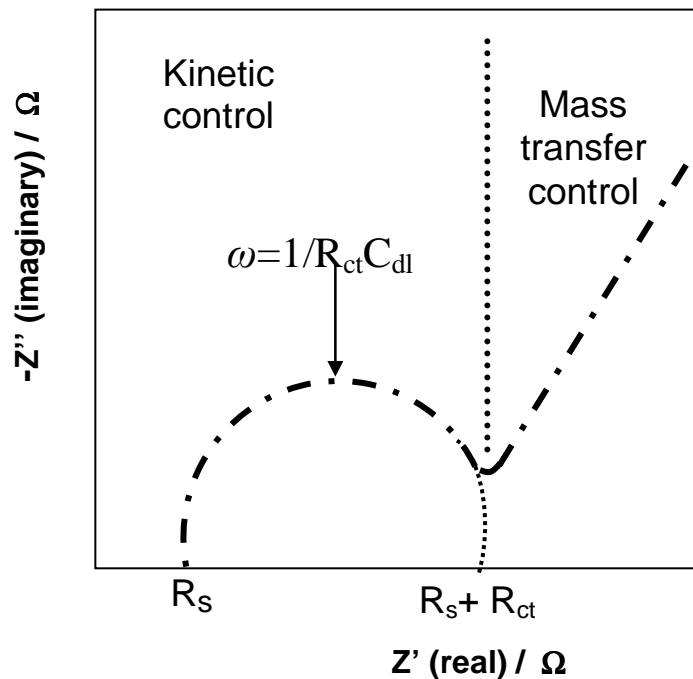


**Figure 2.14:** Nyquist plot of a Randles cell

The Randles cell includes parameters such as solution resistance ( $R_s$ ), a double layer capacitor ( $C_{dl}$ ), charge transfer resistance ( $R_{ct}$ ) and Warburg impedance ( $Z_w$ ). The reaction is kinetically controlled at high

## Chapter 2: Literature review

---

frequencies and is dominated by Warburg impedance at low frequencies. In the case of modified electrodes,  $C_{dl}$  is replaced by constant phase element (CPE) which is associated with porous electrodes. The modified Randles equivalent circuit is depicted in figure 2.15.

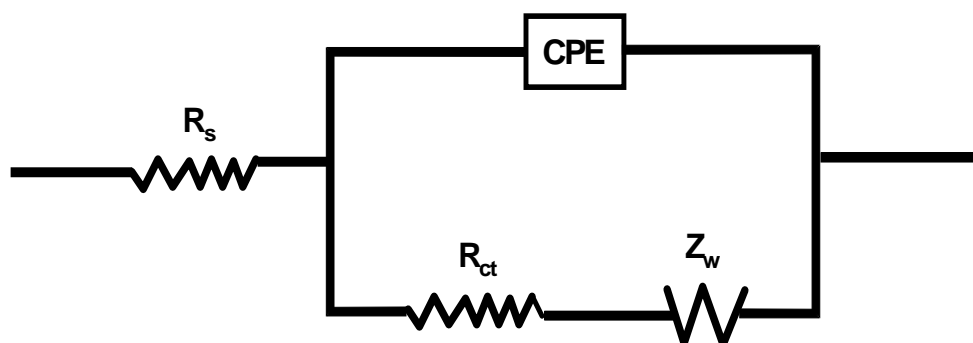


**Figure 2.15:** Modified Randles equivalent circuit

Applications of EIS to study fuel cell electrodes has been reported in [48,63,146,147,150]. He *et al.* [63] used EIS to investigate the kinetics of alcohol electrooxidation; they observed that electron transfer kinetics is faster at higher potentials.

### 2.6 Chemically Modified Electrodes

According to the IUPAC a chemically modified electrode “ is made of a conducting or semiconducting material that is coated with a selected monomolecular, multimolecular, ionic, or polymeric film of a chemical modifier that exhibits chemical, electrochemical or optical properties of the film” [151]. The coating layer can be a single layer or multilayers of different materials. In fuel cell electrocatalyst studies, a binding material such as Nafion® is normally mixed with the analytes’ materials so that it can easily be attached onto the electrode surface. Below are some of the methods that can be used to prepare chemically modified electrodes:

#### (i) Drop – dry

A few drops of an electrocatalyst ink is dropped onto the surface of the electrode when preparing a CME using a drop and dry method. The electrode is air dried for a while to allow the solvent used to prepare the electrocatalyst ink to evaporate [152]. An advantage of using this method is the ability to control the amount of the electrocatalyst on the electrode surface.

#### (ii) Dip- dry

The electrode is immersed in the electrocatalyst ink for a while to allow sufficient spontaneous electrocatalyst film formation to occur by adsorption onto the surface of the electrode, the electrode is then

## Chapter 2: Literature review

---

removed and air dried to allow the solvent used in the ink preparation to evaporate [151]. A major disadvantage of using this method is the inability to control the amount of the electrocatalyst on the surface of the electrode.

### **(iii) Electrochemical deposition**

In this method, the electrocatalyst material is coated onto the surface of the electrode by means of an electric current using a voltammetry technique. The electrode is immersed into the electrocatalyst ink and voltammetric scans are run.

### **(iv) Covalent bonding**

In this method, linking agents (e.g. an organosilanes or cyanuric chloride) are used to covalently attach one or several electrocatalyst layers onto the electrode surface [151].

### **(iv) Spin coating**

The electrocatalyst ink is deposited onto the electrode surface and then dried by spinning the electrode at a high speed resulting in a uniform electrocatalyst film due to the centripetal acceleration.

## Chapter 2: Literature review

---

In this work, the drop-dry method was employed in order to obtain a desired amount of catalyst loading onto the electrode surface.

# **CHAPTER THREE**

## **EXPERIMENTAL**

### 3 EXPERIMENTAL

#### 3.1 Introduction

Fuel cell technology is considered as one of the key alternative power sources for both stationary and portable applications. The anode electrocatalyst is an important component of the fuel cell system as it is used in the alcohol electro-oxidation reaction. At present, Palladium has attracted a lot of interests as a suitable metal to be used in anode electrocatalyst development for the alcohol electro-oxidation in alkaline medium. Studies have shown that the Pd/C electrocatalyst has a higher electro-activity towards alcohol electro-oxidation than the Pt/C electrocatalyst in alkaline medium [32].

In order to enhance the activity of Pd/C electrocatalyst towards alcohol oxidation in alkaline medium, different metals are introduced to the Pd/C catalyst system to form bimetallic or multi-metallic catalyst systems. Different supports and different synthetic techniques are also used in order to prepare better electrocatalyst for alcohol electrooxidation in alkaline medium.

The modification of the Pd/C electrocatalyst is of interest in this study. Different nano metal particles, namely; Pd, Ni and Sn, supported on sulfonated multi-walled carbon nanotubes were

## Chapter 3: Experimental

---

synthesized and then mixed to form mixed bimetallic electrocatalyst systems such as SF-MWCNT-PdNi<sub>mix</sub> and SF-MWCNT-PdSn<sub>mix</sub>. These electrocatalyst systems present interesting electrochemical and structural properties.

This chapter presents a detailed method of preparing the SF-MWCNT-Pd, SF-MWCNT-PdNi<sub>mix</sub> and SF-MWCNT-PdSn<sub>mix</sub> electrocatalyst. The electrocatalysts were prepared using a polyol microwave assisted synthetic technique using sulfonated multi-walled carbon nanotubes as a support material, aqueous metal chlorides as precursors and ethylene glycol as a reducing agent and a source of stabilizing species. The following physical and electrochemical techniques were utilized for the electrocatalyst characterizations: FTIR, TEM, XRD, Raman spectroscopy, EDX, CV, CA, CP, LSV and EIS.

## Chapter 3: Experimental

### 3.2 Chemicals and Materials

The chemicals and materials used in the preparation are listed in table 3.1.

**Table 3.1:** List of used chemicals and materials

<b>Chemicals &amp; materials</b>	<b>Specifications</b>	<b>Supplier</b>
Acetic anhydride	ACS, ISO, Reag Ph Eur	Merck
Carbon nanotubes- multiwalled	Bundles, $\geq 95\%$ as MWCNT, O.D $\times$ I.D $\times$ length, 7-15 nm $\times$ 3-6 nm $\times$ 0.5 – 200 $\mu\text{m}$	Aldrich
Ethanol (C <sub>2</sub> H <sub>5</sub> OH)	Absolute	Sigma - Aldrich
Ethylene glycol (OHCH <sub>2</sub> CH <sub>2</sub> OH)	Extra pure	Merck
Hydrogen peroxide (H <sub>2</sub> O <sub>2</sub> )	30 % by weight H <sub>2</sub> O <sub>2</sub>	Sigma - Aldrich
Hydrophilic polypropylene membrane filters	47 mm, 0.2 $\mu\text{m}$	Pall Corporation
Nafion® perfluorinated ion-exchange resin	5 wt% in mixture of lower aliphatic alcohols	Aldrich
Nickel chloride (NiCl <sub>2</sub> )	60 mesh 99.5 % pure	Cerac Incorporated

## Chapter 3: Experimental

---

Nitric acid ( $\text{HNO}_3$ )	65% extra pure	Merck
Palladium (II) chloride ( $\text{PdCl}_2$ )	-	SA precious metal
pH paper	pH 0-14	Merck
Potassium hydroxide ( $\text{KOH}$ )	ACS reagent > 85% (pellets)	Sigma - Aldrich
Sulfuric acid ( $\text{H}_2\text{SO}_4$ )	95 – 97 %	Sigma - Aldrich
Tin (II) Chloride dehydrate ( $\text{SnCl}_2 \cdot 2\text{H}_2\text{O}$ )	99.995 +%	Aldrich
Vulcan ® XC-72	-	Carbot

### **3.3 Instrumental Conditions**

This chapter gives a summary of the instrumental conditions used during the electrocatalyst characterizations.

#### **3.3.1 Fourier transform infrared spectroscopy**

The chemical structures of the raw MWCNT, carboxylated MWCNTs (AF-MWCNTs) and sulfonated MWCNT (SF-MWCNT) were analyzed by FTIR spectroscopy. The FTIR spectra were recorded using a Perkin Elmer Spectrum 100 FTIR spectrometer. The analysis was carried out using a diamond crystal probe and air was used as a background.

#### **3.3.2 Transmission Electron Microscopy**

TEM micrographs were obtained using a JEOL 2010 TEM system operating at 200 kV at the University of Pretoria. The TEM samples were prepared by suspending the electrocatalyst in ethanol, and then a drop of the suspension was cast onto the sample port for analysis.

#### **3.3.3 Energy dispersive x-ray spectroscopy**

The elemental composition of the electrocatalysts was investigated using an energy dispersive x-ray spectrometer. EDX spectra were obtained using the Noran Vantage (USA). The electrocatalyst

## Chapter 3: Experimental

---

powders were dispersed onto carbon sticks tabs and mounted on an aluminium holder which was then loaded into the spectrometer for analysis.

### **3.3.4 Raman spectroscopy**

Raman spectroscopy was used to monitor changes in the structural properties of the MWCNTs after the purification and functionalization processes. The Raman spectra were acquired using a Horiba Jobin Yvon HR800 micro Raman system in the back scattering mode. An (argon) Ar<sup>+</sup> laser emitter with a wavelength at 514.5 nm was used as an excitation source and an air cooled CCD detector was used.

### **3.3.5 X-ray diffraction**

The crystallinity of the electrocatalysts were determined using an X-ray diffraction spectrometer using a PANalytical X'Pert Pro diffractometer with CuK $\alpha$  radiation, with a wavelength of  $\lambda=1.5046$  Å as a radiation source operating at 45 kV and 40 mA. The XRD diffractograms were obtained in a scan range between 0 and 90°.

### 3.3.6 Electrochemical characterization conditions

All electrochemical experiments were carried out at room temperature in a standard three electrode electrochemical cell using using an Autolab potentiostat PGSTAT 302 (Eco Chemie, Utrecht, Netherlands) driven by the General Purpose Electrochemical Systems data processing software (GPES and FRA softwares version 4.9). The WE was a modified glassy carbon disk electrode (GCE, Bioanalytical systems, diameter = 3.0 mm). A Pt rod and Ag|AgCl, saturated KCl) were used as a CE and RE, respectively. EIS measurements were performed using Autolab Frequency Response Analyser (FRA) software between 100 kHz and 10 mHz with the amplitude (rms value) of the ac signal of 10 mV. All solutions were de-aerated by bubbling pure nitrogen prior to each electrochemical experiment.

### 3.4 Functionalization of the Multi-Walled Carbon Nanotubes

#### 3.4.1 Purification and oxidation of the MWCNTs

The MWCNTs were purified and COO-functionalized as described by Siswana *et al.* [88]. In this work, the procedure was slightly modified by reducing the time for refluxing the MWCNTs in HNO<sub>3</sub> solution to 24 hr in order to prevent extensive cutting or damage of the MWCNTs. 1 g of MWCNTs was added to 140 ml of 2.6 M HNO<sub>3</sub>, and the mixture was refluxed for 24 hr. The carbon nanotube sediment was separated from the solution using a centrifuge and washed with distilled water. The carbon nanotube sediment was then sonicated in a 3:1 mixture of H<sub>2</sub>SO<sub>4</sub> and HNO<sub>3</sub> for 24 hr. The sediment was thereafter washed with distilled water, stirred for 30 min in a 4:1 H<sub>2</sub>SO<sub>4</sub>/ H<sub>2</sub>O<sub>2</sub> mixture at 70 ° C, and then washed again with distilled water. The purified acid functionalized MWCNT paste was then dried in an oven at 110 ° C overnight to obtain the solid product (herein abbreviated as AF-MWCNTs).

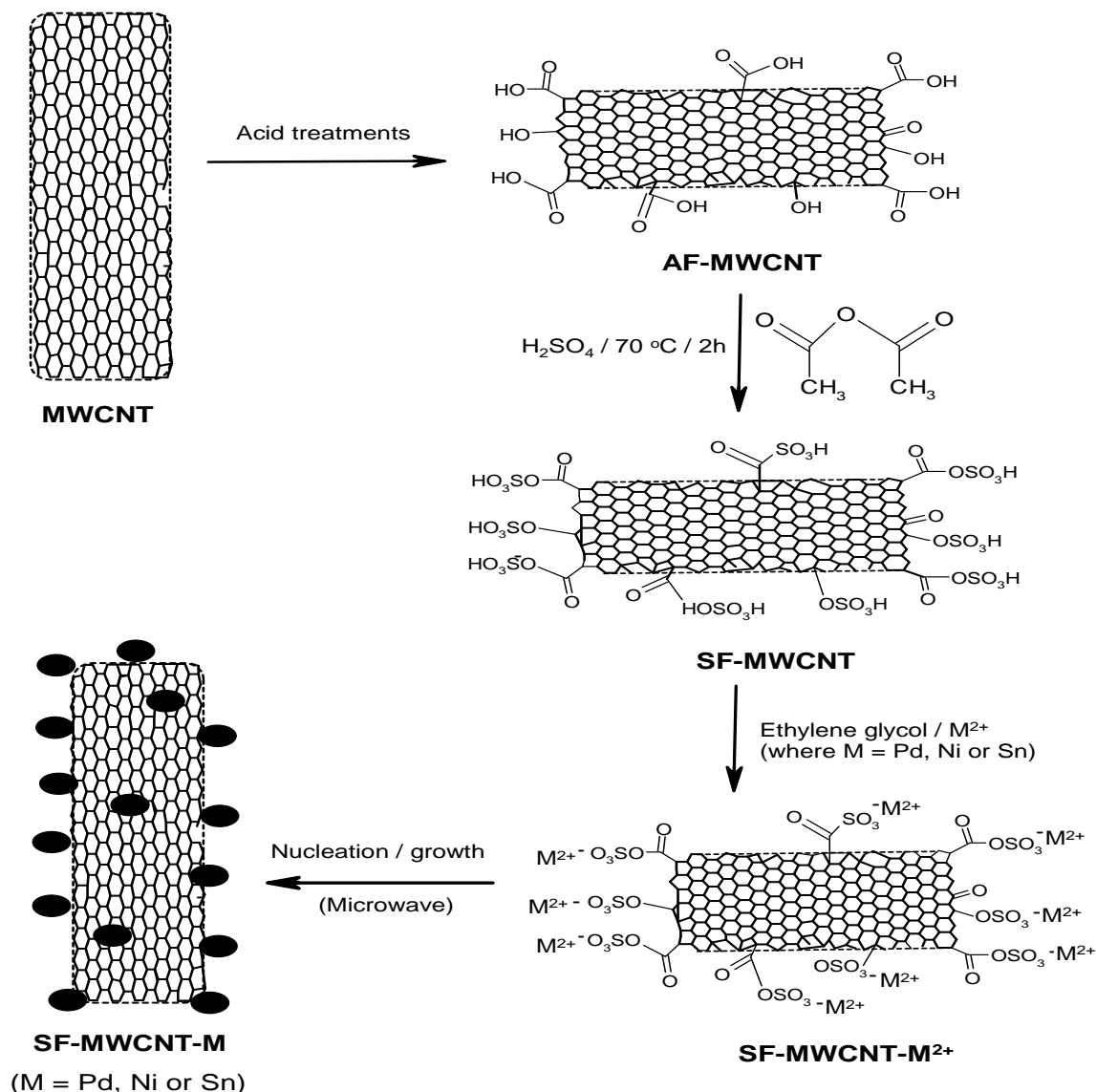
### 3.4.2 Sulfonation of the Multi-walled Carbon Nanotubes

The AF-MWCNTs (containing oxo-functional groups, mainly  $-\text{COOH}$ ) were sulfonated following the method described elsewhere [64]. 120 mg of the purified MWCNTs was added to a mixture of 20 ml of sulphuric acid ( $\text{H}_2\text{SO}_4$ ) and 300 ml of acetic anhydride ( $(\text{CH}_3\text{-CO})_2\text{O}$ ) holding continuous stirring at  $70\text{ }^\circ\text{C}$  for 2 hr. After 2 hr, the reaction mixture was allowed to cool and continuously stirred until room temperature. The resulting product (abbreviated herein as SF-MWCNT) was repeatedly washed with distilled water and dried at  $70\text{ }^\circ\text{C}$  overnight in an oven.

## Chapter 3: Experimental

### 3.5 Catalysts Syntheses

The metal (Pd, Ni and Sn) nanoparticles electrocatalyst were supported onto the walls of the SF-MWCNTs by adopting the microwave polyol process as reported in the literature [153], summarised in scheme 1.



**Scheme 1:** Schematic of the preparation of SF-MWCNT-M ( $M = \text{Pd, Ni or Sn}$ ) electrocatalysts using microwave-assisted method.

## Chapter 3: Experimental

---

The Pd and Pd-bimetallic electrocatalysts were prepared by microwave polyol process as reported in the literature [108,153]. 3.0 mL of 0.05 M aqueous PdCl<sub>2</sub> solution and 50 mL of EG were introduced into a 250 ml Erlenmeyer flask. The synthesis solution pH was adjusted to ~ 7.4 by adding 0.8 M aqueous KOH solution. 80 mg of SF-MWCNTs was then added into the above solution and ultrasonically dispersed in the solution for 1 h. The solution was then transferred into a liner-rotor 16 F100 TFM vessel, then placed in a microwave (Multiwave 3000 sample preparation system, 1400 Watts, Anton Paar) and heated using 1000 Watts at 170 °C for 60 s. The time taken to reach 170 °C was 13 min, after which the microwave was stopped and allowed to cool before the reaction vessel was removed. The resulting suspension was then filtered and the obtained residue was washed with acetone and distilled water. The final solid product (abbreviated herein as SF-MWCNT-Pd) was dried at 110 °C overnight in an oven. The SF-MWCNT-Sn and SF-MWCNT-Ni were prepared using the same procedure as for the SF-MWCNT-Pd, using 3.0 mL and 5.5 mL of the SnCl<sub>2</sub> and NiCl<sub>2</sub>, respectively. The ratios of Pd, Sn or Ni were controlled by stoichiometric calculation and confirmed by EDX measurements. Bimetallic PdSn alloyed electrocatalyst supported on vulcan (PdSn/C) was also prepared using a similar procedure, calculated amounts of PdCl<sub>2</sub> and SnCl<sub>2</sub> aqueous solutions were used to form the PdSn/C electrocatalyst. In this is instant two metals were used instead of

## Chapter 3: Experimental

---

one as done in preparing the SF-MWCNT-Pd electrocatalyst. The Pd-M electrocatalysts (mixtures) were obtained by physically mixing the SF-MWCNT-Pd powder with either SF-MWCNT-Ni or SF-MWCNT-Sn powder to form a mixed bimetallic electrocatalyst.

### 3.6 Electrode Modification

2 mg carbon material (AF-MWCNTs or SF-MWCNTs or Vulcan carbon) with or without Pd or Pd-M nanoparticles or nano-alloy was thoroughly dispersed in 2 ml ethanol and 100  $\mu$ L 5 % Nafion® solution with the aid of ultrasonic stirring (Bransonic 52 bath). To allow for proper mixing, each mixture was allowed to stay overnight after preparation before carrying out further experiment. A glassy carbon electrode (GCE) was polished to a mirror finish with an alumina slurry (nano powder, Aldrich) and then cleaned by ultrasonic stirring in acetone and distilled water for 3 min respectively. 10  $\mu$ L of the mixture (pre-sonicated again for about 1 min) was then cast onto the surface of the cleaned GCE. The electrode was then dried at 80 °C in an oven.

## Chapter 3: Experimental

---

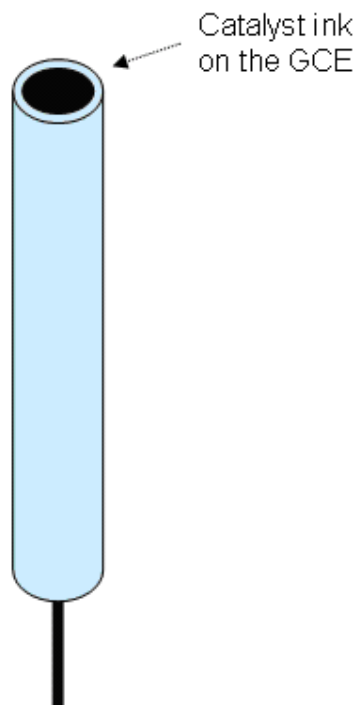


**Figure 3.1:** Schematic diagram of a modified GCE electrode

The following electrodes were studied: GCE modified with (a) SF-MWCNTs containing Pd alone (abbreviated as SF-MWCNT-Pd), (b) mixtures of SF-MWCNTs containing Pd and Ni (abbreviated as SF-MWCNT-PdNi<sub>mix</sub>), and (c) mixtures of SF-MWCNTs containing Pd and Sn (abbreviated as SF-MWCNT-PdSn<sub>mix</sub>). The alloy (abbreviated as AF-MWCNT-PdSn) was studied but gave poor performance compared to their mixtures (to be discussed later). The Pd loading of each electrode was maintained at 6.7  $\mu\text{g}$ .

### 3.7 CO- Stripping Measurements

A 0.5 M KOH electrolyte solution was purged by bubbling gaseous nitrogen for 15 min to remove dissolved oxygen. The CO was adsorbed by purging the KOH electrolyte solution with gaseous carbon monoxide for 30 min while keeping the electrode potential at -0.2 V vs. Ag|AgCl (sat. 3 M KCl). Gaseous nitrogen was then bubbled vigorously through the solution to remove any traces of dissolved CO.

## **CHAPTER FOUR**

### **RESULTS AND DISCUSSION\***

---

The following paper resulted from part of the research work presented in this thesis and is not referenced further. Also, oral and poster presentations resulting from this thesis are summarized in the Appendix (see page 186).

\* Tendamudzimu Ramulifho, Kenneth I. Ozoemena, Remegia M. Modibedi and Mkhulu K. Mathe, "Fast microwave-assisted solvothermal synthesis of metal nanoparticles (Pd, Ni, and Sn) supported on sulfonated MWCNTs: Electrocatalysts for ethanol oxidation in alkaline medium" [submitted].

### **The Significance of using the Microwave Synthetic Method**

Scheme 1 summarised the synthetic process adopted in this work. To our knowledge, this is the first time that a microwave-assisted synthetic method has been employed to support Pd, Ni and Sn nanoparticles onto sulfonate-functionalised MWCNTs. The same electrocatalysts can be synthesised by using other methods which are long processes requiring the use of reducing agents such as  $\text{NaBH}_4$  [154,155]. However, the microwave method is highly advantageous over the conventional chemical reduction methods as already indicated in chapter 2. The way in which the microwave heats the reactant is quite interesting; the heat is transferred directly into the reaction mixture. The microwave irradiation causes the dipoles' within the reaction liquid to rotate resulting in the alignment and relaxation of the polar molecules in the oscillating field of electromagnetic radiation which then causes the liquid to become hot [106].

The MWAS method provides a uniform nucleation environment and offers highly crystalline monodispersed metal nanoparticles. In this method, ethylene glycol (EG) was used as the solvent, as it can be rapidly heated by microwave radiation. EG was also used as agent, a stabilizer and a medium to prevent particles growth and

## Chapter 4: Results and discussion

---

agglomeration. The experimental temperature was 170 °C [108], as it is believed that EG is able to generate reducing species for the reduction of the metal ions to metallic particle in that temperature. The metal ions were coordinated with the functional groups (i.e., -COOH, -C=O, and -SO<sub>3</sub>H) on the SF-MWCNTs, functioning as nucleation precursors that are finally reduced to produce metal nanoparticles on the SF-MWCNTs. It is well known that the reaction mixture has a great influence on the stability and size of the metal particles. The work done by Zhao et al. [108] showed that EG can be oxidized to acetic acid at pH values of ~ 7.4 which then acts as a stabilizer. They explained the stabilizing mechanism as a by formation of the chelate-type complexes via its carbonyls groups [108]. Thus, in this work, the synthesis pH was increased to ~7.4 as reported by Zhao *et al.* [108].

## Chapter 4: Results and discussion

---

### 4.1 Spectroscopic and Microscopic Characterization

#### 4.1.1 Characterization of the Multi-Walled Carbon Nanotubes

##### 4.1.1.1 X-ray diffraction analysis

Figure 4.1 shows the XRD patterns of the MWCNT, AF-MWCNT and SF-MWCNT.

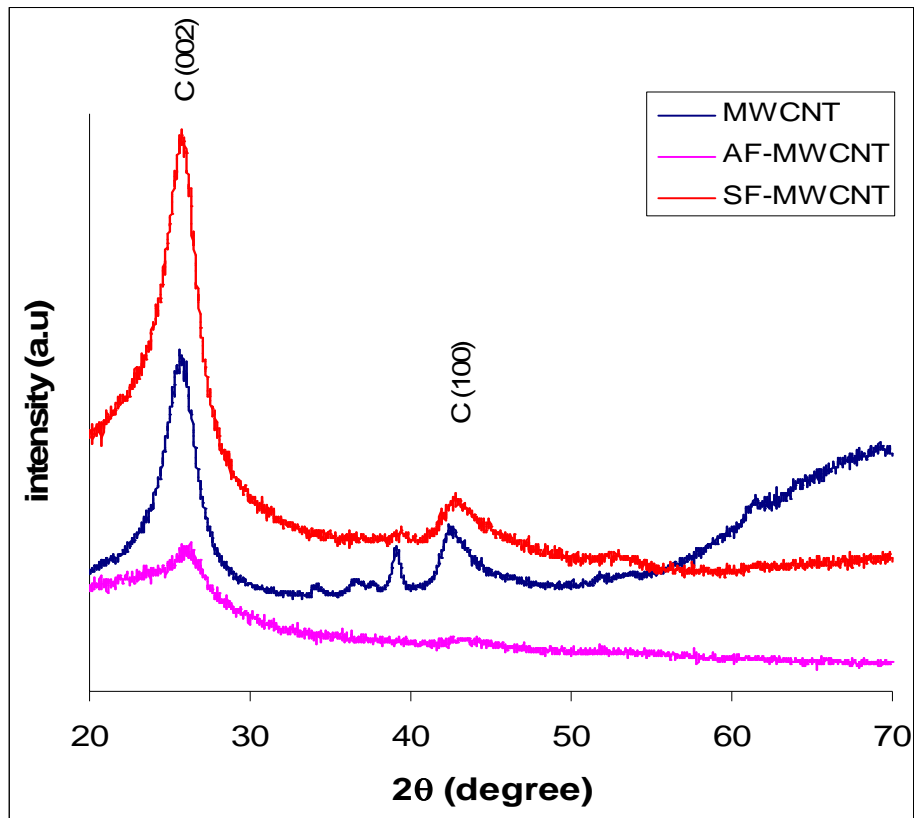


**Figure 4.1:** Comparative XRD patterns of (a) MWCNT, AF-MWCNT and SF-MWCNT.

## Chapter 4: Results and discussion

---

The diffraction peaks around  $25.8^\circ$  and  $43.1^\circ$  are attributed to the graphite structure (002) and (100) reflections of the MWCNT (JCPDS card No. 88-8487). The standard diffraction patterns as obtained from the (JCPDS card No. 88-8487) are  $26.5^\circ$  and  $42.5^\circ$ . The peaks observed in the range between  $2\theta$  angles  $30^\circ$  and  $40^\circ$  may be attributed to species introduced during the acid treatments. The AF-MWCNT is more crystalline, while the SF-MWCNT seems to be amorphous. Amorphous materials result in electrodes with high Tafel slopes.

### 4.1.1.2 Raman spectroscopy analysis

Figure 4.2 compares Raman spectra of the MWCNT, AF-MWCNT and SF-MWCNT. The D and G bands are the main important peaks used in analysing the quality of the carbon nanotubes. The principal two bands can be observed from the figure. The D band also known as the disorder or defect mode occurring at  $1346\text{ cm}^{-1}$  for the untreated MWCNT and G band (the graphite mode) occurring at  $1590\text{ cm}^{-1}$  for the untreated MWCNT. A third band was observed at  $\sim 2704\text{ cm}^{-1}$ , this band is known as the second order band (2D) [127]. The analysis of the D and G bands is important to trace defects in the structure of CNTs due to chemical processing [103]. Thus, in this study, the D and

## Chapter 4: Results and discussion

G bands were used to determine the quality of the MWCNTs by comparing their D/G ratios as described by [103]. After the acid treatment (AF-MWCNT), the D and G bands shifted in the direction of higher wavelengths with respect to the untreated MWCNT. However, after the sulfonation process, both D and G bands shifted in the direction of lower wavelengths as compared to the AF-MWCNT.

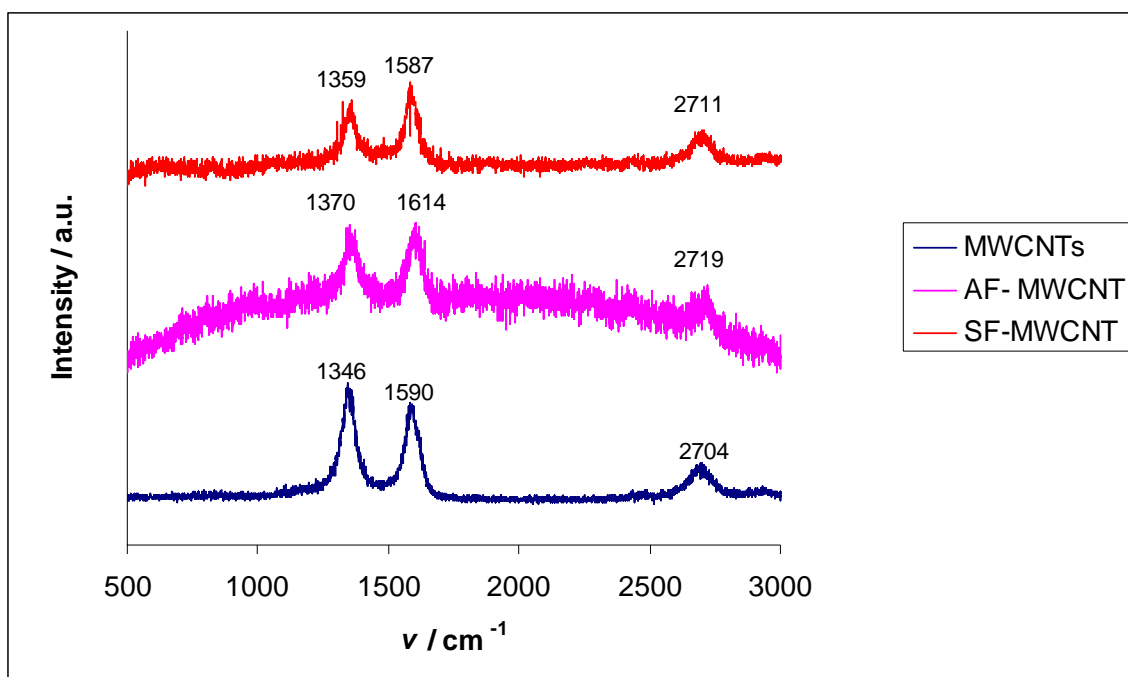


**Figure 4.2:** Raman spectra of MWCNT, AF-MWCNT and SF-MWCNT.

The SF-MWCNT have a sharper and narrower G band which is more intense than its D band as compared to that of AF-MWCNT (D and G band are of same intensities) and MWCNT (D band is more intense

## Chapter 4: Results and discussion

---

than the G band. The shifts in the D and G band and the change in the intensities of the D and G band can be associated with the introduction of defects in the structure of the MWCNTs as a result of the modification processes. The quality of the MWCNTs was evaluated using the  $I_D/I_G$  ratio. The  $I_D/I_G$  ratio is an indication of the graphitization degree of the MWCNTs due to the oxidation processes [103]. A large quantity of structural defects is indicated by similar intensities [129]. The  $I_D/I_G$  ratio was calculated to be 0.85 for the untreated and AF-MWCNT; and 0.86 for the SF-MWCNT. These ratios suggest similar degree of graphitization of the MWCNTs.

### **4.1.1.3 Fourier transform infrared spectroscopy analysis**

Figure 4.3 shows the FTIR spectra of the MWCNT, AF-MWCNT and SF-MWCNT respectively.

## Chapter 4: Results and discussion

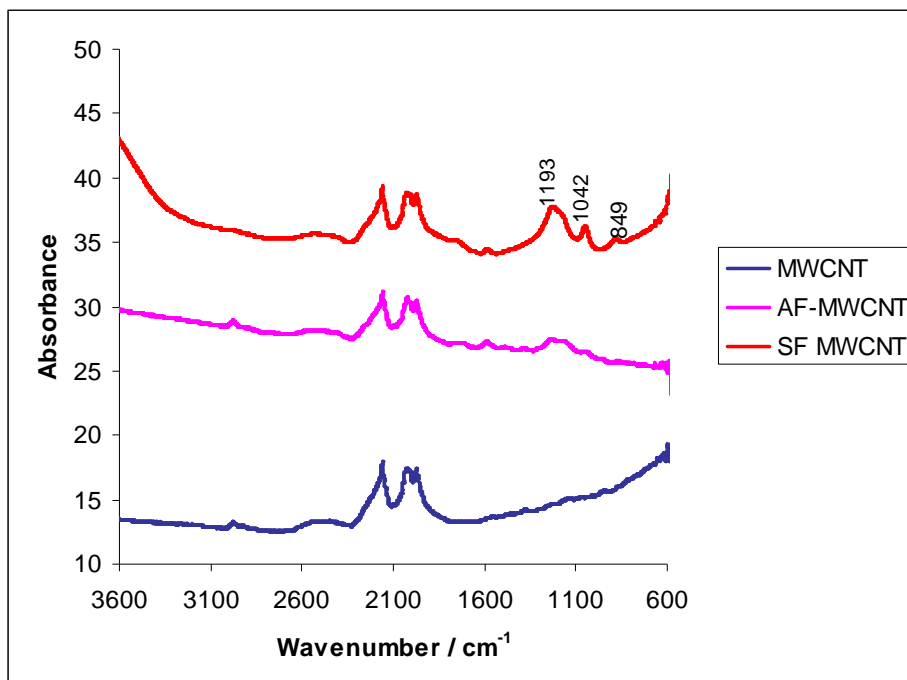


**Figure 4.3:** FTIR spectra of MWCNT, AF-MWCNT and SF-MWCNT.

The successful grafting of the sulfonic acid groups onto the SF-MWCNT was further confirmed by using FTIR spectroscopy. In comparison to the MWCNT and the AF-MWCNT, the FTIR spectra of SF-MWCNT exhibited additional bands at 860, 1041 and 1169  $\text{cm}^{-1}$ , which could be attributed to the  $-\text{SO}_3$  peaks of the sulfonic acid groups [156]. These representative absorption bands indicated that the sulfonic acid groups were successfully grafted on the surface of the SF-MWCNT. The multiple bands observed around  $\sim 2100 \text{ cm}^{-1}$  on all the spectra can be attributed to the carbon-carbon bonds of the alkynes groups on the MWCNTs [157,158].

## Chapter 4: Results and discussion

### 4.1.1.4 Transmission electron microscopy images

Figure 4.4 shows the TEM images of the MWCNTs. As can be seen in the figure, as the MWCNT were being functionalized, some defects were being created on the structure of the MWCNT. This is indicated by the visible roughness on the MWCNT. The SF-MWCNT, figure 12 (c) show more defects on the MWCNTs.

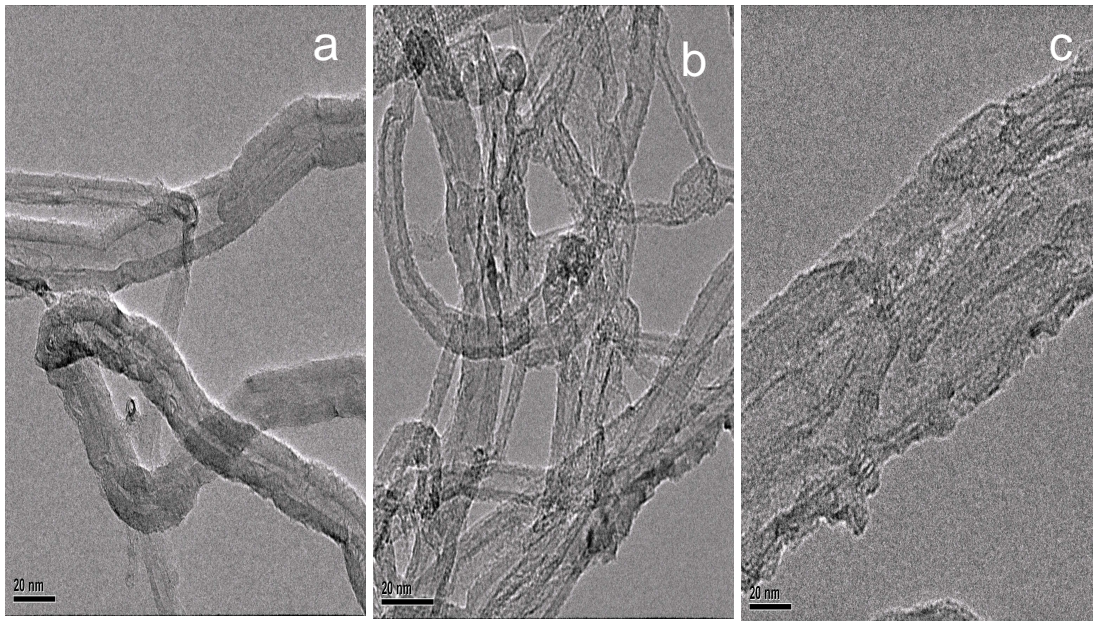


**Figure 4.4:** TEM images of the (a) MWCNTs, (b) AF-MWCNTs and (c) SF-MWCNTs

### 4.1.2 Characterization of the electrocatalysts

#### 4.1.2.1 X-ray diffraction analysis

Figure 4.5 compares XRD patterns of the three electrocatalysts (SF-MWCNT-Pd), SF-MWCNT-Ni and SF-MWCNT-Sn). The three electrocatalysts were chosen as they are the main electrocatalysts that are using in preparing the mixed electrocatalysts. The mixed electrocatalyst is prepared by physically mixing the SF-MWCNT-Pd and SF-MWCNT-Ni electrocatalyst or the SF-MWCNT-Pd and SF-MWCNT-Sn electrocatalyst. The XRD peaks of SF-MWCNT-Pd, SF-MWCNT-Ni and SF-MWCNT-Sn electrocatalyst clearly indicate that the metal particles were successfully reduced and supported onto the SF-MWCNTs surface. The diffraction peaks of the Pd are well defined and can be matched to the (111), (200), and (220) reflections of a palladium face-centred cubic (fcc) crystal structure (JCPDS card No. 88-2335). The standard diffraction patterns of pure metals occurs at  $40.0^\circ$  (111),  $46.5^\circ$  (200) and  $67.90^\circ$  (220). The intensity ratio of the crystal planes (111): (200): (220) is 4: 2: 1.

## Chapter 4: Results and discussion

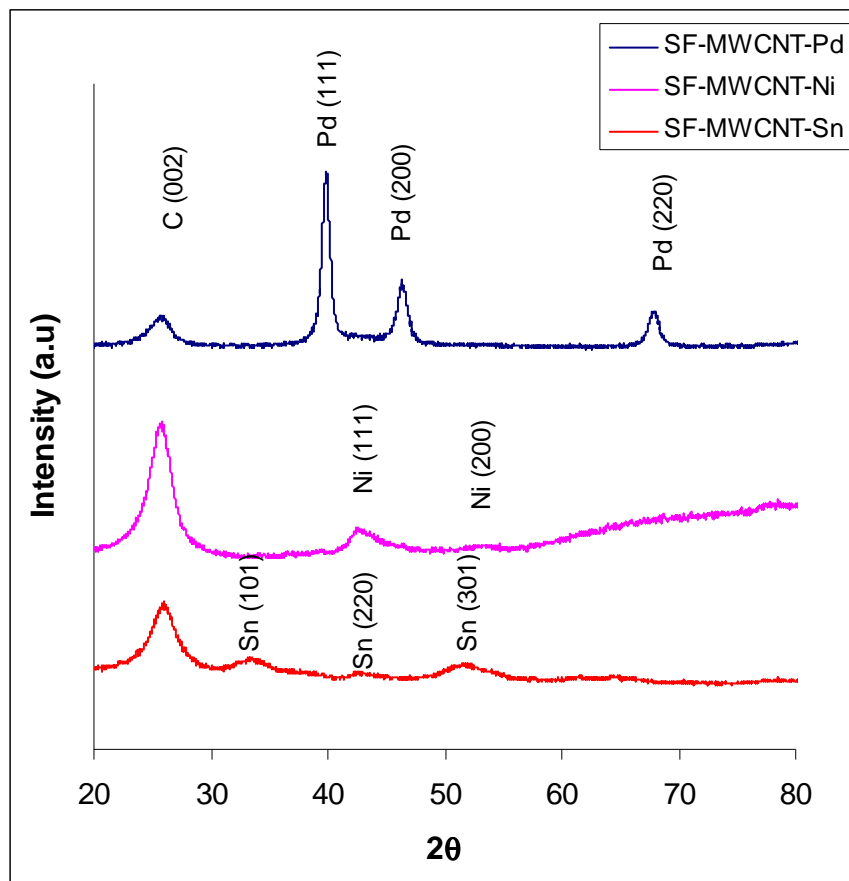


**Figure 4.5:** Comparative XRD patterns of SF-MWCNT-Pd, SF-MWCNT-Ni and SF-MWCNT-Sn.

The peak C (002) is attributed to the supporting MWCNTs matrix occurring at  $26.6^\circ$  for the pure metal. Unlike Pd, the crystalline peaks for the Ni (JCPDS card No. 88-2326) occurring at  $45.5^\circ$  (111) and  $53.0^\circ$  (200) for the pure metals and Sn (JCPDS card No. 65-7657) occurring at  $32.0^\circ$  (101),  $43.8^\circ$  (220) and  $55.3^\circ$  (301) for the pure metal are less pronounced, suggesting poor crystallinity or amorphous structures. In this work palladium is the main element active towards

## Chapter 4: Results and discussion

---

ethanol and ethylene glycol oxidation in alkaline medium since tin and nickel alone cannot oxidize these alcohols. Thus, the particle size determination was focused on the SF-MWCNT-Pd.

The average crystallite size for the SF-MWCNT-Pd electrocatalyst was calculated using the Debye-Scherrer formula [159,160] :

$$d = \frac{K\lambda}{B \cos \theta} \quad (4.1)$$

where  $d$  = average crystal size;  $K$  = a constant (0.89);  $\lambda$  = wavelength,  $B$  is the full width at half maximum of the peak and  $(\theta)$  is the Bragg's angle of the XRD peak. The crystallite size of the Pd particle as calculated from the Pd (111) peak is  $\sim 30$  nm. The catalyst particles are agglomerated on the nanotubes as can be seen on the TEM images (figure 4.6), which causes the average crystallite size to be big. However, different crystallite sizes were obtained using the other peaks; Pd (200) = 15.4 nm and Pd (220) = 10.2 nm. Thus, it is difficult to determine the precise crystallite size due to agglomeration. It should be noted that crystallite size determination is a broad field of study. Uvarov et al. [116] have indicated that there is no common opinion on the advantages and disadvantages of different XRD methods for the crystallite size determination. They also indicated that

## Chapter 4: Results and discussion

---

the crystallite sizes obtained from different XRD methods differ. The different methods that can be used for crystallite size determination are discussed on the literature review. The Debye-Scherrer method was used in this study as it is commonly used in fuel cell electrocatalyst determination. The K constant was also used as 0.89 since the particle shape was not clear due to agglomeration. The TEM technique could not be used to complement the XRD results due to the metal particles agglomeration as seen on the TEM images. Different XRD methods will be investigated in future to determine the crystallite sizes.

### **4.1.2.2 Transmission electron microscopy analysis**

Figure 4.6 shows the TEM images of the SF-MWCNT-Pd, SF-MWCNT-Ni and SF-MWCNT-Sn. The images show that the metal catalysts are satisfactorily dispersed onto the walls of the SF-MWCNTs. In addition the crystallinity of the Pd and the amorphous nature of the Sn and Ni are visible.

## Chapter 4: Results and discussion

---

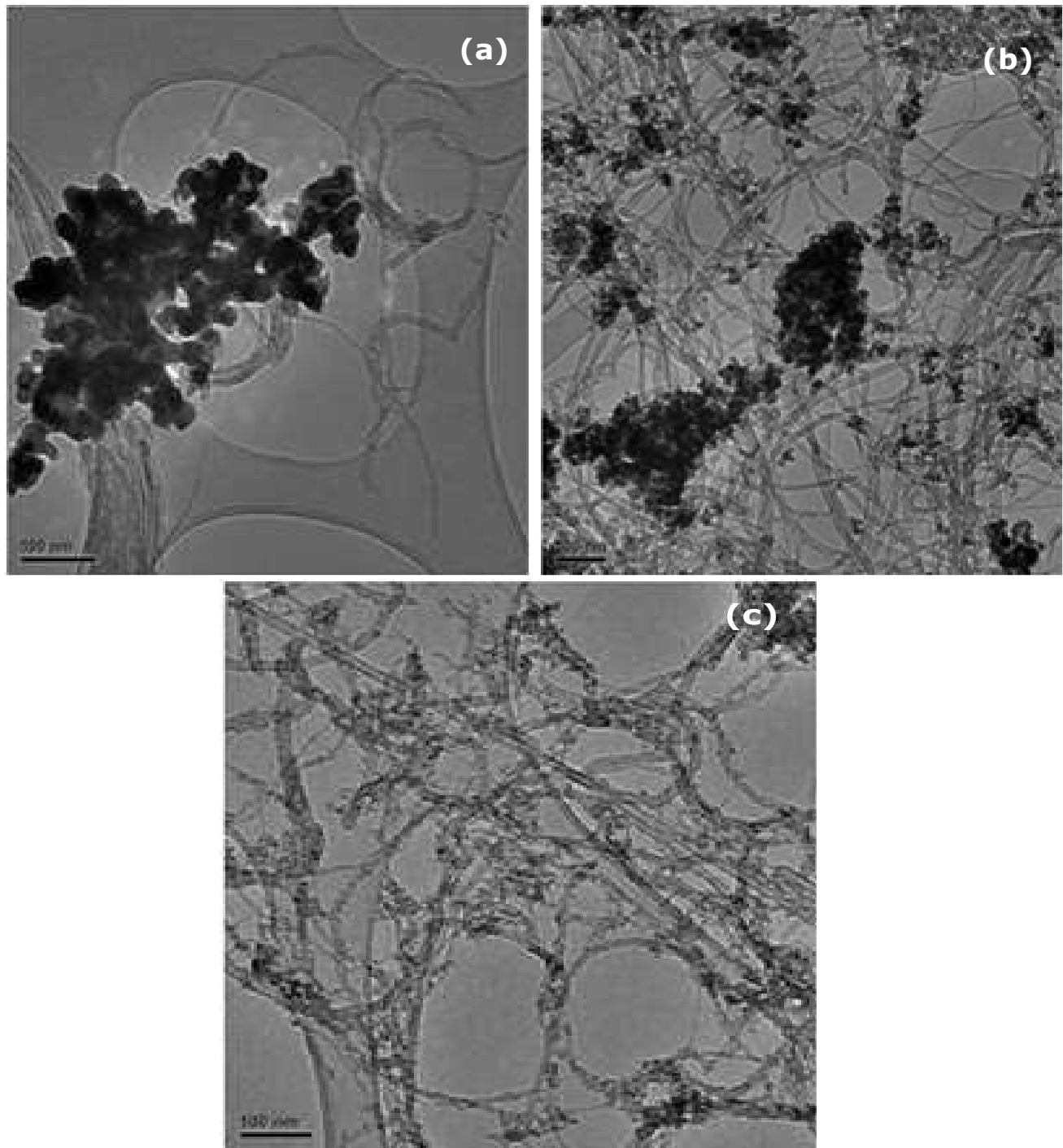


**Figure 4.6:** Comparative TEM images of SF-MWCNT-Pd, SF-MWCNT-Ni and SF-MWCNT-Sn at 100 nm magnification.

## Chapter 4: Results and discussion

---

### 4.1.2.3 Energy dispersive X-ray spectroscopy analysis

Figure 4.7 shows the EDX profiles of the prepared electrocatalysts, (a) SF-MWCNT-Pd, (b) SF-MWCNT-Sn and (c) SF-MWCNT-Ni. The presence of oxygen peaks on all the EDX spectra is an indication of the successful modification of the MWCNTs to the acid derivatives MWCNTs-COOH while the sulphur peaks are an indication of the successful modification of the oxidized MWCNTs with the sulfonic acid groups to form SF-MWCNTs. The presence of the Cl molecules is due to the presence of the precursors, it would not affect the electrochemical performance as it is inactive towards alcohol electro-oxidation. The EDX results are summarised in Table 4.1.

## Chapter 4: Results and discussion

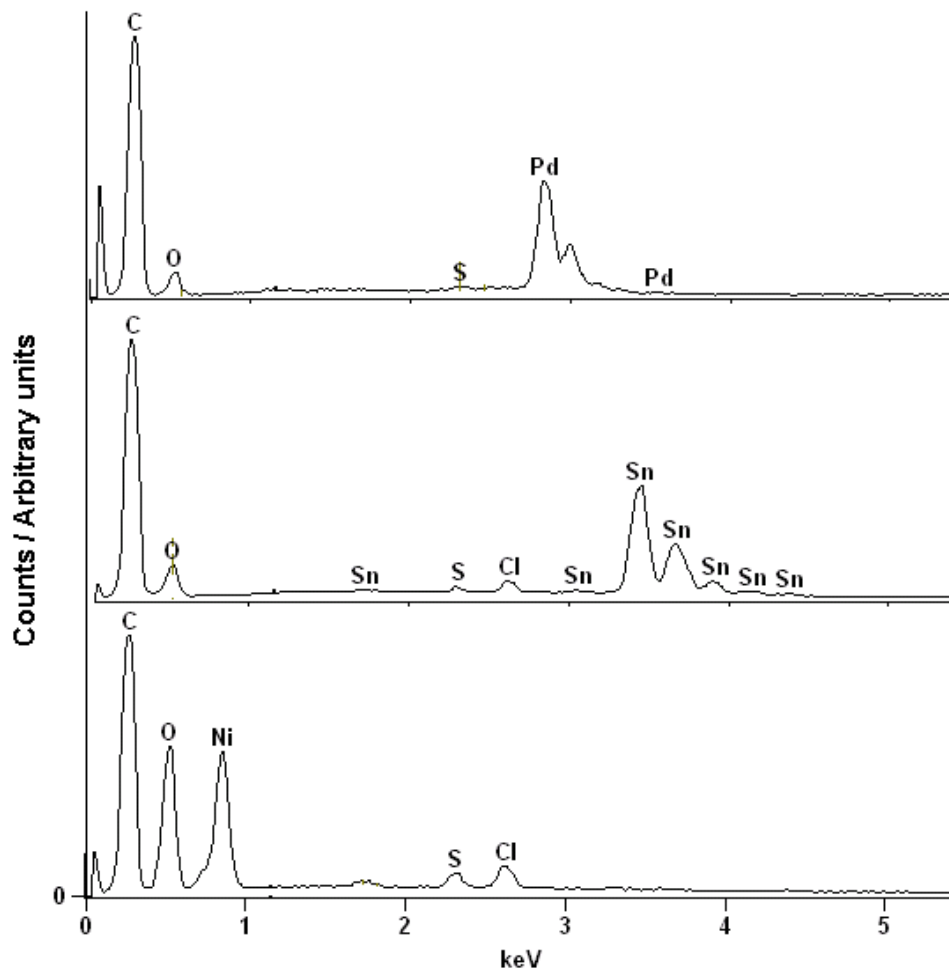


**Figure 4.7:** EDX patterns of SF-MWCNT-Pd, SF-MWCNT-Ni and SF-MWCNT-Sn.

## Chapter 4: Results and discussion

---

**Table 4.1:** Composition of the prepared electrocatalysts.

<b>Catalyst</b>	SF-MWCNT-Pd	SF-MWCNT-Ni	SF-MWCNT-Sn
<b>Weight %</b>	24.61 (± 0.30)	16.42 (± 0.21)	25.13(± 0.26)
<b>Atomic %</b>	3.77 (± 0.05)	4.35 (± 0.06)	3.60 (± 0.04)

## Chapter 4: Results and discussion

---

### 4.2 Electrochemical characterization

#### 4.2.1 The effect of support on the catalytic performance

The support material plays a vital role on the performance of the fuel cell electrocatalyst as indicated on the literature review. Many fuel cell electrocatalysts are supported on vulcan. In this studies, PdSn alloyed electrocatalyst was prepared and supported on carbon vulcan XC-72 (abbreviated C-PdSn), carboxylated MWCNT (abbreviated AF-MWCNT-PdSn) and Sulfonated MWCNT (abbreviated SF-MWCNT-PdSn); and tested for ethanol oxidation in alkaline medium to investigate the effect of these different supports. Figure 4.8 shows cyclic voltammograms of the C-PdSn, AF-MWCNT-PdSn and SF-MWCNT-PdSn in 0.5 M EtOH and 0.5 M KOH solutions. It can be observed that the SF-MWCNT-PdSn electrocatalyst showed the highest current density for ethanol oxidation in alkaline medium. This result agrees with previous work done by Zheng *et al.* [48] who showed an enhanced catalytic performance of an electrocatalyst supported on MWCNT. The results indicated that the sulfonated MWCNTs give the best electrocatalytic activity in terms of low onset potential and high current density when compared to the commercially available vulcan or the carboxylated MWCNTs. The high activity of CNTs originates from their edge plane like-sites/defects [74,161]. Thus, all subsequent studies

## Chapter 4: Results and discussion

were devoted to the metal electrocatalysts supported on the SF-MWCNTs.

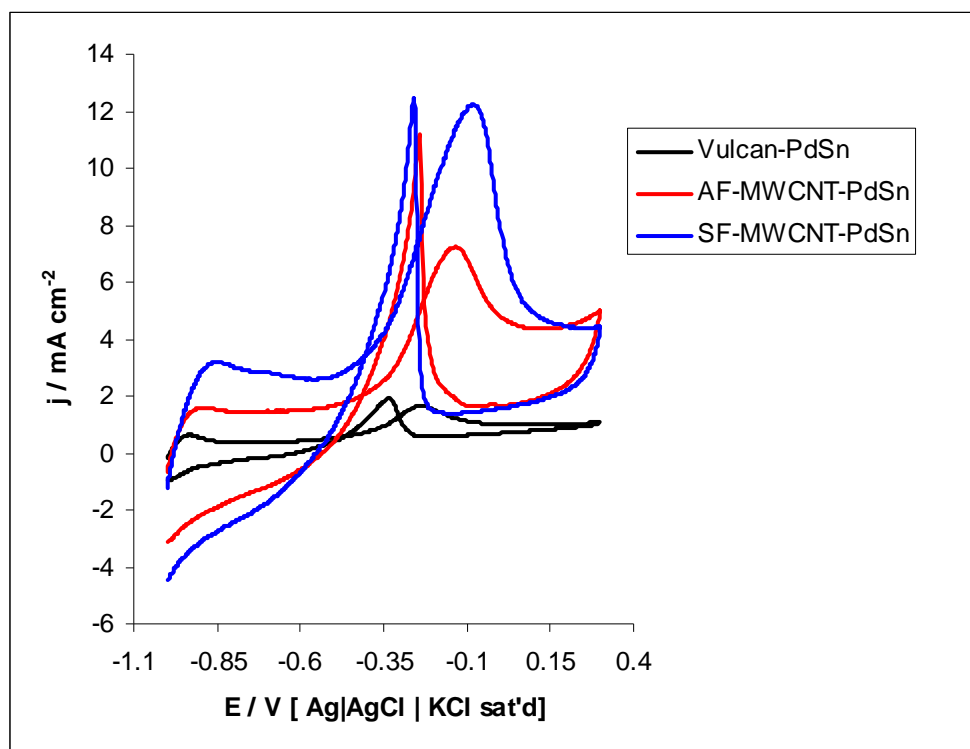


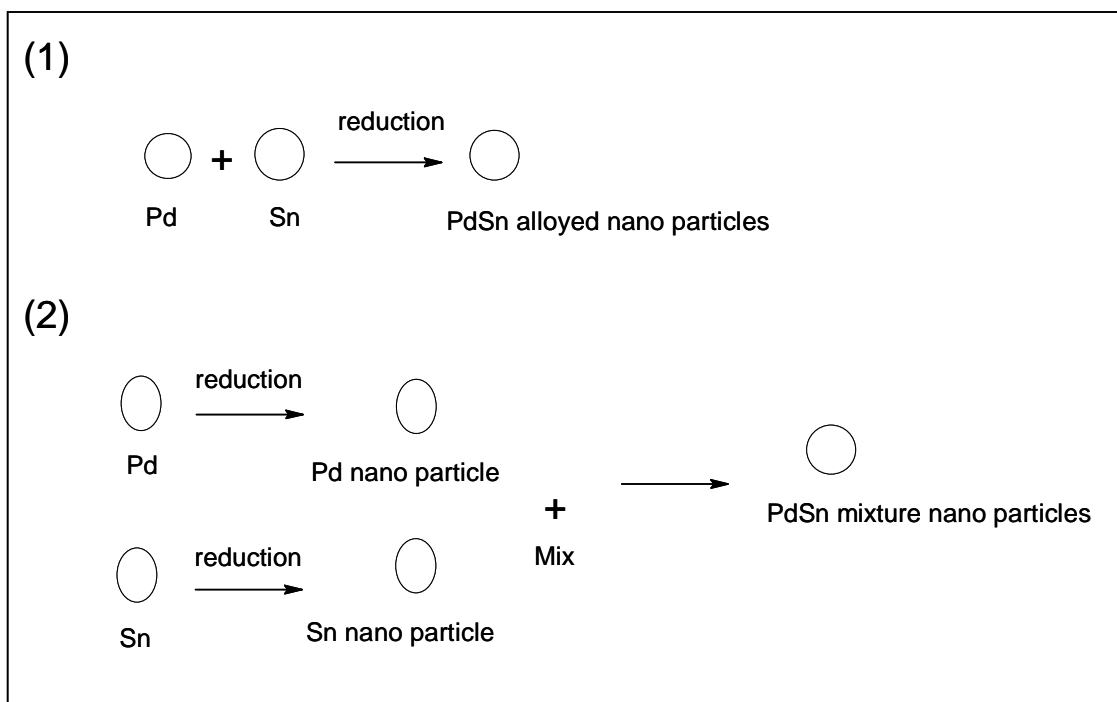
**Figure 4.8:** Cyclic voltammograms of C-PdSn, AF-MWCNT-PdSn and SF-MWCNT-PdSn (at the fourth cycle) in 0.5 M KOH + 0.5 M EtOH solutions. Scan rate:  $50\text{mVs}^{-1}$ .

### 4.2.2 The effect of the method of preparing bi-metallic electrocatalysts

The method in which a catalyst is prepared also plays an important role in its performance. Two methods of bi-metallic electrocatalyst combination were investigated, namely (1) Reducing the metal

## Chapter 4: Results and discussion

particles together to form an alloyed bi-metallic electrocatalyst and (2) Co-reducing the metals (separately) and mixing them after reduction to form a mixture of a bi-metallic electrocatalyst. The two methods are shown in scheme 2.



**Scheme 2:** Schematic diagram of the two methods of preparing bi-metallic electrocatalysts.

Figure 4.9 shows a cyclic voltammogram of the alloyed (C-PdSn, AF-MWCNT-PdSn and SF-MWCNT-PdSn) electrocatalyst and SF-MWCNT-PdSn<sub>mix</sub> (mixture) electrocatalyst in 0.5 M EtOH and 0.5 M KOH solutions. It is clear that the mixture exhibits the most pronounced enhanced catalytic activity towards ethanol oxidation than the alloyed

## Chapter 4: Results and discussion

PdSn electrocatalysts, implying that alloying impedes ethanol electro-oxidation presumably due to the inhibition of the ethanol adsorption/dehydrogenation process on Pd.

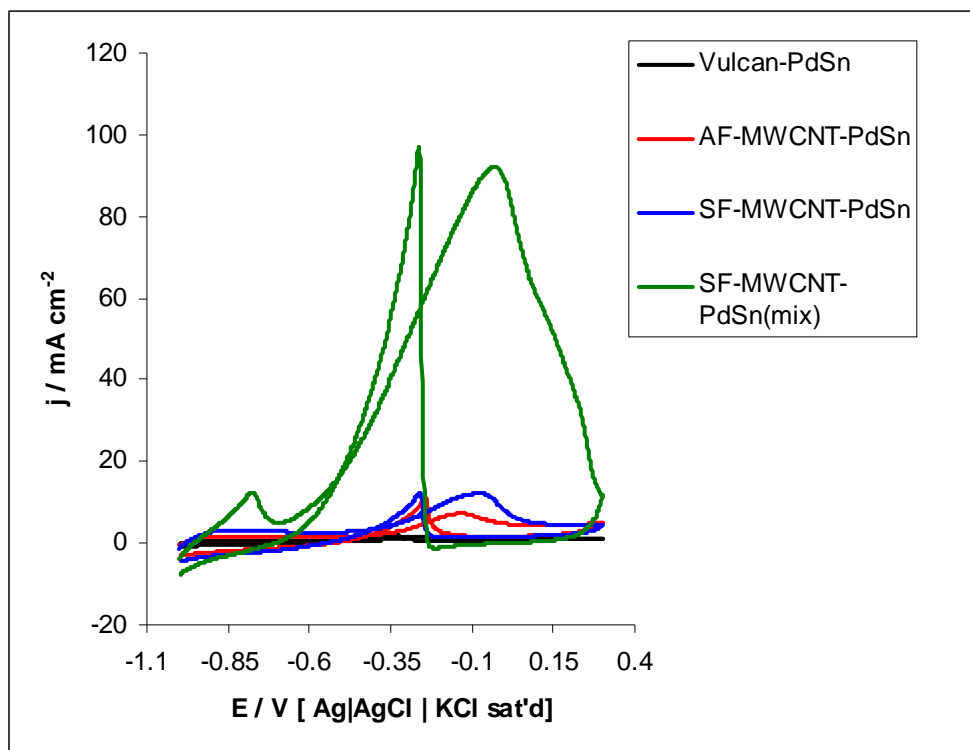


**Figure 4.9:** Cyclic voltammograms of C-PdSn, AF-MWCNT-PdSn and SF-MWCNT-PdSn and SF-MWCNT-PdSn<sub>mix</sub> (at the fourth cycle) in 0.5 M KOH + 0.5 M EtOH solutions. Scan rate:  $50\text{mVs}^{-1}$ .

Recently, Gupta *et al.* [161] also observed that unalloyed Sn promoted the oxidation of ethanol in PtSn binary catalysts, and attributed this to a possible inhibition of ethanol adsorption/ dehydrogenation on Pt. Based on this finding; all subsequent experiments were devoted to the use of the mixtures rather than the alloyed electrocatalysts.

## Chapter 4: Results and discussion

---

### 4.2.3 Electrochemically active surface area determination

It is of great importance to determine the electrochemically active surface area (EASA) of an electrode as its activity is not only controlled by its catalytic properties but also by the surface area. Below is a comparative determination of electrochemically active surface area using different methods.

#### (i) Hydrogen desorption method

Figure 4.10 shows the electrochemical reactivity and the electrochemical active surface (EAS) areas of the SF-MWCNT-Pd, SF-MWCNT-PdNi<sub>mix</sub> and SF-MWCNT-PdSn<sub>mix</sub> electrocatalysts determined by a CV (after the fourth cycle) measurement performed in 0.5 M KOH electrolyte at a scan rate of 50 mV s<sup>-1</sup>. The forward and reverse peaks (I) and (II) in the potential range -0.9 and -0.7 V are the hydrogen desorption and adsorption peaks. Peak (III) can be attributed to the formation of palladium oxide layer on the surface of the catalysts and peak (IV) can be attributed to the reduction of the Pd (II) oxide layer during the reverse sweep [24]. As seen in figure 4.10, the hydrogen desorption peaks of the SF-MWCNT-PdNi<sub>mix</sub> and SF-MWCNT-PdSn<sub>mix</sub> catalysts are both larger than those of the SF-MWCNT-Pd catalyst.

## Chapter 4: Results and discussion

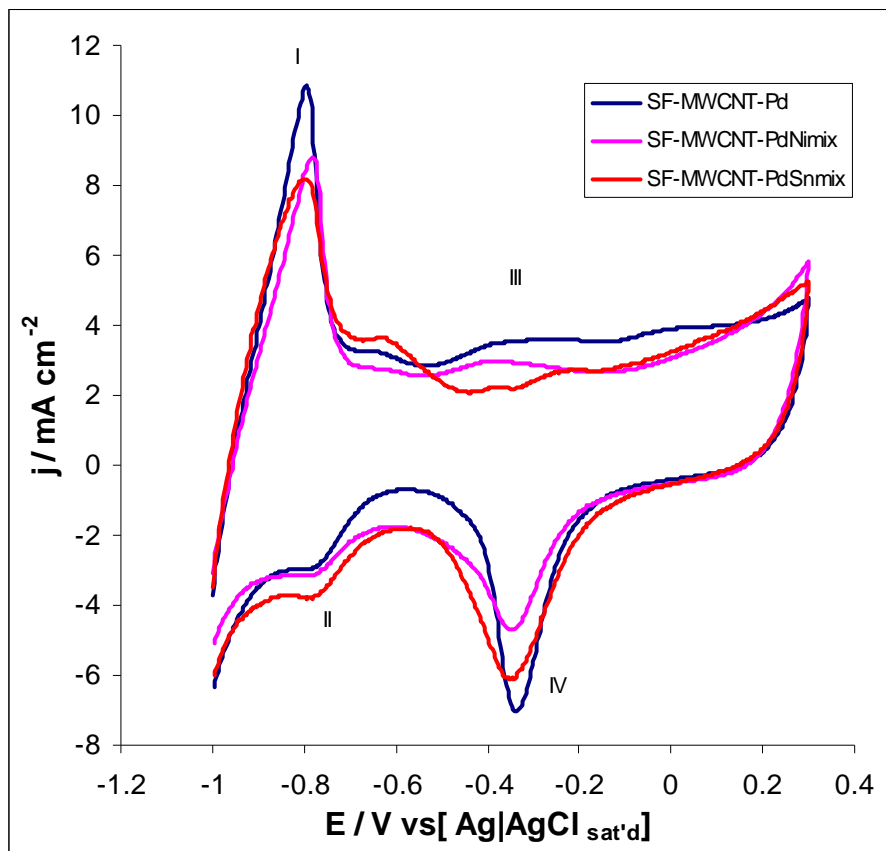


**Figure 4.10:** Cyclic voltammograms of SF-MWCNT-Pd, SF-MWCNT-PdNi<sub>mix</sub> and SF-MWCNT-PdSn<sub>mix</sub> (at the fourth cycle) in 0.5 M KOH solution. Scan rate: 50 mVs<sup>-1</sup>.

The Coulombic amount ( $Q$ ) which is associated with the peak area can be used to calculate the electroactive surface area (EASA) using the following equation and a conversion factor of 210  $\mu\text{C cm}^{-2}$  [162-164].

$$\text{EASA} = \frac{Q}{m.C} \quad (4.2)$$

## Chapter 4: Results and discussion

---

where  $C$  = the quantity of electricity when hydrogen molecules are adsorbed on palladium with a homogeneous and single layer ( $C = 210 \mu\text{C}\cdot\text{cm}^2$ ); and  $m$  = mass of palladium on the catalyst surface.

The EASA values of the different electrocatalysts are summarized on Table 4.2. The EASA values of the three electrocatalyst are high which indicates that they are active for alcohol oxidation. Further electrochemical investigations (see further topics on the electrochemical studies) revealed that the SF-MWCNT-PdNi<sub>mix</sub> and SF-MWCNT-PdSn<sub>mix</sub> show better electrochemical performance towards alcohol oxidation in alkaline medium.

## Chapter 4: Results and discussion

---

**Table 4.2:** Electrochemically Active Surface Area of the catalysts

Catalyst	EASA ( $\text{m}^2\text{g}^{-1}$ Pd) H <sub>2</sub>	S <sub>co</sub> ( $\text{m}^2\text{g}^{-1}$ Pd) CO	EASA ( $\text{m}^2\text{g}^{-1}$ Pd) PdO
SF-MWCNT-Pd	183.70	-	60.44
SF-MWCNT-PdNi <sub>mix</sub>	163.89	35.61	58.82
SF-MWCNT-PdSn <sub>mix</sub>	212.08	20.00	76.58

### (ii) CO adsorption method

The SF-MWCNT-PdNi<sub>mix</sub> and SF-MWCNT-PdSn<sub>mix</sub> electrocatalysts were further characterized in alkaline solution in the presence of CO. Figure 4.11 shows the CO stripping voltammograms of the catalysts in the absence and presence of CO in 0.5 M KOH solution.

## Chapter 4: Results and discussion

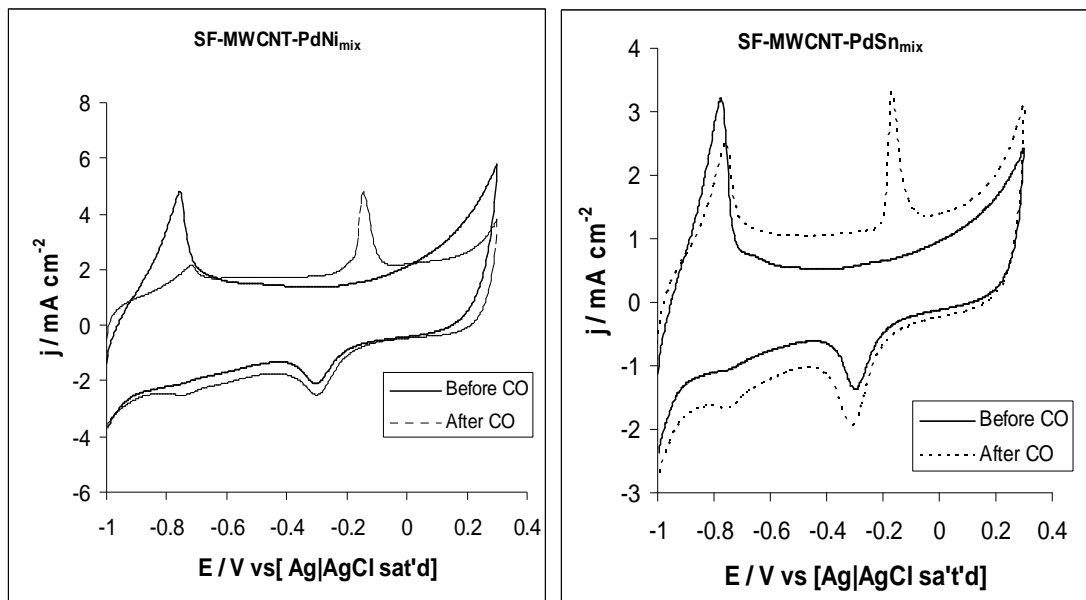


**Figure 4.11:** CO stripping voltammograms of SF-MWCNT-PdNi<sub>mix</sub> and SF-MWCNT-PdSn<sub>mix</sub> (at the fourth cycle) in 0.5M KOH. Scan rate: 50mVs<sup>-1</sup>.

As observed in Figure 4.11, the CO stripping onset potential of SF-MWCNT-PdNi<sub>mix</sub> electrocatalysts is more negative (-0.2402 V) in comparison to that of SF-MWCNT-PdSn<sub>mix</sub> (-0.2036 V) catalyst. This is an indication that the presence of Ni in the SF-MWCNT-PdNi<sub>mix</sub> was helpful to weakening the CO adsorptive bond on the Pd active sites through the interaction between the Pd and Ni particles than the Sn in the SF-MWCNT-Pd Sn<sub>mix</sub> electrocatalyst. It also means that the removal of CO on SF-MWCNT-PdSn<sub>mix</sub> is more difficult than that on SF-MWCNT-PdNi<sub>mix</sub> electrocatalyst. The CO oxidation potential of SF-

## Chapter 4: Results and discussion

---

MWCNT-PdNi<sub>mix</sub> electrocatalyst occurred at a more negative potential (-0.169 V) as compared to that of SF-MWCNT-PdSn<sub>mix</sub> (-0.139 V).

The CO surface area  $S_{CO}$  as measured by the integrated CO-oxidation peak areas were calculated using the following equation [165,166]

$$S_{CO} = \frac{Q_{CO}}{Q_{ml} * M_{pd}} \quad (4.3)$$

where  $Q_{CO}$  = CO stripping charge;  $Q_{ml}$  = charge associated with oxidation of adsorbed CO monolayer (0.420 mC cm<sup>-2</sup>) [167,168] and  $M_{pd}$  = metal loading in the catalyst layer.

The obtained values are summarized in table 4.2. The values of the surface area obtained using this method is lower than those obtained from the hydrogen adsorption method. Vidakovi'c *et al.* [168] also found different values of the EASA from the two methods and concluded that the hydrogen adsorption method gives the maximum number of surface reactive sites as one of the uncertainties in the CO surface area determination is the type of the CO bonding on the surface. SF-MWCNT-PdNi<sub>mix</sub> showed higher CO surface area as compared to the SF-MWCNT-PdSn<sub>mix</sub>.

### (iii) Pd-Oxide layer method

Figure 4.10 shows the cyclic voltammograms of SF-MWCNT-PdNi<sub>mix</sub> and SF-MWCNT-PdSn<sub>mix</sub> electrocatalysts in 0.5 M KOH electrolyte solution at a scan rate of 50 mv s<sup>-1</sup>. The peak observed during the reverse scan which appears at E = -0.365 V corresponds to the reduction of palladium (II) oxide into a Pd metal. The EASA was determined using the total charge (Q) involved in the complete reduction of Pd-Oxide into Pd metal using the following equation [169]

$$EASA = \frac{Q}{SI} \quad (4.4)$$

where S = charge associated with the reduction of Pd-O monolayer (405 μCcm<sup>-2</sup>) [170] ; I = catalyst loading; Q = value estimated by integrating the Pd-O peak.

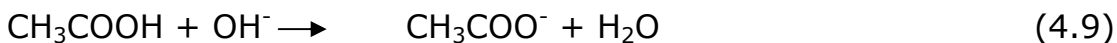
The SF-MWCNT-PdSn<sub>mix</sub> electrocatalyst showed the highest EASA from the PdO layer method. In conclusion, all the three electrocatalysts have good EASA values. Their electrochemical performances towards alcohol oxidation were further investigated and are reported on the sections that follow.

## Chapter 4: Results and discussion

---

### 4.3 Electrocatalysis towards Ethanol Oxidation in Alkaline Medium

The prepared electrocatalysts were evaluated for their electrocatalytic behaviour towards ethanol oxidation in alkaline medium. However, the mechanism of ethanol oxidation is still a subject of some controversy [24,171,172] as it involves intermediate products (such as linearly adsorbed CO and CO<sub>2</sub>, CH<sub>x,ads</sub> species [37,159,173-176] and final products (such as CO<sub>2</sub>, acetaldehyde and acetic acid [37,175]. However, recent reports [24,176] on Pd and Pd/Ti based electrocatalyst for ethanol oxidation in alkaline medium simplified the mechanistic steps as follows:



Equation 4.5 and 4.6 describe the dissociative adsorption of ethanol on the catalyst surface. Equation 4.8 represents the rate-determining step, meaning that the degree of ethanol oxidation is dependent on the coverage of the CH<sub>3</sub>CO<sub>ads</sub> and OH<sub>ads</sub> on the surface of the catalyst.

## Chapter 4: Results and discussion

---

### 4.3.1 Comparative electrocatalytic oxidation of ethanol in alkaline medium

Figure 4.12 shows the voltammetric responses of SF-MWCNT-Pd, SF-MWCNT-PdNi<sub>mix</sub> and SF-MWCNT-PdSn<sub>mix</sub> electrocatalysts towards ethanol oxidation in 0.5 M KOH + 0.5 M EtOH solutions at a scan rate of 50 mVs<sup>-1</sup>. The geometric area of the glassy carbon electrode (0.071 cm<sup>2</sup>) was used in the calculation of the current density.

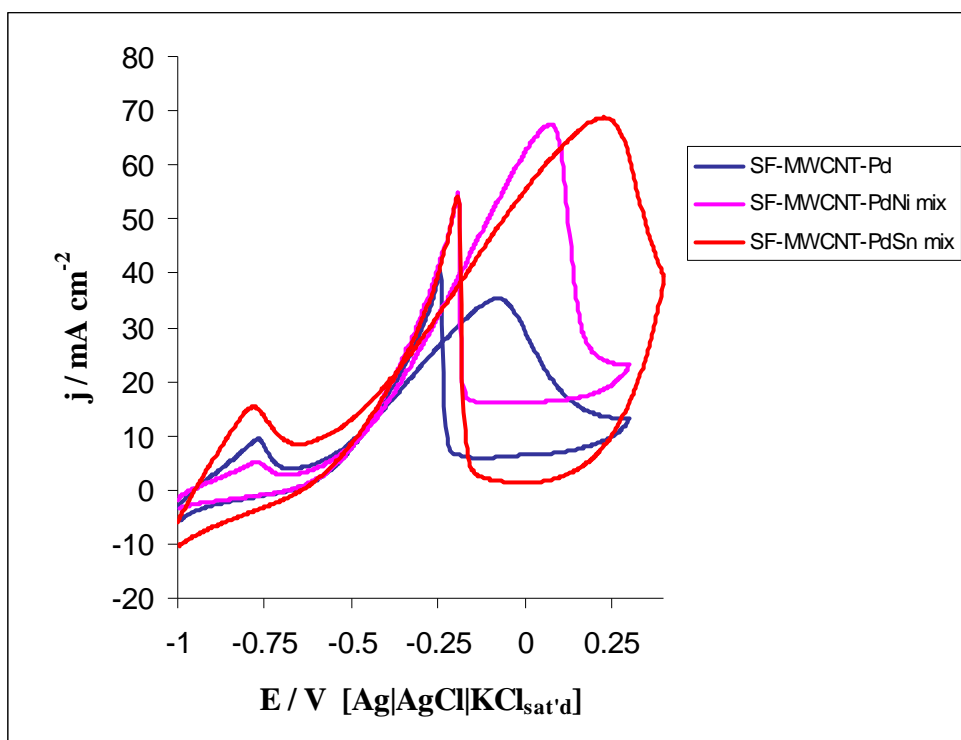


**Figure 4.12:** Cyclic voltammograms of SF-MWCNT-Pd, SF-MWCNT-PdNi<sub>mix</sub> and SF-MWCNT-PdSn<sub>mix</sub> (at the fourth cycle) 0.5 M KOH + 0.5 M EtOH solutions. Scan rate: 50 mVs<sup>-1</sup>.

## Chapter 4: Results and discussion

---

The electro-oxidation of ethanol was clearly observed from figure 4.12, which is characterized by two well defined peaks on the forward and reverse scans. The magnitude of the peak current in the forward scan shows the electrocatalytic activity of the electrocatalyst towards the ethanol electro-oxidation reaction. The forward oxidation peak is associated with the electro-oxidation of freshly chemisorbed species from the ethanol adsorption and the reverse oxidation peak is associated with the removal of carbonaceous species which were not completely oxidized in the forward scan [63,177,178]. The ratio of the forward anodic peak current density ( $I_f$ ) to the reverse anodic peak current density ( $I_b$ ) i.e ( $I_f/I_b$ ) can be used to describe the electrocatalyst tolerance to carbonaceous species build up on the electrocatalysts' surface since the carbonaceous species are typically in the form of linearly bonded Pd=C=O [63,66,179,180]. A low  $I_f/I_b$  value shows large amount of the carbonaceous species build up on the electrocatalysts' surface due to poor ethanol electro-oxidation during the forward scan and a high  $I_f/I_b$  ratio shows the converse case.

The electrode with Pd alone (SF-MWCNT-Pd) gave poorer  $I_f/I_b$  ratio and current density than the bimetallic catalysts. The SF-MWCNT-PdSn<sub>mix</sub> electrocatalyst showed broader peak compared to the SF-MWCNT-Pd or SF-MWCNT-PdNi<sub>mix</sub>, presumably due to the involvement

## Chapter 4: Results and discussion

---

of more than one oxidation state of Sn, and/or the different locations of the Sn nanoparticles at the different environments of the SF-MWCNTs leading to different but very close oxidation potentials of the ethanol.

A change in Gibb's free energy of reaction ( $\Delta G$ ) is related to the electrochemical potential (E) by the relationship:

$$\Delta G = -nFE \quad (4.10)$$

where  $\Delta G$  = change in Gibb's free energy; n = the number of electron transferred; F = Faraday's constant; and E = potential.

As a result, the onset potential for ethanol electro-oxidation is directly related to the activation energy of the reaction [34]. From the electrocatalytic performance (in terms of onset potential, current density, and the  $I_f/I_b$  ratio) summarized in Table 4.3, the SF-MWCNT-PdSn<sub>mix</sub> is the most favoured catalyst system. The SF-MWCNT-PdSn<sub>mix</sub> system gave the highest peak potential ( $E_p \approx 0.25$  V), meaning poor kinetics for ethanol oxidation compared to the SF-MWCNT-PdSn<sub>i</sub> and SF-MWCNT-Pd.

## Chapter 4: Results and discussion

---

However, of major interest is the observation that the current peak density on both SF-MWCNT-PdSn<sub>mix</sub> and SF-MWCNT-PdNi<sub>mix</sub> systems is much higher than that observed at the SF-MWCNT-Pd, meaning that the Pd-M<sub>mix</sub> systems are more stable and more likely to resist poisoning by the reaction products (confirmed later by chronoamperometric test). The advantageous effect of the Ni and Sn metals on the Pd systems may be associated with the oxophilicity of the Ni and Sn to generate the Sn-OH or Ni-OH moieties. Increased amount of OH<sub>ads</sub> on the catalyst surface is believed to favour the formation of the acetate (CH<sub>3</sub>COO<sup>-</sup>) by coupling with CH<sub>3</sub>CO<sub>ads</sub>, thus explaining the stability of Sn even at high ethanol concentration. Other researchers have observed the advantageous effect of the Ni on the Pd catalyst [44,181,182] but it is only Petrii *et al.* [181] that recently speculated this to be due to the hydrophilicity of the Ni and NiO.

## Chapter 4: Results and discussion

---

**Table 4.3:** Comparison of the electrochemical performances of ethanol oxidation on SF-MWCNT-Pd, SF-MWCNT-PdSn<sub>mix</sub> and SF-MWCNT-PdNi<sub>mix</sub> electrodes measured in 0.5 M ethanol + 0.5 M KOH solutions at a sweep rate of 50 mVs<sup>-1</sup> (n = 9).

Electrocatalysts	Electrocatalytic performance data			
	$J_f / \text{mA cm}^{-2}$	$E_{\text{onset}} / \text{V}$	$E_p / \text{V}$	$I_f/I_b$
SF-MWCNT-Pd	35.2±0.02	-0.65±0.02	-0.07±0.02	0.90
SF-MWCNT-PdNi <sub>mix</sub>	67.2±0.02	-0.68±0.02	0.08±0.02	1.24
SF-MWCNT-PdSn <sub>mix</sub>	68.7±0.02	-0.63±0.02	0.24±0.02	1.27

### 4.3.2 Long-term stability curves of the electrocatalysts

Chronoamperometric studies were conducted to investigate the electrocatalysts' stability. Figure 4.13 shows the long-term chronoamperometric curves of the three electrocatalyst electrodes in 0.5 M C<sub>2</sub>H<sub>5</sub>OH + 0.5 M KOH solutions at a fixed potential of -0.2 V.

## Chapter 4: Results and discussion

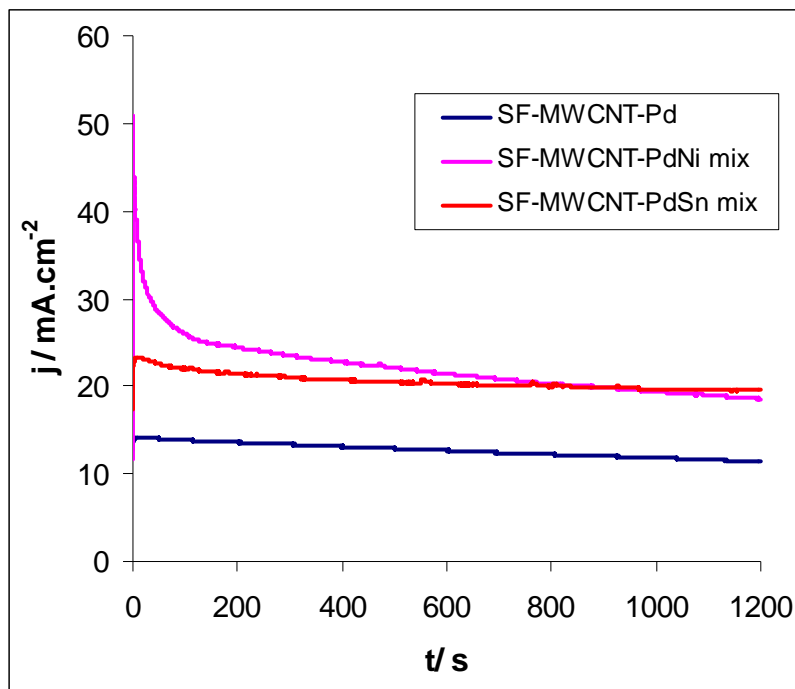


**Figure 4.13:** Chronoamperometric curves of SF-MWCNT-Pd, SF-MWCNT-PdSn<sub>mix</sub> and GCE-SF-MWCNT-PdNi<sub>mix</sub> electrodes in 0.5 M C<sub>2</sub>H<sub>5</sub>OH + 0.5 M KOH aqueous solutions at fixed potential of -0.2 V.

SF-MWCNT-PdNi<sub>mix</sub> and SF-MWCNT-PdSn<sub>mix</sub> electrocatalysts showed better stability and higher current response than SF-MWCNT-Pd electrocatalyst for ethanol oxidation in alkaline medium. The SF-MWCNT-PdNi<sub>mix</sub> electrocatalyst initially showed a higher current which then decreases with time and stabilizes just below that of the SF-MWCNT-PdSn<sub>mix</sub> electrocatalyst, which was stable throughout the experiment. These results show that the addition of Sn or Ni on the SF-MWCNT-Pd enhances the stability of the electrocatalyst.

## Chapter 4: Results and discussion

### 4.3.3 Chronopotentiometric analysis on the electrocatalysts

The electrocatalysts were further evaluated for their ability to resist poisoning due to carbonaceous species using chronopotentiometric studies. Figure 4.14 (a) shows the chronopotentiometric curves of ethanol oxidation on SF-MWCNT-Pd, SF-MWCNT-PdNi<sub>mix</sub> and SF-MWCNT-PdSn<sub>mix</sub> electrocatalysts at (a) 1 mA cm<sup>-2</sup> and (b) 3 mA cm<sup>-2</sup>.

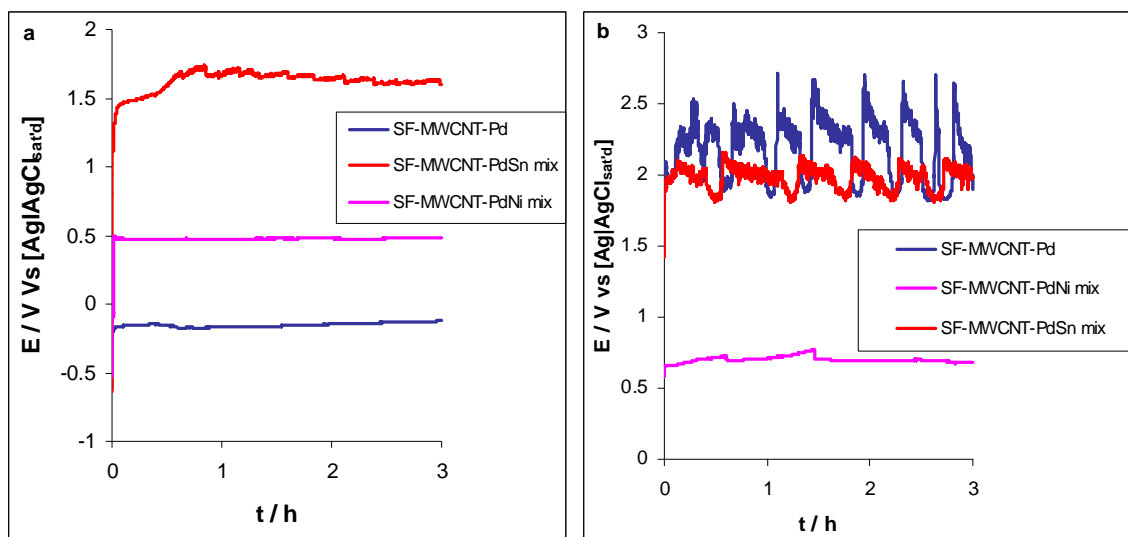


**Figure 4.14:** Chronopotentiometric curves of GCE-SF-MWCNT-Pd, GCE-SF-MWCNT-PdSn<sub>mix</sub> and GCE-SF-MWCNT-PdNi<sub>mix</sub> in 0.5 M C<sub>2</sub>H<sub>5</sub>OH + 0.5 M KOH aqueous solutions at (a) 1 mA cm<sup>-2</sup> and (b) 3 mA cm<sup>-2</sup>.

At 1 mA cm<sup>-2</sup>, figure 4.14 (a); a steady state oxidation of ethanol was observed on the SF-MWCNT-Pd and SF-MWCNT-PdNi<sub>mix</sub> electrocatalysts at low potentials (-0.13 and 0.5 V respectively), with minor potential oscillations. However, the ethanol oxidation on SF-

## Chapter 4: Results and discussion

---

MWCNT-PdSn<sub>mix</sub> occurred at higher potentials (1.4 - 1.7 V) with potential oscillations. At 3 mA cm<sup>-2</sup>, figure 4.14 (b); the ethanol oxidation on the SF-MWCNT-PdNi<sub>mix</sub> occurred at low potential (~ 0.6 V) with minor potential oscillation while the oxidation at the SF-MWCNT-Pd and SF-MWCNT-PdSn<sub>mix</sub> occurred at higher potential (2.0 - 2.5 V) with significant potential oscillations. Higher potential polarizations accompanied by oscillations are indicative of poor catalysis and / or a poisoned electrocatalyst [36]. Thus, this result suggests that the tendency for the electrocatalytic sites to be blocked by the adsorbed species during ethanol oxidation decreases as SF-MWCNT-Pd >> SF-MWCNT-PdNi<sub>mix</sub> > SF-MWCNT-PdSn<sub>mix</sub> at 1 mAcm<sup>-2</sup> and decreases as SF-MWCNT-PdNi<sub>mix</sub> >> SF-MWCNT-PdSn<sub>mix</sub> > SF-MWCNT-Pd at 3 mA cm<sup>-2</sup>. The stability of the SF-MWCNT-PdNi<sub>mix</sub> and SF-MWCNT-PdSn<sub>mix</sub> electrocatalysts towards poisoning was further demonstrated using CO stripping voltammetry as discussed below. The two were chosen as they showed better electrocatalytic activity than the SF-MWCNT-Pd electrocatalyst.

### **4.3.4 The effect of carbon monoxide poisoning during ethanol oxidation**

Adsorption of carbon monoxide or CO-like species on the surface of the electrocatalyst is used to evaluate the extent to which an electrocatalyst can tolerate poisoning in a fuel cell system [166,180].

## Chapter 4: Results and discussion

Figure 4.15 compares the effect of CO on the direct oxidation of ethanol in alkaline medium at the SF-MWCNT-PdNi<sub>mix</sub> and SF-MWCNT-PdSn<sub>mix</sub> electrodes. At the SF-MWCNT-PdNi<sub>mix</sub> electrode, the onset potential for ethanol oxidation in the presence of saturated CO is more positive (−0.27 V) than in the absence of saturated CO (−0.46 V).

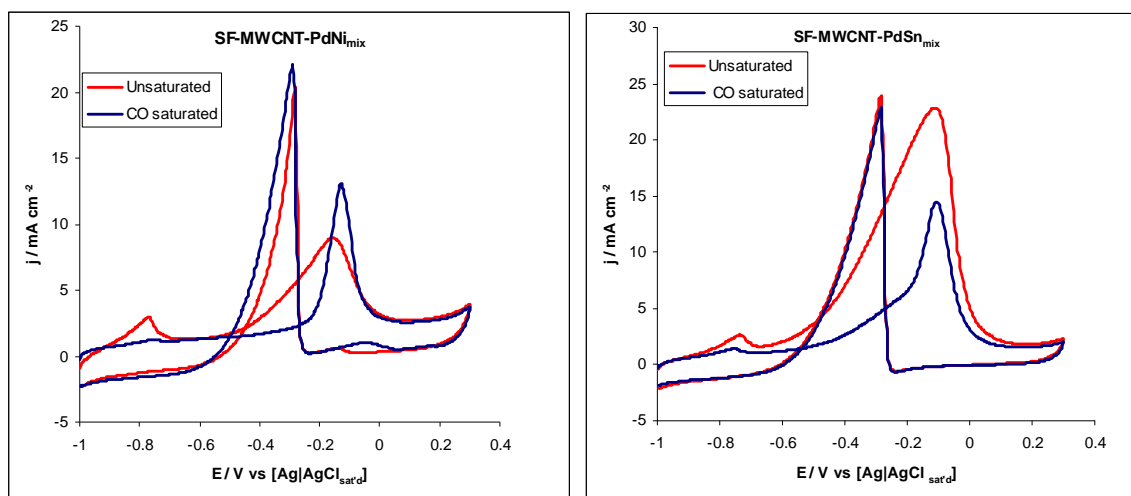


**Figure 4.15:** Comparison of the influence of CO on SF-MWCNT-PdNi<sub>mix</sub> and S-MWCNT-PdSn<sub>mix</sub> electrodes in 0.5 M ethanol + 0.5 M KOH solution with or without the presence of saturated CO.

Similarly, at the SF-MWCNT-PdSn<sub>mix</sub> electrode, the onset potential in the presence of saturated CO (−0.46 V) is more positive than in the absence of it (−0.66 V). In both cases, the magnitude of potential shift is essentially the same (i.e., 200 mV), suggesting the same level of tolerance of CO. However, unlike the SF-MWCNT-PdNi<sub>mix</sub> electrode where the forward oxidation peak increased slightly, presumably due to the combined oxidation of ethanol and CO; the SF-MWCNT-PdSn<sub>mix</sub>

## Chapter 4: Results and discussion

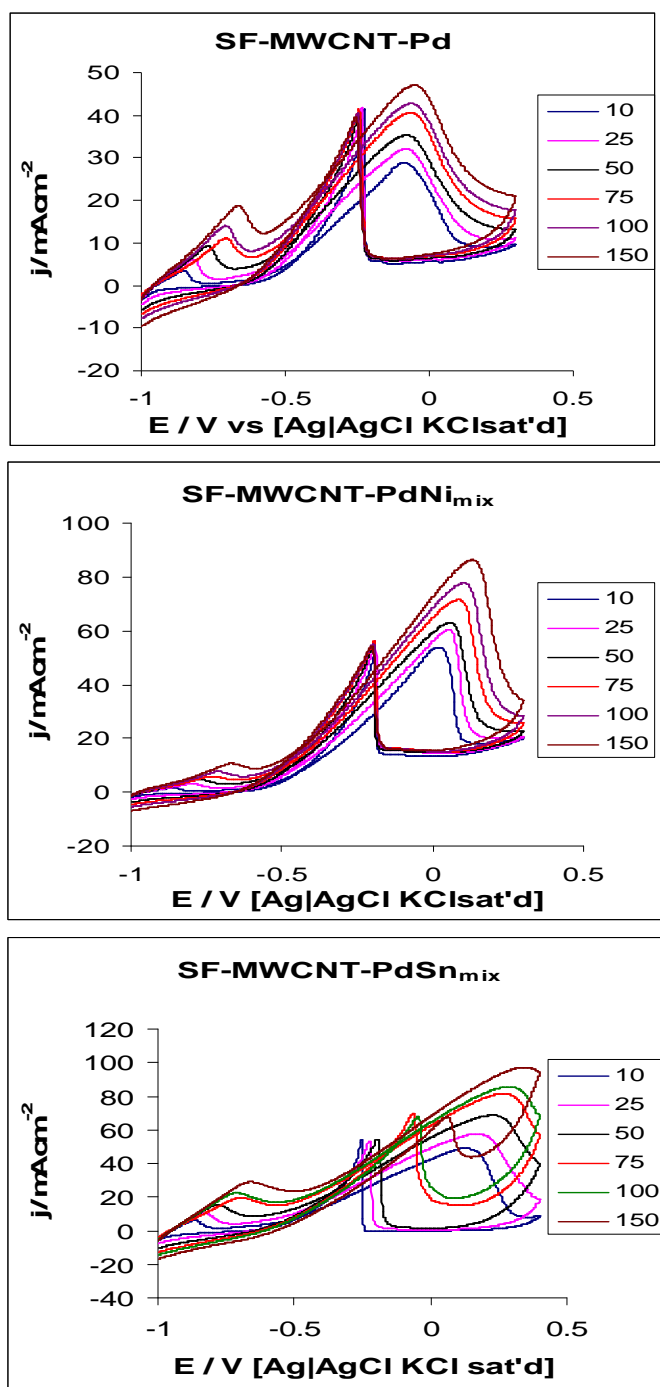
---

showed a different behaviour. In the absence of CO, the onset potentials were observed to be -0.655 V for SF-MWCNT-PdSn<sub>mix</sub> with  $I_p$  of 21.77 mA cm<sup>-2</sup> and -0.459 V for SF-MWCNT-PdNi<sub>mix</sub> with a peak current of 8.807 mA/cm<sup>-2</sup>. In the presence of CO the onset potentials shifted to more positive values, -0.463 V for SF-MWCNT-PdSn<sub>mix</sub> with a peak current of 14.169 mA cm<sup>-2</sup> and -0.267 V and 13.286 mA cm<sup>-2</sup> for the SF-MWCNT-PdNi<sub>mix</sub> electrode. The results indicated that the removal of CO on SF-MWCNT-PdNi<sub>mix</sub> electrocatalyst is more difficult than that of SF-MWCNT-PdSn<sub>mix</sub> electrocatalyst. However, the peak potential for the ethanol oxidation in the presence of CO is more negative on the SF-MWCNT-PdNi<sub>mix</sub> (-0.124 V) as compared to that of SF-MWCNT-PdSn<sub>mix</sub> electrocatalysts (-0.096 V).

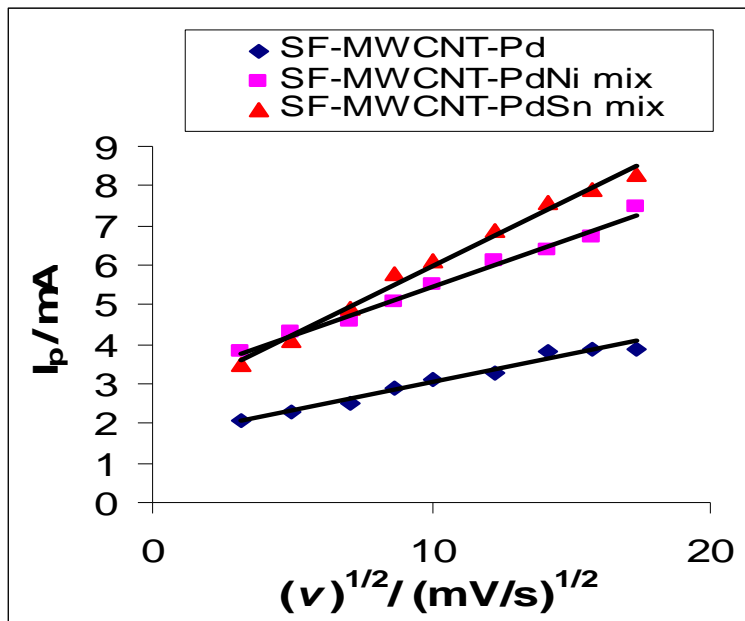
### 4.3.5 The effect of the sweep rate ( $\nu$ ) on the current density ( $I_p$ )

Figure 4.16 shows the cyclic voltammograms of ethanol oxidation in 0.5 M KOH + 0.5 M EtOH solutions on SF-MWCNT-Pd, SF-MWCNT-PdNi<sub>mix</sub> and SF-MWCNT-PdSn<sub>mix</sub> electrodes at different sweep rates (10 – 150 mV s<sup>-1</sup>). It can be observed that the anodic peak occurs at higher peak potentials as the sweep rate is increased. The peak current density increased with increasing sweep rate. The relationship between  $I_p$  and  $\nu^{1/2}$  are given in figure 4.17, where straight lines are observed.

## Chapter 4: Results and discussion



**Figure 4.16:** CVs of (a) SF-MWCNT-Pd, (b) SF-MWCNT-PdNi<sub>mix</sub> and (c) SF-MWCNT-PdSn<sub>mix</sub> in 0.5 M KOH + 0.5 M C<sub>2</sub>H<sub>5</sub>OH at different scan rates (10 – 150 mVs<sup>-1</sup>).



**Figure 4.17:** Dependence of the peak current density ( $I_p$ ) obtained from the forward CV scan on the scan rate of CV ( $v^{1/2}$ ) in 0.5 M KOH + 0.5 M  $C_2H_5OH$  aqueous solutions on SF-MWCNTS-Pd, SF-MWCNT-PdNi<sub>mix</sub> and SF-MWCNT-PdSn<sub>mix</sub> electrocatalysts.

#### 4.3.6 Tafel analysis

Figure 4.18 (a) compares the linear sweep voltammograms at a sweep rate of  $1 \text{ mVs}^{-1}$  at the three electrodes in 0.5 M  $C_2H_5OH$  + 0.5 M KOH aqueous solutions. The relationship between the oxidation current and potential is given by the Tafel equation 4.11 [181,183].

$$\eta = a + b \log j \quad (4.11)$$

## Chapter 4: Results and discussion

---

$$b = \frac{2.303 RT}{\alpha nF} \quad (4.12)$$

where  $\eta$  = overpotential (difference between the applied potential and the open circuit potential);  $j$  = current density;  $b$  = Tafel slope;  $\alpha$  = transfer coefficient;  $n$  = number of electrons involved in the rate determining step, while other symbols retain their usual meaning.

Figure 4.18 (b) shows the plots of  $\eta$  vs.  $\log j$  (from the quasi-steady state curves in Fig. 27 a), giving Tafel slopes of 180 mV dec<sup>-1</sup> (SF-MWCNT-PdNi<sub>mix</sub>), 211 mV dec<sup>-1</sup> (SF-MWCNT-PdSn<sub>mix</sub>) and 209 mV dec<sup>-1</sup> (SF-MWCNT-Pd). The value of  $\alpha n \approx 0.3$  for all the electrodes, the  $n = 3$  for ethanol oxidation [37,173]. Thus, a  $\alpha \approx 0.1$  indicates that the ethanol electro-oxidation reaction is an irreversible process [37]. The Tafel data also suggest that similar reaction mechanism is probably operating at all the electrodes. Tafel slopes higher than 118 mV dec<sup>-1</sup> as obtained here are characteristic of porous electrode with high internal surface area leading to high electrocatalytic activities [183]. Porous electrodes have very narrow charge transfer control regions the mass transport interferences are not negligible.

## Chapter 4: Results and discussion

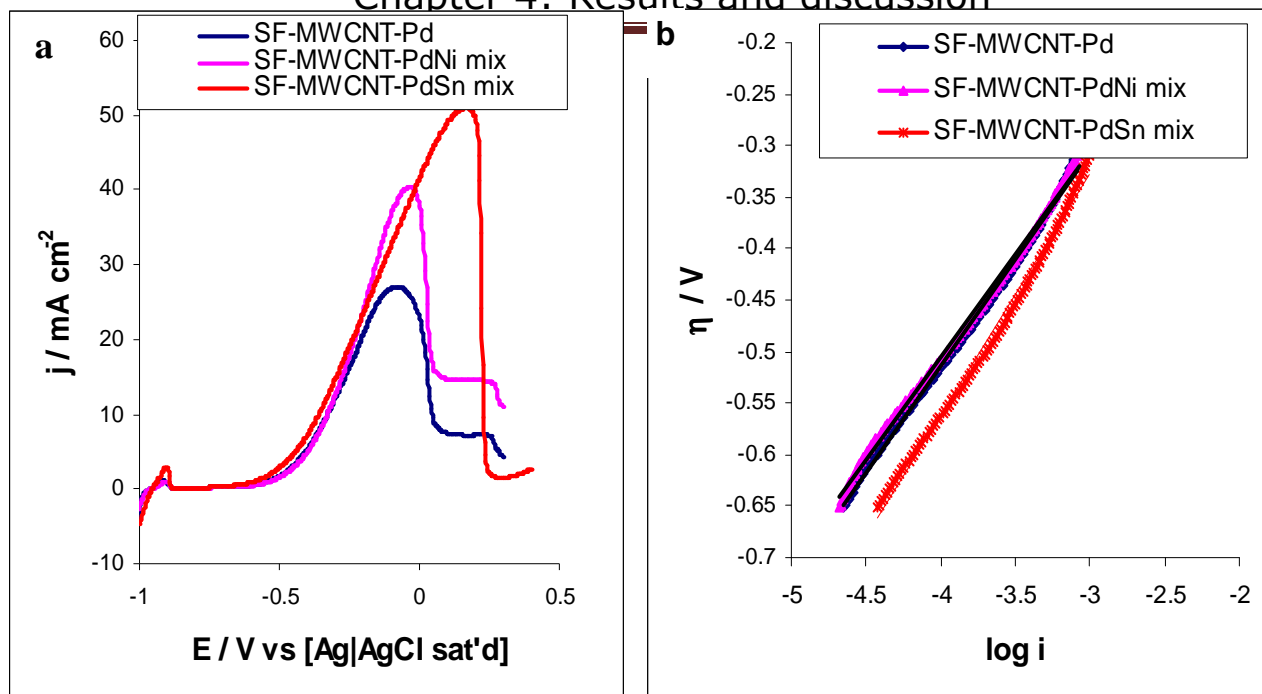


**Figure 4.18:** (a) A quasi-steady-state curve of the ethanol oxidation on the SF-MWCNT-Pd, SF-MWCNT-PdNi<sub>mix</sub> and SF-MWCNT-PdSn<sub>mix</sub> electrocatalysts in 0.5 M C<sub>2</sub>H<sub>5</sub>OH + 0.5 M KOH aqueous solutions. (b) The Tafel plot of the ethanol oxidation on the SF-MWCNT-Pd, SF-MWCNT-PdNi<sub>mix</sub> and SF-MWCNT-PdSn<sub>mix</sub> electrocatalysts in 0.5 M C<sub>2</sub>H<sub>5</sub>OH + 0.5 M KOH aqueous solutions.

## Chapter 4: Results and discussion

---

### 4.3.7 Electrochemical impedance analysis

EIS is a sensitive electrochemical technique that is used for the investigation of the heterogeneous electron transfer kinetics [184-187] as well as the electrocatalytic oxidation kinetics of alcohols in fuel cell systems [176,179,180]. Figures 4.19 presents typical Nyquist plots and the corresponding Bode plots (Figure 4.20) obtained at the SF-MWCNT-Pd, SF-MWCNT-PdNi<sub>mix</sub> and SF-MWCNT-PdSn<sub>mix</sub> electrodes in 0.5 M C<sub>2</sub>H<sub>5</sub>OH + 0.5 M KOH at three different potentials (-0.6V, 0.2 V and 0.3 V). The spectra were satisfactorily fitted with the  $R_s(R_{ct}C_{dl})$  circuit for the SF-MWCNT-Pd, and  $R_s(R_{ct}CPE)$  circuit for the SF-MWCNT-PdNi<sub>mix</sub> and SF-MWCNT-PdSn<sub>mix</sub>, where  $R_s$  is the electrolyte resistance,  $R_{ct}$  is the charge transfer resistance,  $C_{dl}$  is the double layer capacitance, while  $CPE$  is the constant phase element. The impedimetric data are summarised in Table 4.4. The  $R_{ct}$  is related to the reaction kinetics; its values of the SF-MWCNT-Pd and SF-MWCNT-PdNi<sub>mix</sub> electrodes decreased as the potential was increased from negative to positive potentials (-0.6 to 0.3 V), indicating faster electro-transfer kinetics at higher potentials. However, the SF-MWCNT-PdSn<sub>mix</sub> electrode showed a slightly different pattern where the  $R_{ct}$  at the 0.2 V is higher than obtained at the -0.6 and 0.3 V. but as the potential was increased to 0.2 V the  $R_{ct}$  value increased indicating high charge

## Chapter 4: Results and discussion

transfer resistance for the SF-MWCNT-PdSn<sub>mix</sub> electrode towards ethanol oxidation.

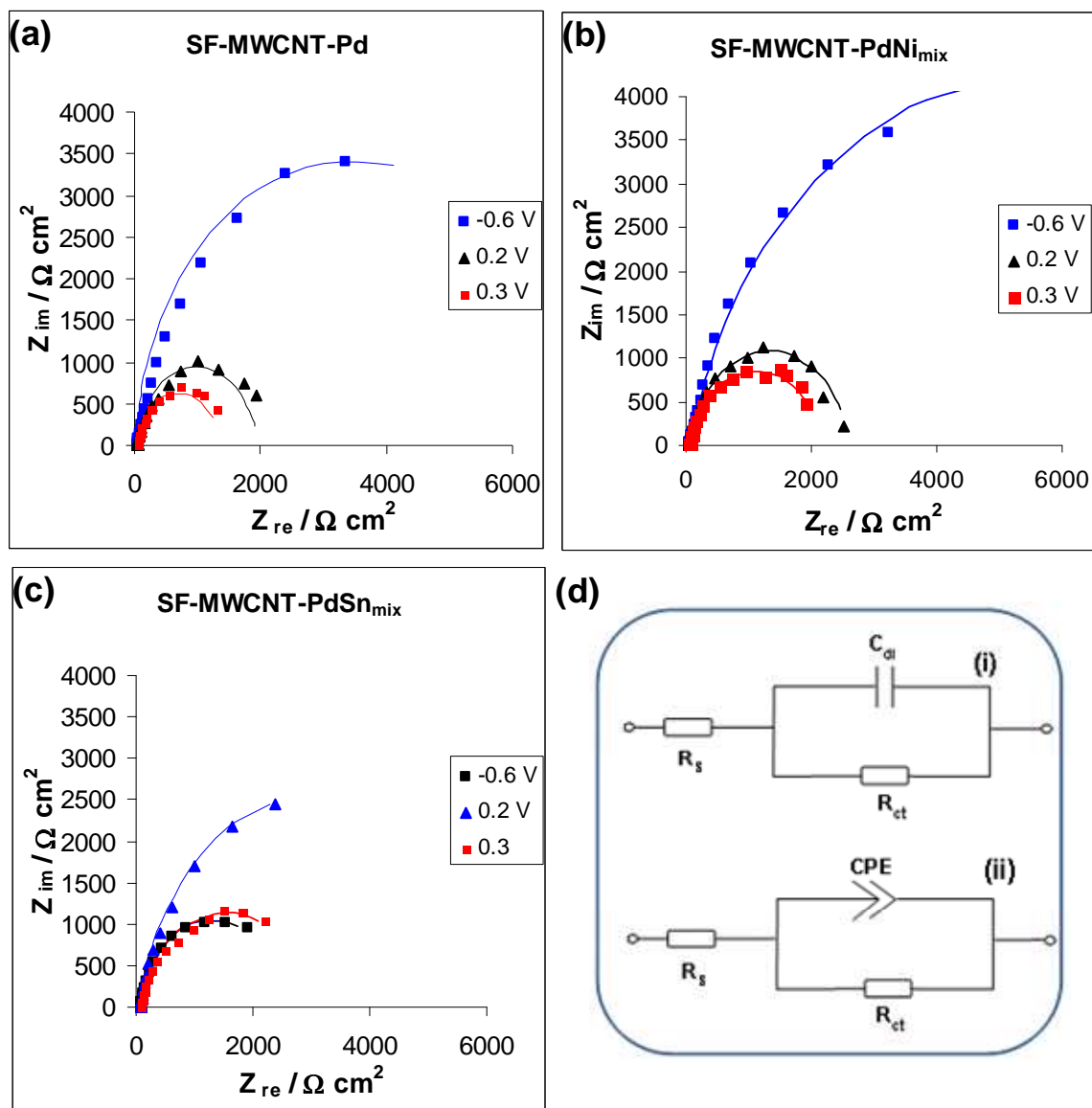


**Figure 4.19:** Nyquist plots obtained during the oxidation of ethanol oxidation at (a) SF-MWCNT-Pd, (b) SF-MWCNT-PdNi<sub>mix</sub>, and SF-MWCNT-PdSn<sub>mix</sub> electrodes and (d) is the equivalent circuit used in fitting the electrochemical impedance spectra.

## Chapter 4: Results and discussion

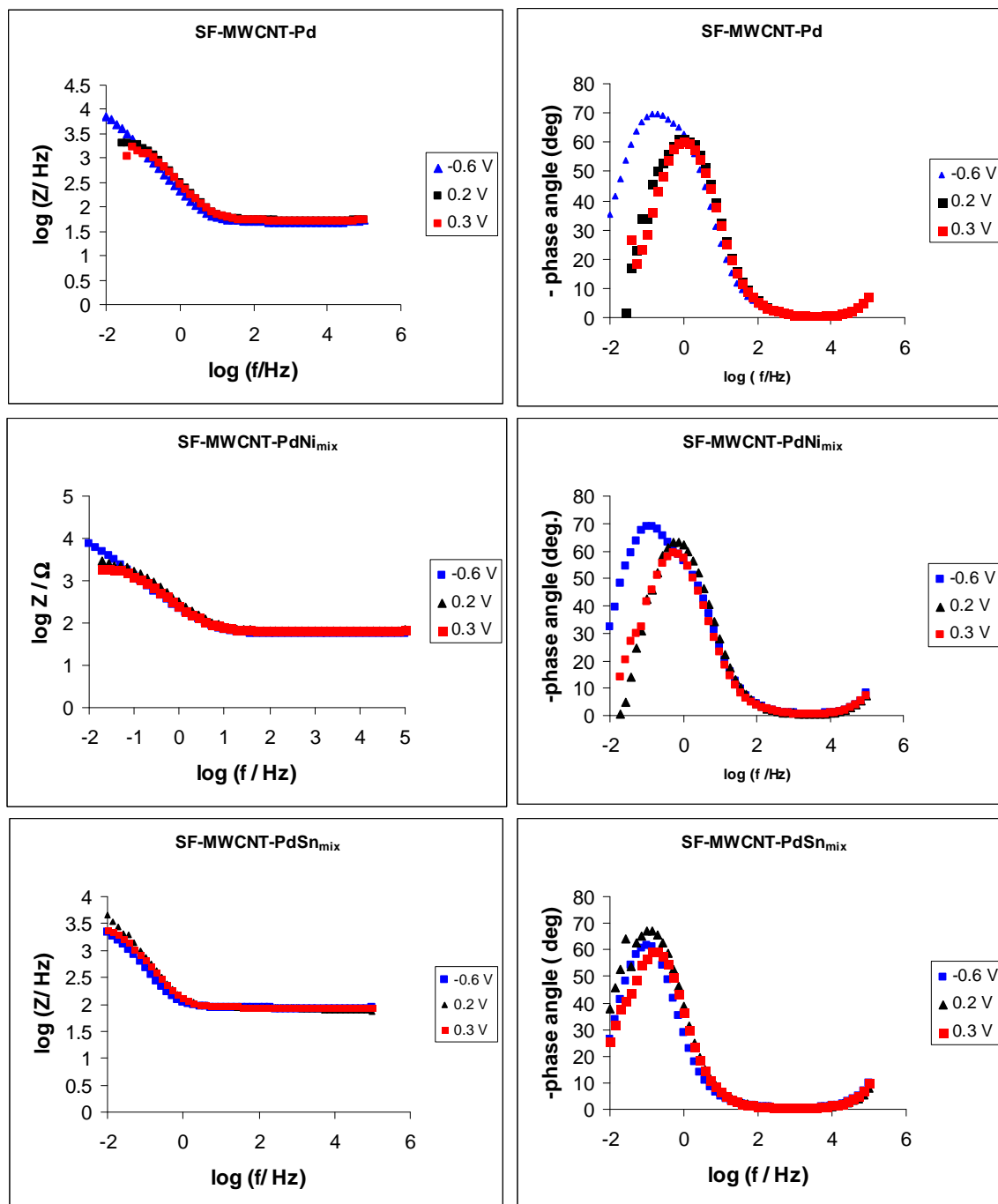


**Figure 4.20:** The Bode plots ( $\log Z$  (a), phase angle (b) vs  $\log f$ ) obtained for the SF-MWCNT-Pd, SF-MWCNT-PdNi<sub>mix</sub>, and SF-MWCNT-PdSn<sub>mix</sub> electrodes in 0.5 M KOH + 0.5 M EtOH solution at different potentials.

## Chapter 4: Results and discussion

---

From the Bode plots (Figure 4.20), it can be observed that at each applied potential of the electrode, there is a maximum phase angle ( $\theta$ ) at a characteristic frequency ( $f$ ). This characteristic frequency increases with increasing potential. In an electrochemical reaction, the frequency is related to the time-constant. Thus, the reaction rate increases with increasing potential, supporting the  $R_{ct}$  data. The Bode plots also shows phase angles lower than  $-90^\circ$  which is expected for an ideal capacitive behaviour, confirming the presence of CPE and the pseudo-capacitive nature of the electrodes. It also means that the  $C_{dl}$  of the SF-MWCNT-Pd is not true double layer capacitance, but also a CPE [184] . The slopes from the plots of  $\log Z$  vs  $\log f$  (Figure 4.20) were in the  $-0.78$  and  $-0.60$  at low frequency regions, smaller than the ideal  $-1.0$  expected for an ideal capacitive behaviour, indicative of pseudo-capacitive behaviour. At the high frequency regions, the slopes are approximately zero, indicative of resistive behaviour.

## Chapter 4: Results and discussion

**Table 4.4:** Impedimetric data for ethanol oxidation on GCE-SF-MWCNT-Pd, GCE-SF-MWCNT-PdSn<sub>mix</sub> and GCE-SF-MWCNT-PdNi<sub>mix</sub> nanocomposites measured in a 0.5 M ethanol + 0.5 M KOH solution at different potentials (n=9).

Bias potential / V (vsAg AgCl sat'd KCl)	Electrochemical impedimetric parameters				
	R <sub>s</sub> / Ω	R <sub>ct</sub> / kΩ	N	CPE / mF	C <sub>dl</sub> / mF
<b>GCE-SF-MWCNT-Pd</b>					
-0.60	51.00 ± 1.40	6.85 ± 0.58	-	-	1.00 ± 0.04
0.20	54.00 ± 1.09	1.87 ± 0.09	-	-	0.52 ± 0.02
0.30	53.20 ± 1.23	1.26 ± 0.07	-	-	0.54 ± 0.02
<b>GCE-SF-MWCNT-PdNi<sub>mix</sub></b>					
-0.60	55.20 ± 0.68	10.86 ± 0.88	0.84 ± 0.07	1.06 ± 0.02	-
0.20	64.60 ± 0.65	2.55 ± 0.07	0.90 ± 0.01	0.64 ± 0.01	-
0.30	64.60 ± 0.47	2.13 ± 0.05	0.86 ± 0.004	0.88 ± 0.01	-
<b>GCE-SF-MWCNT-PdSn<sub>mix</sub></b>					
-0.60	84.70 ± 0.68	2.41 ± 0.10	0.92 ± 0.01	3.34 ± 0.05	-
0.20	83.20 ± 1.11	5.87 ± 0.51	0.91 ± 0.01	2.10 ± 0.05	-
0.30	87.40 ± 0.77	2.62 ± 0.10	1.07 ± 0.01	2.31 ± 0.04	-

### 4.3.8 Effect of varying the concentrations of KOH or ethanol on the voltammetric behaviour

Figure 4.21 shows the linear sweep voltammetric evolutions of different concentrations of ethanol (0.50 – 3.0 M range) in 0.5 M KOH at the SF-MWCNT-PdNi<sub>mix</sub> and SF-MWCNT-PdSn<sub>mix</sub> electrodes at a sweep rate of 1 mV s<sup>-1</sup>. At both electrodes, the current density increased in proportion with the ethanol concentrations until at 1.5 M (for the SF-MWCNT-PdNi<sub>mix</sub>) or 2.0 M (for the SF-MWCNT-PdSn<sub>mix</sub>), where they stabilised and then decreased until 3.0 M: from 0.5 mA cm<sup>-2</sup> at 1.5 M to 0.5 mAcm<sup>-2</sup> at 3.0 M for the SF-MWCNT-PdNi<sub>mix</sub>; and from 1.5 mAcm<sup>-2</sup> at 1.25 M to 1.1 mAcm<sup>-2</sup> at 3.0 M for the SF-MWCNT-PdSn<sub>mix</sub>. The ethanol oxidation peak potential shifted positively with increasing concentration (from -0.167 V at 0.50 M to -0.008 V at 3.0 M for the SF-MWCNT-PdNi<sub>mix</sub>, and from -0.127 V at 0.50 M to 0.001 V at 3.0 M for the SF-MWCNT-PdSn<sub>mix</sub>), indicating poorer electron transport process at the SF-MWCNT-PdSn<sub>mix</sub> than seen at the SF-MWCNT-PdNi<sub>mix</sub> electrode. This phenomenon at high ethanol concentrations has been associated with the mass transfer resistances or build-up of adsorbates formed during the electro-oxidation process or the combination of both [82,166,188].

## Chapter 4: Results and discussion

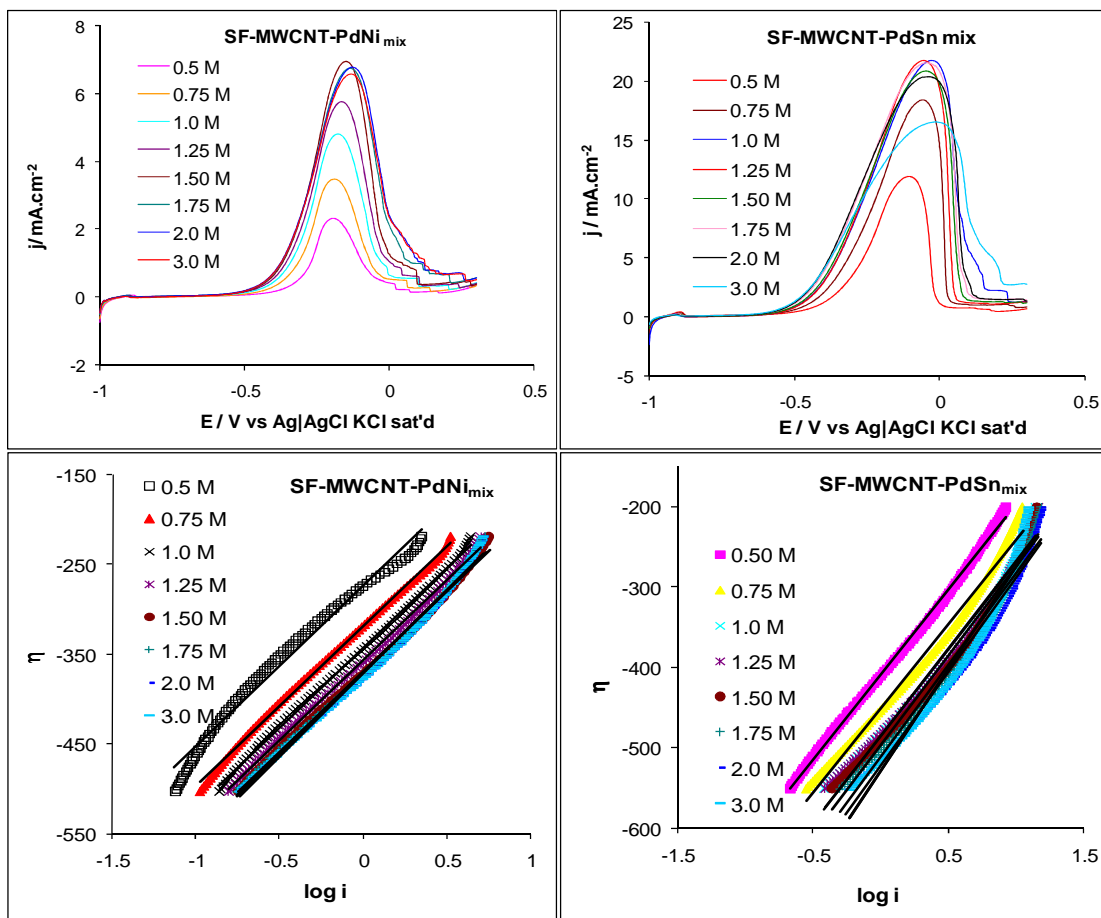


**Figure 4.21:** Linear sweep voltammograms and Tafel plots for ethanol oxidation reaction on the SF-MWCNT-PdNi<sub>mix</sub> and SF-MWCNT-PdSn<sub>mix</sub> electrodes in 0.5 M KOH solution containing ethanol solutions of various concentrations at a sweep rate: 1 mV s<sup>-1</sup>.

At high ethanol concentration, the electrocatalyst becomes easily saturated, presumably, as also proposed by others [166,179] due to the depletion of OH<sub>ads</sub> by CH<sub>3</sub>CO<sub>ads</sub> at the electrode surface. Simply put, at low ethanol concentrations, the reactions are governed by the diffusion of ethanol due to excessive OH<sup>-</sup> ions, whereas at high

## Chapter 4: Results and discussion

concentration the reactions are governed by the diffusion of  $\text{OH}^-$  ions due to excessive ethanol. From the plots of  $\eta$  vs  $\log j$  (exemplified in Figure 4.22), the Tafel slopes (Table 4.5) ranged between 178 and 186  $\text{mV dec}^{-1}$  for the SF-MWCNT-PdNi<sub>mix</sub> and 194 – 255  $\text{mV dec}^{-1}$  for SF-MWCNT-PdSn<sub>mix</sub> at all ethanol concentrations studied.

**Table 4.5:** Tafel slopes of the SF-MWCNT-PdNi<sub>mix</sub> and SF-MWCNT-PdSn<sub>mix</sub> electrocatalysts at 0.5 M KOH and different ethanol concentrations

(EtOH) Concentration Mol. L <sup>-1</sup>	SF-MWCNT-PdNi <sub>mix</sub>		SF-MWCNT-PdSn <sub>mix</sub>	
	Tafel slope (mV dec <sup>-1</sup> )	R <sup>2</sup>	Tafel slope (mV dec <sup>-1</sup> )	R <sup>2</sup>
0.50	180.28	0.9819	211.70	0.9978
0.75	178.18	0.9982	210.83	0.9876
1.0	177.50	0.9987	217.80	0.9789
1.25	178.78	0.9978	215.13	0.9817
1.50	178.81	0.9966	222.90	0.9772
1.75	181.80	0.9944	228.46	0.9731
2.0	183.21	0.9931	234.80	0.9676
3.0	185.91	0.9938	254.75	0.9611

## Chapter 4: Results and discussion

Figure 4.22 shows the dependence of  $\log j$  vs  $\log C_{\text{ETOH}}$  at various low fixed potentials. The reaction orders of ethanol electro-oxidation are shown in Table 4.6. Similarly, the impact of different concentrations of the electrolyte (KOH) at constant concentration of ethanol was investigated at both electrodes. Figure 4.24 exemplifies data obtained at the SF-MWCNT-PdSn<sub>mix</sub> electrode in 0.5 M ethanol solution with different KOH concentrations ranging from 0.50 to 3.0 M. At both electrodes, the peak current increased with increasing KOH concentration until at 1.25 M, where it started to decrease until 3.0 M. The ethanol oxidation peak potential shifted negatively with increasing KOH concentration, indicating that the electrocatalytic oxidation kinetics of ethanol are enhanced by the greater availability of the OH<sup>-</sup> ions in the reaction solution, and hence a higher OH<sup>-</sup> coverage on the electrode surface.

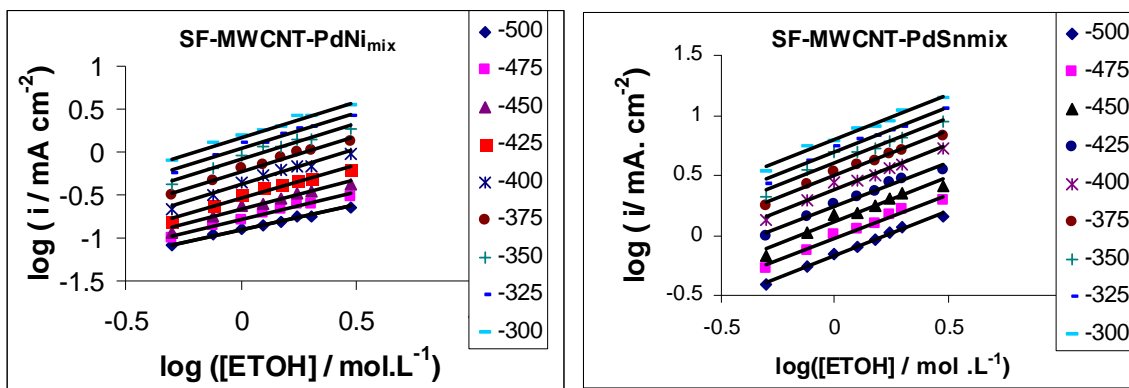


**Figure 4.22:** The log-log plot of current density vs ethanol concentration in 0.5 M KOH obtained at different potentials on SF-MWCNT-PdNi<sub>mix</sub> and SF-MWCNTs-PdSn<sub>mix</sub> electrocatalysts.

## Chapter 4: Results and discussion

---

**Table 4.6:** Reaction orders with respect to OH<sup>-</sup> and ethanol for SF-MWCNT-PdNi<sub>mix</sub> and SF-MWCNT-PdSn<sub>mix</sub> electrocatalysts (RSD ~ 5 %)

<b>Potential (mV) (vs. Ag AgCl)</b>	<b>SF-MWCNT-PdNi<sub>mix</sub></b>		<b>SF-MWCNT-PdSn<sub>mix</sub></b>	
	OH <sup>-</sup>	EtOH	OH <sup>-</sup>	EtOH
-500	0.46	0.57	0.80	0.74
-475	0.52	0.64	0.79	0.74
-450	0.50	0.70	0.76	0.75
-425	0.52	0.78	0.71	0.73
-400	0.49	0.83	0.67	0.75
-375	0.53	0.82	0.60	0.74
-350	0.54	0.84	0.57	0.75
-325	0.53	0.83	0.56	0.75
-300	0.47	0.83	0.55	0.75

## Chapter 4: Results and discussion

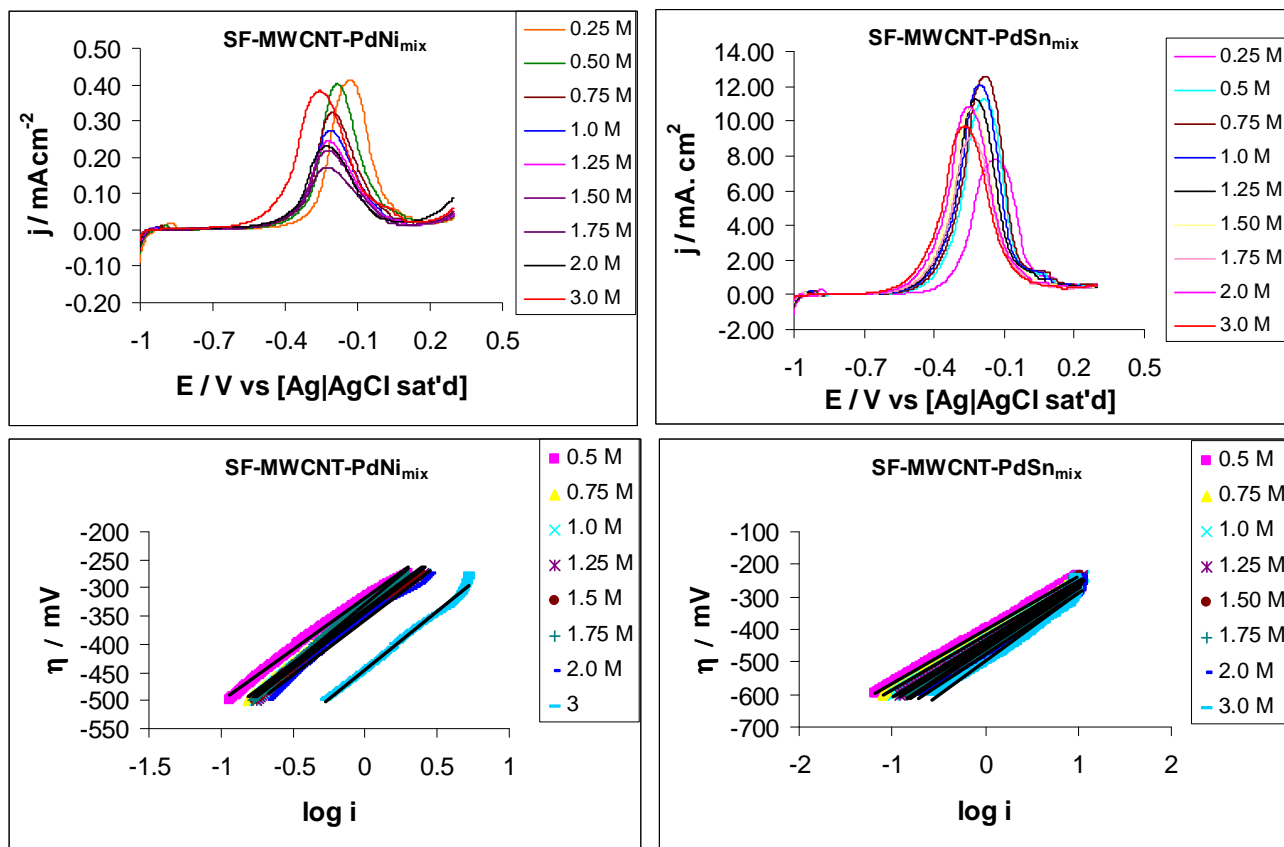


**Figure 4.23:** Linear sweep voltammograms and Tafel plots for ethanol oxidation reaction on the SF-MWCNT-PdNi<sub>mix</sub> and SF-MWCNT-PdSn<sub>mix</sub> in 0.5 M ETOH solution containing KOH solutions of various concentrations at a sweep rate: 1 mV s<sup>-1</sup>.

From the plots of  $\eta$  vs  $\log j$ , the Tafel slopes (Table 4.7) ranged between 178 and 186 mV dec<sup>-1</sup> for the SF-MWCNT-PdNi<sub>mix</sub> and 194 – 255 mV dec<sup>-1</sup> for SF-MWCNT-PdSn<sub>mix</sub> at all KOH concentrations studied. Figure 4.24 shows the dependence of  $\log j$  vs  $\log C_{\text{KOH}}$  at various low fixed potentials. The reaction orders of OH<sup>-</sup> as seen in

## Chapter 4: Results and discussion

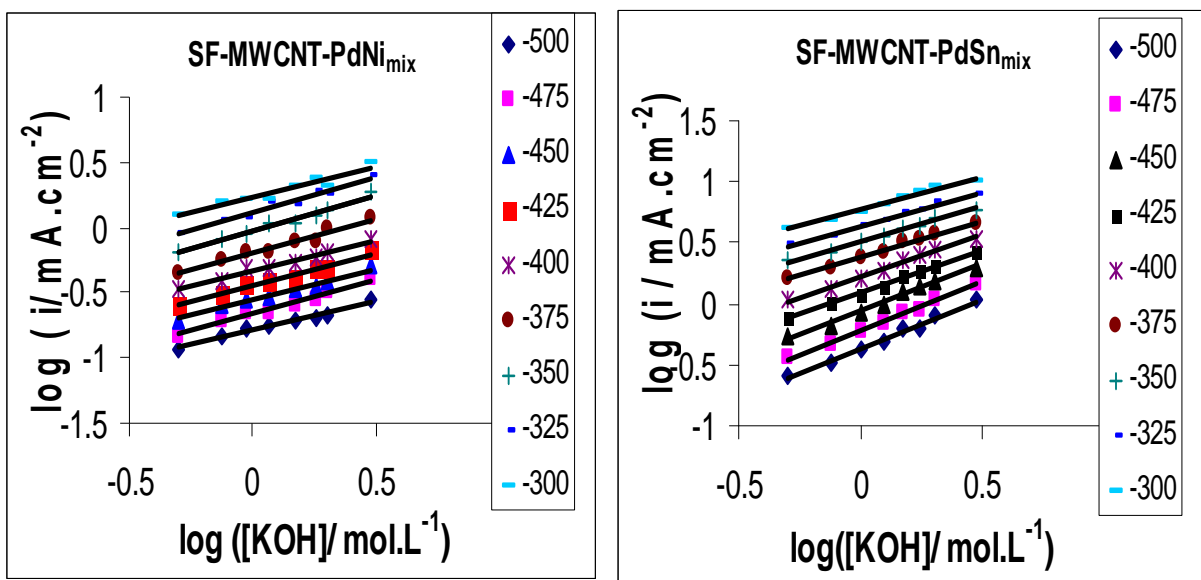
---

Table 4.6 is approximately 0.6 for the SF-MWCNT-PdNi<sub>mix</sub> and 0.8 for the SF-MWCNT-PdSn<sub>mix</sub>

**Table 4.7:** Tafel slopes of the electrocatalysts at constant 0.5 M ETOH concentration and various KOH concentrations

(KOH) Concentration Mol. L <sup>-1</sup>	SF-MWCNT-PdNi <sub>mix</sub>		SF-MWCNT-PdSn <sub>mix</sub>	
	Tafel slope (mV dec <sup>-1</sup> )	R <sup>2</sup>	Tafel slope (mV dec <sup>-1</sup> )	R <sup>2</sup>
0.50	184.72	0.9969	164.24	0.9997
0.75	191.00	0.9970	167.23	0.9986
1.0	195.00	0.9968	174.43	0.9984
1.25	198.44	0.9962	177.89	0.9971
1.50	195.79	0.9952	186.00	0.9934
1.75	209.48	0.9961	189.47	0.9936
2.0	194.54	0.9891	191.83	0.9872
3.0	207.98	0.9929	212.10	0.9719

## Chapter 4: Results and discussion

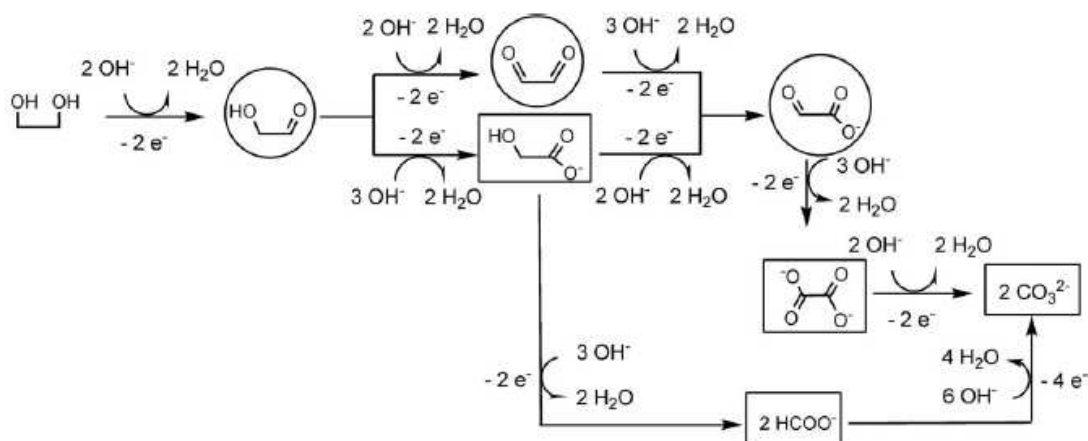


**Figure 4.24:** The log-log plot of current density vs KOH concentration in 0.5 M ETOH obtained at different potentials on SF-MWCNT-PdNi<sub>mix</sub> and SF-MWCNTs-PdSn<sub>mix</sub> catalysts.

## Chapter 4: Results and discussion

### 4.4 Electrocatalysis towards ethylene glycol oxidation in alkaline medium

Next, the prepared electrocatalysts were evaluated for their electrocatalytic behaviour towards EG oxidation in alkaline medium. Studies have shown that the electrochemical oxidation of EG in alkaline media involves at least three carboxylate products (glycolate, glyoxylate and oxalate) plus formate and carbonate since EG contains two hydroxyl groups [2]. The overall mechanism from different literature is shown in scheme 3 [2,100,175,189-193].



**Scheme 3:** Schematic diagram of the overall mechanism of EG oxidation in alkaline media [2,100,175,189-193].

From scheme 3, it can be seen that the electrochemical oxidation of EG in alkaline medium is a complicated reaction as it involves many pathways. Many products can be obtained depending on the type of electrocatalysts used.

### 4.4.1 Comparative electrocatalytic oxidation of ethylene glycol in alkaline medium

Figure 4.26 shows the voltammetric responses of SF-MWCNT-Pd, SF-MWCNT-PdNi<sub>mix</sub> and SF-MWCNT-PdSn<sub>mix</sub> electrocatalysts towards EG oxidation in 0.5 M KOH + 0.5 M EG solutions at a scan rate of 50 mVs<sup>-1</sup>. In the forward scan, the oxidation peak corresponds to the oxidation of freshly chemisorbed species coming from the ethylene glycol adsorption. The reverse scan oxidation peak is associated with the removal of carbonaceous species not completely oxidized during the forward scan.

It can be seen from figure 4.25, that the EG oxidation activity on the SF-MWCNT-PdSn<sub>mix</sub> catalyst is higher than that on the SF-MWCNT-PdNi<sub>mix</sub> and SF-MWCNT-Pd electrocatalysts. The electrochemical parameters are summarized in Table 4.8. The SF-MWCNT-PdSn<sub>mix</sub> has the most negative onset potential, the highest current density and less positive peak potential as compared to the SF-MWCNT-PdNi<sub>mix</sub> electrocatalyst. The  $I_f/I_b$  ratio was used to determine the electrocatalyst tolerance to carbonaceous species accumulation [194]. The  $I_f/I_b$  value of the SF-MWCNT-PdSn<sub>mix</sub> was the highest, indicating

## Chapter 4: Results and discussion

---

better oxidation of ethylene glycol during the anodic scan and also shows that the electrocatalyst is less likely to be poisoned by carbonaceous species such as CO as compared to the SF-MWCNT-Pd and SF-MWCNT-PdNi<sub>mix</sub> electrocatalysts.

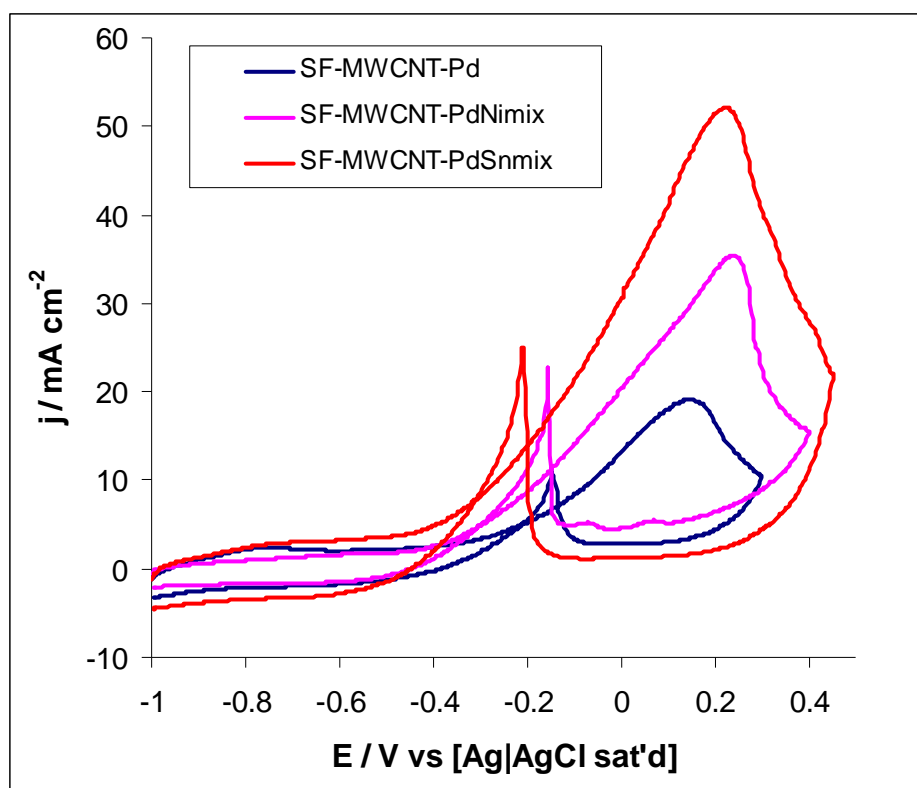


**Figure 4.25:** Cyclic voltammograms of SF-MWCNT-Pd, SF-MWCNT-PdNi<sub>mix</sub> and SF-MWCNT-PdSn<sub>mix</sub> (at the fourth cycle) 0.5 M KOH + 0.5 M EG solutions. Scan rate: 50 mVs<sup>-1</sup>.

## Chapter 4: Results and discussion

---

**Table 4.8:** Comparison of the electrochemical performances of ethanol oxidation on SF-MWCNT-Pd, SF-MWCNT-PdSn<sub>mix</sub> and SF-MWCNT-PdNi<sub>mix</sub> electrodes measured in a 0.5 M Ethylene glycol + 0.5 M KOH solution at a sweep rate of 50 mVs<sup>-1</sup> (n = 9).

Electrocatalyst	Electrocatalytic performance data			
	$J_f / \text{mA cm}^{-2}$	$E_{\text{onset}} / \text{V}$	$E_p / \text{V}$	$I_f/I_b$
SF-MWCNT-Pd	19.1±0.02	-0.24±0.02	0.15±0.02	1.82
SF-MWCNT-PdNi <sub>mix</sub>	35.3±0.02	-0.39±0.02	0.25±0.02	1.57
SF-MWCNT-PdSn <sub>mix</sub>	51.9±0.02	-0.44±0.02	0.23±0.02	2.10

### 4.4.2 Long-term stability curves of the electrocatalysts

The stability of the SF-MWCNT-Pd, SF-MWCNT-PdNi<sub>mix</sub> and SF-MWCNT-PdSn<sub>mix</sub> electrocatalysts were evaluated using chronoamperometric test. Figure 4.26 shows the long-term chronoamperometric curves of the three catalysts in 0.5 M Ethylene Glycol in 0.5 M KOH solutions at a fixed potential of -0.2 V.

## Chapter 4: Results and discussion

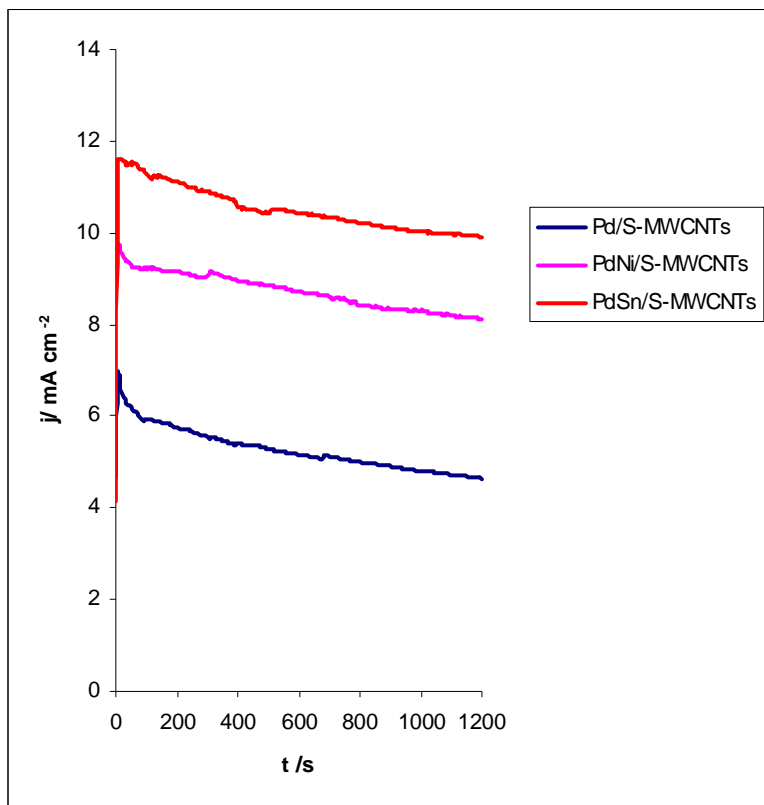


**Figure 4.26:** Chronoamperometric curves of SF-MWCNT-Pd, SF-MWCNT-PdSn<sub>mix</sub> and SF-MWCNT-PdNi<sub>mix</sub> electrodes in 0.5 M EG + 0.5 M KOH aqueous solutions at fixed potential of -0.2 V.

All electrocatalysts showed a small current decay in the first few seconds followed by a small decay. The current value obtained for the SF-MWCNT-PdSn<sub>mix</sub> electrocatalyst was higher (11.59 mA cm<sup>-2</sup>) than that obtained for SF-MWCNT-PdNi<sub>mix</sub> (9.75 mA cm<sup>-2</sup>) and SF-MWCNT-Pd (6.91 mA cm<sup>-2</sup>) electrocatalysts. The current value of the SF-MWCNT-PdSn<sub>mix</sub> electrocatalyst remained higher throughout indicating higher stability of the SF-MWCNT-PdSn<sub>mix</sub> electrocatalyst.

## Chapter 4: Results and discussion

### 4.4.3 Chronopotentiometric analysis on the electrocatalysts

Chronopotentiometry studies were conducted in order to determine the electrocatalysts ability to resist poisoning due to carbonaceous species. Figure 4.27 (a) shows the chronopotentiometric curves of ethylene glycol oxidation on SF-MWCNT-Pd, SF-MWCNT-PdNi<sub>mix</sub> and SF-MWCNT-PdSn<sub>mix</sub> electrocatalysts at (a) 1 mA cm<sup>-2</sup> and (b) 3 mA cm<sup>-2</sup>.

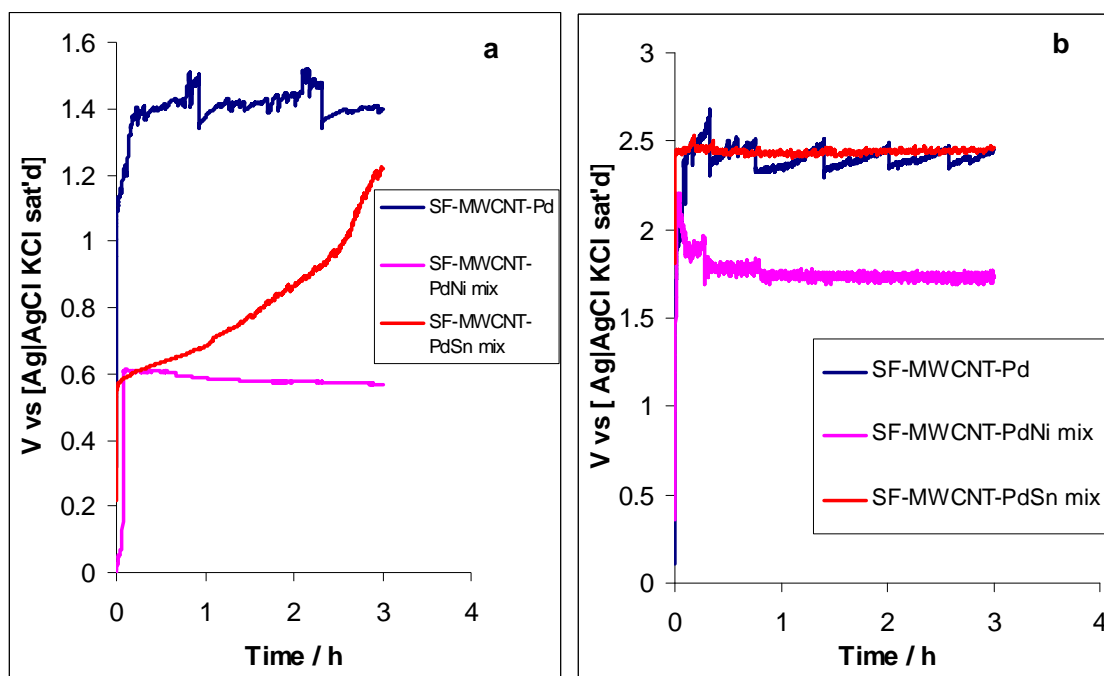


**Figure 4.27:** Chronopotentiometric curves of SF-MWCNT-Pd, SF-MWCNT-PdSn<sub>mix</sub> and SF-MWCNT-PdNi<sub>mix</sub> electrodes in 0.5 M EG + 0.5 M KOH aqueous solutions at (a) 1 mA cm<sup>-2</sup> and (b) 3 mA cm<sup>-2</sup>.

At 1 mA cm<sup>-2</sup> (figure 4.27a), the SF-MWCNT-PdNi<sub>mix</sub> and SF-MWCNT-PdSn<sub>mix</sub> occurred at lower potentials initially (~0.6 V). However, the potential of the SF-MWCNT-PdSn<sub>mix</sub> electrocatalyst increased with time

## Chapter 4: Results and discussion

---

with minor potential oscillations. The SF-MWCNT-PdNi<sub>mix</sub> electrocatalyst remained at lower potential throughout with minor oscillations. The SF-MWCNT-Pd electrocatalyst showed the worst performance, occurring at higher potential ( $\sim 1.4$  V) and with frequent potential oscillations. The results show the SF-MWCNT-Pd electrocatalyst was poisoned and that there were many strongly adsorbed species formed on the surface of the SF-MWCNT-Pd electrocatalyst. At  $3 \text{ mA cm}^{-2}$  (figure 4.27 b), SF-MWCNT-PdNi<sub>mix</sub> electrocatalyst appeared at lower potentials as compared to the SF-MWCNT-PdSn<sub>mix</sub> and SF-MWCNT-Pd electrocatalysts during the ethylene glycol oxidation. The SF-MWCNT-PdNi<sub>mix</sub> and SF-MWCNT-PdSn<sub>mix</sub> electrodes showed the least potential oscillation when compared to the SF-MWCNT-Pd electrode. The huge potential oscillation frequency observed on the SF-MWCNT-Pd electrocatalyst shows a typical phenomenon of a poisoned electrocatalyst. The results indicated that there were no strongly adsorbed species formed on the surface of the SF-MWCNT-PdNi<sub>mix</sub> and SF-MWCNT-PdSn<sub>mix</sub> electrocatalysts. In both current densities, the ethylene glycol oxidation on the SF-MWCNT-PdNi<sub>mix</sub> electrocatalyst occurred at lower potentials indicating more stability.

### 4.4.4 The effect of carbon monoxide poisoning during ethylene glycol oxidation

The catalysts were further evaluated for their stability by studying their tolerance towards CO poisoning. Figure 4.28 compares the effect of CO on the direct oxidation of ethylene glycol in alkaline medium at the SF-MWCNT-PdNi<sub>mix</sub> and SF-MWCNT-PdSn<sub>mix</sub> electrodes. The onset potential for ethylene glycol oxidation on the SF-MWCNT-PdSn<sub>mix</sub> remained the same in the absence and presence of saturated CO (-0.36 V), whereas the onset potential of ethylene glycol oxidation on the SF-MWCNT-PdNi<sub>mix</sub> electrode shifted to more positive values in the presence of saturated CO (from -0.39 V to -0.33 V). The peak potential  $E_p$  of both electrodes slightly shifted to more negative values. The SF-MWCNT-PdSn<sub>mix</sub> shifted from 0.7028 V to 0.6906 V (12.2 mV) while that of the SF-MWCNT-PdNi<sub>mix</sub> shifted from 0.3671 V in the absence of saturated CO to 0.3641 V in the presence of saturated CO (3 mV). These findings show a comparable behaviour of SF-MWCNT-PdSn<sub>mix</sub> and SF-MWCNT-PdNi<sub>mix</sub> electrocatalysts towards CO poisoning.

## Chapter 4: Results and discussion

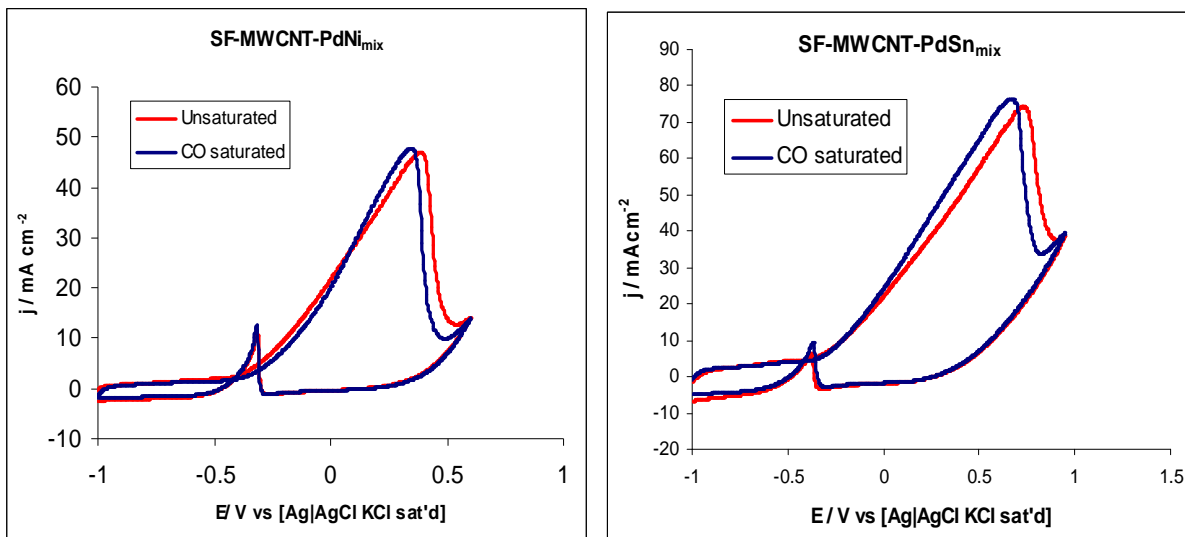


**Figure 4.28:** Comparison of the influence of CO on SF-MWCNT-PdNi<sub>mix</sub> and S-MWCNT-PdSn<sub>mix</sub> electrodes in 0.5 M ethylene glycol + 0.5 M KOH solution with or without the presence of saturated CO.

### 4.4.5 The effect of the sweep rate ( $\nu$ ) on the current density ( $I_p$ )

Figure 4.29 shows the cyclic voltammograms of ethylene glycol oxidation on SF-MWCNT-Pd, SF-MWCNT-PdNi<sub>mix</sub> and SF-MWCNT-PdSn<sub>mix</sub> at different sweep rates (10 – 150 mVs<sup>-1</sup>). It can be observed that the anodic peak occurs at higher peak potentials as the sweep rate is increased. The peak current density increased with increasing sweep rate. The relationship between  $I_p$  and  $\nu^{1/2}$  are given in figure 4.30, where straight lines are observed.

## Chapter 4: Results and discussion

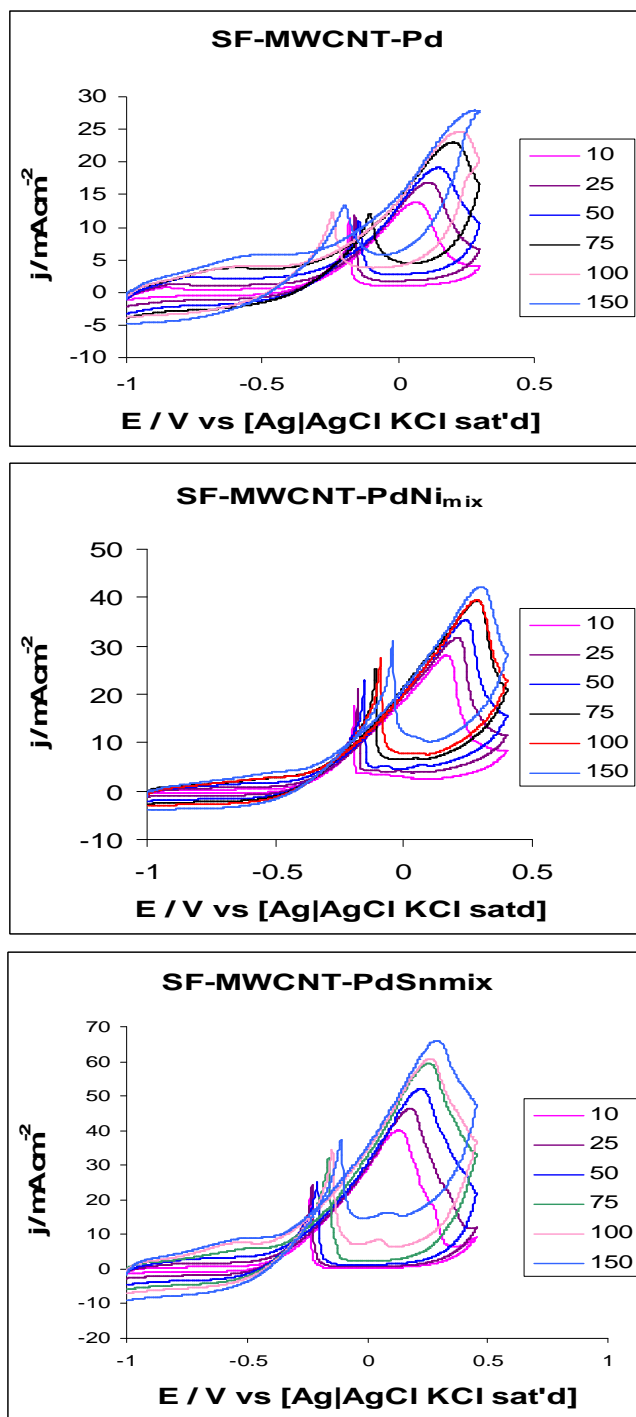


**Figure 4.29:** CVs of (a) SF-MWCNT-Pd, (b) SF-MWCNT-PdNi<sub>mix</sub> and (c) SF-MWCNT-PdSn<sub>mix</sub> in 0.5 M KOH + 0.5 M EG at different scan rates (10 – 150 mV s<sup>-1</sup>).

## Chapter 4: Results and discussion

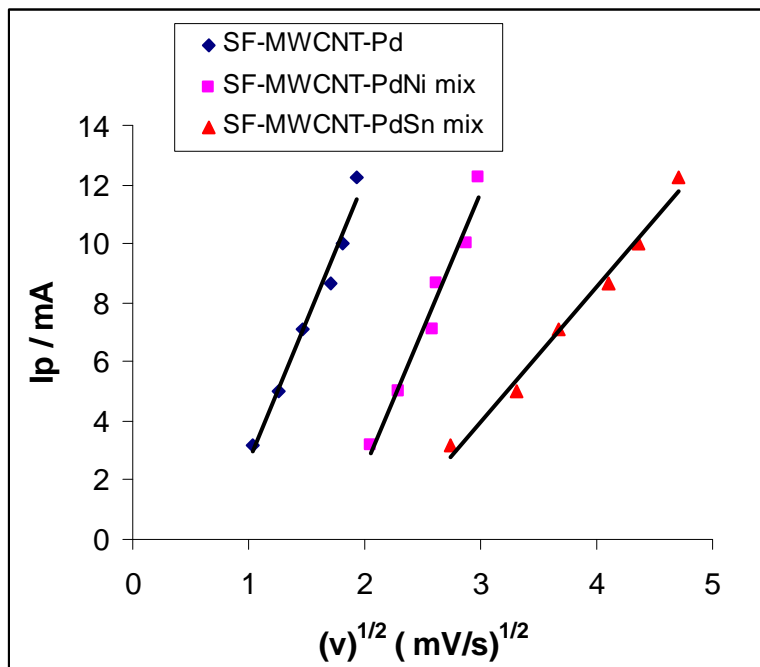


**Figure 4.30:** Dependence of the peak current density ( $I_p$ ) obtained from the forward CV scan on the scan rate of CV ( $v^{1/2}$ ) in 0.5 M KOH + 0.5 M EG aqueous solutions on SF-MWCNTS-Pd, SF-MWCNT-PdNi<sub>mix</sub> and SF-MWCNT-PdSn<sub>mix</sub> electrocatalysts.

### 4.4.6 Tafel analysis

The kinetics parameters of ethylene glycol oxidation reaction were obtained from the Tafel and electrochemical impedance analysis. Figure 4.31 shows the quasi-steady state curves for ethylene glycol oxidation on SF-MWCNT-Pd, SF-MWCNT-PdNi<sub>mix</sub> and SF-MWCNT-PdSn<sub>mix</sub> at 1 mV S<sup>-1</sup>.

## Chapter 4: Results and discussion

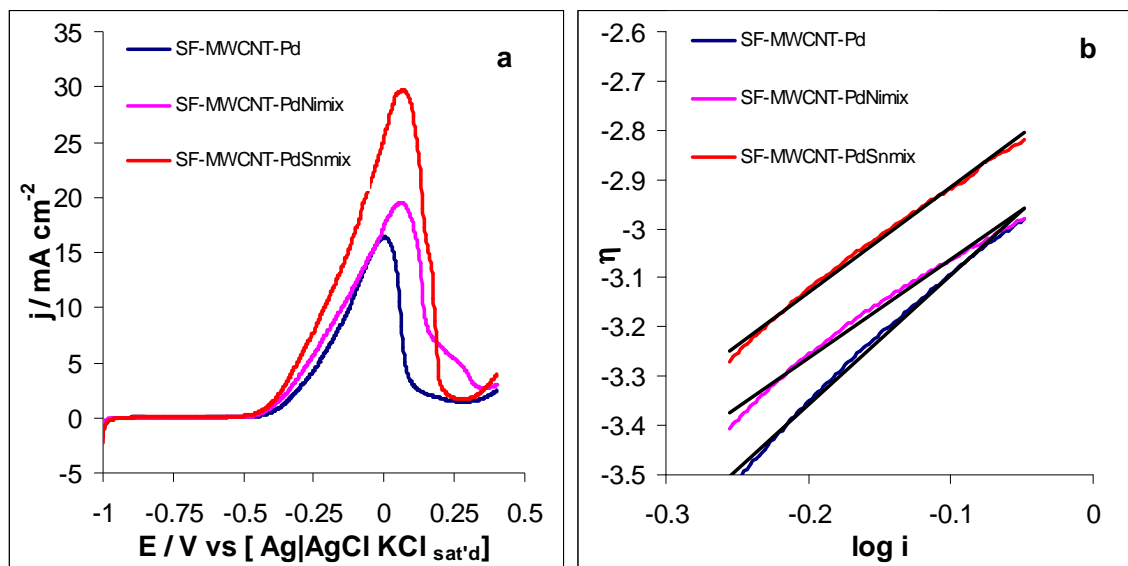


**Figure 4.31:** (a) A quasi-steady-state curve of the ethanol oxidation on the SF-MWCNT-Pd, SF-MWCNT-PdNi<sub>mix</sub> and SF-MWCNT-PdSn<sub>mix</sub> electrocatalysts in 0.5 M Ethylene glycol + 0.5 M KOH aqueous solutions. (b) The Tafel plot of the ethylene glycol oxidation on the SF-MWCNT-Pd, SF-MWCNT-PdNi<sub>mix</sub> and SF-MWCNT-PdSn<sub>mix</sub> electrocatalysts in 0.5 M ethylene glycol + 0.5 M KOH aqueous solutions.

From figure 4.31(a), it is clearly observed that the SF-MWCNT-PdSn<sub>mix</sub> electrocatalyst shows the highest anodic current density when compared to the SF-MWCNT-PdNi<sub>mix</sub> and SF-MWCNT-Pd electrocatalysts. A linear region of the electrodes potential describes the Tafel plots (Figure 4.31(b)) corresponding to the quasi-steady state curves obtained at a slow sweep rate of at 1 mV S<sup>-1</sup>.

## Chapter 4: Results and discussion

---

The transfer coefficient values were obtained assuming one electron transfer to be the rate limiting step. The SF-MWCNT-PdNi<sub>mix</sub> and SF-MWCNT-PdSn<sub>mix</sub> electrodes have Tafel slopes of 200 and 213 mV dec<sup>-1</sup> respectively with a transfer coefficient value of 0.3. This showed that the two electrodes have a similar reaction mechanism of ethylene glycol oxidation in alkaline medium. However, the SF-MWCNT-Pd electrode showed a very high Tafel slope of 254 mV dec<sup>-1</sup> and a transfer coefficient value of  $\alpha = 0.2$  suggesting a different reaction mechanism and slow electron transfer kinetics towards ethylene glycol oxidation in alkaline medium. The high values of the Tafel slopes obtained indicate porous electrodes with high surface areas and high electrocatalytic activities [47].

### 4.4.7 Electrochemical impedance analysis

Figures 4.32 presents typical Nyquist plots and the corresponding Bode plots (Figure 4.34) obtained at the SF-MWCNT-PdNi<sub>mix</sub> and SF-MWCNT-PdSn<sub>mix</sub> in 0.5 M ethylene glycol + 0.5 M KOH at three different potentials (0.2 V, 0.3 V and 0.4 V).

## Chapter 4: Results and discussion

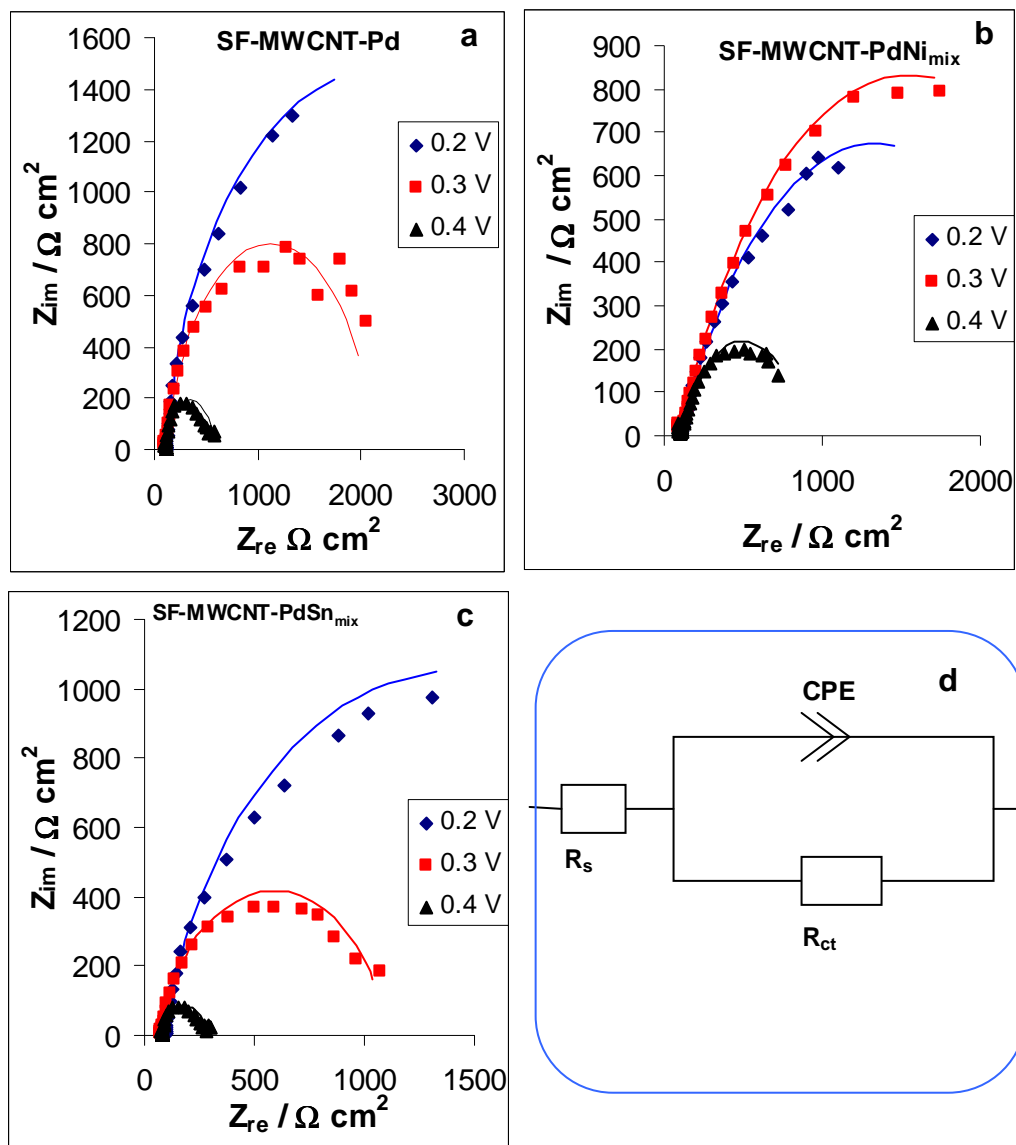


**Figure 4.32:** Nyquist plots obtained during the oxidation of ethylene glycol oxidation at (a) SF-MWCNT-Pd, (b) SF-MWCNT-PdNi<sub>mix</sub>, and SF-MWCNT-PdSn<sub>mix</sub> electrodes and (d) is the equivalent circuit used in fitting the electrochemical impedance circuit.

## Chapter 4: Results and discussion

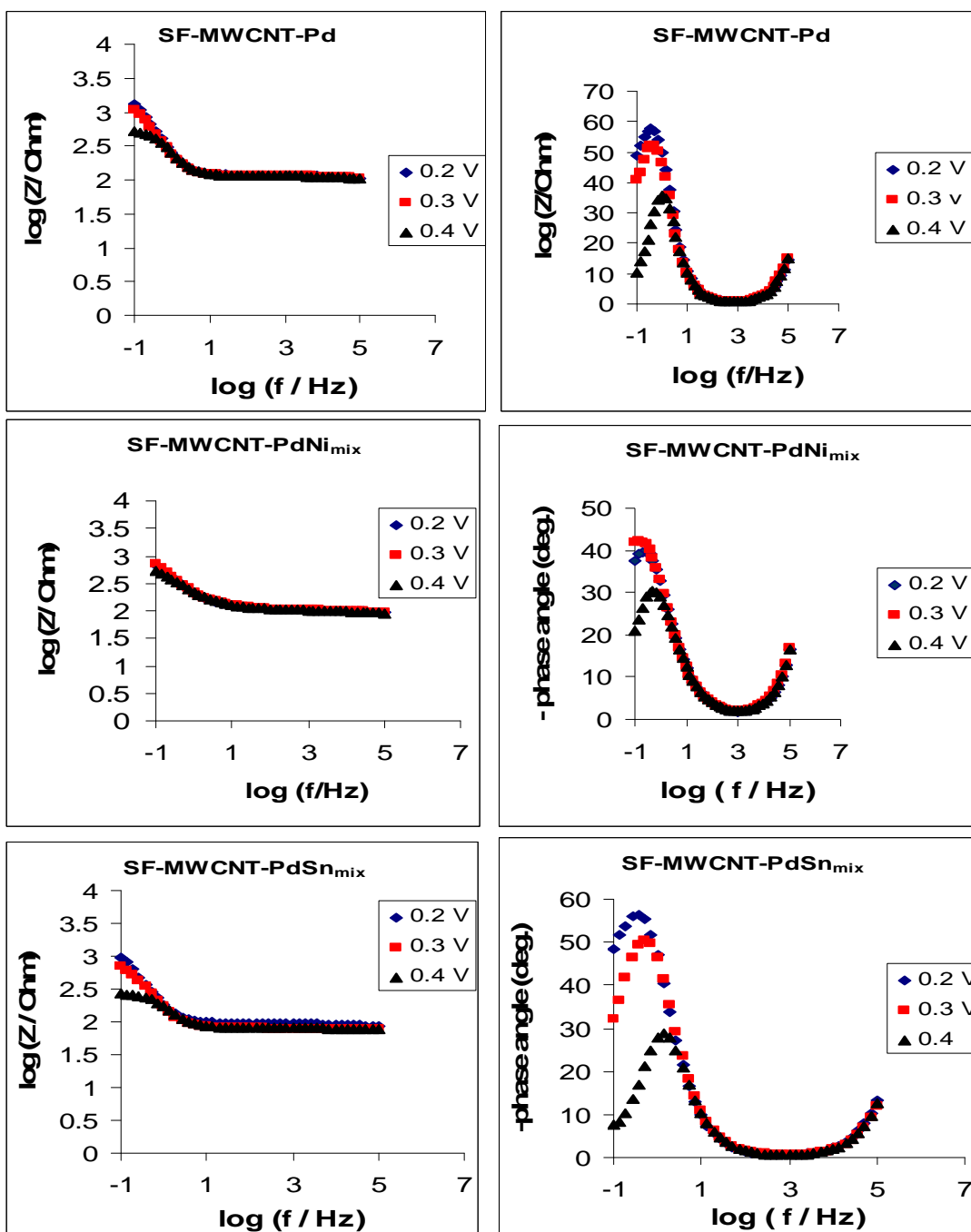


**Figure 4.33:** The Bode plots ( $\log Z$  (a), phase angle (b) vs  $\log f$ ) obtained for the SF-MWCNT-Pd, SF-MWCNT-PdNi<sub>mix</sub>, and SF-MWCNT-PdSn<sub>mix</sub> electrodes in 0.5 M KOH + 0.5 M EG solution at different potentials.

## Chapter 4: Results and discussion

---

The spectra were satisfactorily fitted with the  $R_s(R_{ct}CPE)$  circuit for the SF-MWCNT-Pd, SF-MWCNT-PdNi<sub>mix</sub> and SF-MWCNT-PdSn<sub>mix</sub> electrodes where  $R_s$  is the electrolyte resistance,  $R_{ct}$  is the charge transfer resistance and  $CPE$  is the constant phase element. The impedimetric data are summarised in Table 4.9. The  $R_{ct}$  is related to the reaction kinetics; its values of the SF-MWCNT-Pd and SF-MWCNT-PdSn<sub>mix</sub> electrodes decreased as the potential was increased from low to higher potentials (0.2 to 0.4 V), indicating faster electro-transfer kinetics at higher potentials. However, the SF-MWCNT-PdNi<sub>mix</sub> electrode showed a slightly different pattern where the  $R_{ct}$  at the 0.3 V is higher than obtained at the 0.2 V. As the potential was increased to 0.4 V the  $R_{ct}$  value decreased indicating low charge transfer resistance for the SF-MWCNT-PdNi<sub>mix</sub> electrode towards ethylene glycol oxidation.

## Chapter 4: Results and discussion

---

**Table 4.9:** Impedimetric data for ethylene oxidation on SF-MWCNT-Pd, SF-MWCNT-PdSn<sub>mix</sub> and SF-MWCNT-PdNi<sub>mix</sub> electrodes measured in a 0.5 M ethylene glycol + 0.5 M KOH solution at different potentials (n=9).

Bias potential / V (vsAg AgCl sat'd KCl)	Electrochemical impedimetric parameters			
	R <sub>s</sub> / Ω	R <sub>ct</sub> / kΩ	n	CPE/ F (X10 <sup>2</sup> )
<b>GCE-SF-MWCNT-Pd</b>				
0.2	112.30 ± 1.97	3.84 ± 0.26	0.85 ± 0.02	0.10 ± 0.003
0.3	112.00 ± 1.55	2.02 ± 0.09	0.85 ± 0.02	0.11 ± 0.003
0.4	112.00 ± 1.65	0.48 ± 0.02	0.87 ± 0.03	0.10 ± 0.01
<b>GCE-SF-MWCNT-PdNi<sub>mix</sub></b>				
0.2	100.20 ± 1.76	2.49 ± 0.29	0.63 ± 0.02	0.20 ± 0.01
0.3	101.50 ± 1.87	2.90 ± 0.36	0.67 ± 0.02	0.18 ± 0.01
0.4	98.80 ± 1.89	0.80 ± 0.06	0.63 ± 0.03	0.18 ± 0.01
<b>GCE-SF-MWCNT-PdSn<sub>mix</sub></b>				
0.2	92.00 ± 1.48	2.64 ± 0.16	0.86 ± 0.02	0.14 ± 0.004
0.3	78.60 ± 0.90	1.02 ± 0.03	0.88 ± 0.01	0.15 ± 0.004
0.4	80.00 ± 0.90	0.21 ± 0.01	0.87 ± 0.03	0.01 ± 0.04

### 4.4.8 Effect of varying the concentrations of KOH or ethylene glycol on the voltammetric behaviour

Figure 4.34 shows the linear sweep voltammetric evolutions of different concentrations of ethylene glycol (0.50 – 3.0 M range) in 0.5 M KOH at the SF-MWCNT-PdNi<sub>mix</sub> and SF-MWCNT-PdSn<sub>mix</sub> electrodes at a sweep rate of 1 mV s<sup>-1</sup>. At the SF-MWCNT-PdNi<sub>mix</sub> electrode, the current density increased with an increase in concentration from 0.5 M (14.70 mA cm<sup>-2</sup>) to 0.75 M (16.02 mA cm<sup>-2</sup>). The current density then decreased at 1.0 M to (12.20 mA cm<sup>-2</sup>), increased at 1.25 M (14.11 mA cm<sup>-2</sup>) to 1.50 M (17.04 mA cm<sup>-2</sup>) and then decreased at 1.75 M (13.62 mA cm<sup>-2</sup>), went up at 2.0 M (23.58 mA cm<sup>-2</sup>) and went down at 3.0 M (21.57 mA cm<sup>-2</sup>). The current density at the SF-MWCNT-PdSn<sub>mix</sub> electrode increased in proportion with the ethylene concentrations from 18.44 mA cm<sup>-2</sup> at 0.50 M to 48.80 mA cm<sup>-2</sup> at 3.0 M. The ethylene glycol oxidation peak potential shifted positively with increasing concentration (from -0.127 V at 0.50 M to -0.039 V at 3.0 M) for the SF-MWCNT-PdNi<sub>mix</sub>, and shifted negatively with increasing ethylene glycol concentration (from 0.129 V at 0.50 M to 0.223 V at 3.0 M) for the SF-MWCNT-PdSn<sub>mix</sub>, indicating poorer electron transport

## Chapter 4: Results and discussion

process at the SF-MWCNT-PdNi<sub>mix</sub> than seen at the SF-MWCNT-PdSn<sub>mix</sub> electrode with an increase in ethylene glycol concentration.

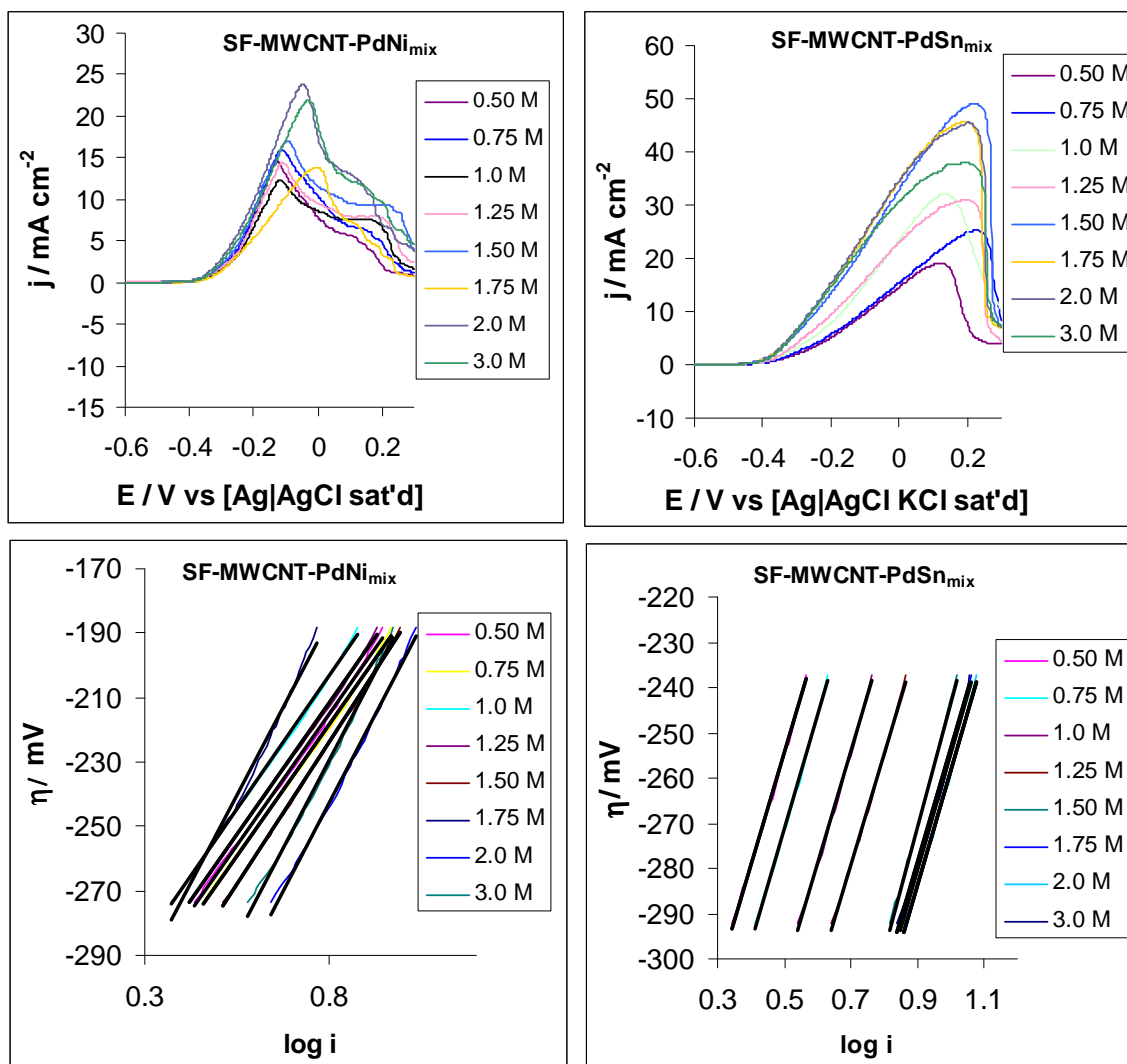


**Figure 4.34:** Linear sweep voltammograms and Tafel plots for ethanol oxidation reaction on the SF-MWCNT-PdNi<sub>mix</sub> and SF-MWCNT-PdSn<sub>mix</sub> in 0.5 M KOH solution containing ethanol solutions of various concentrations at a sweep rate of 1 mV s<sup>-1</sup>.

## Chapter 4: Results and discussion

From the plots of  $\eta$  vs  $\log i$  (exemplified in Figure 4.34), the Tafel slopes (Table 4.10) ranged between 162 - 217 mV dec<sup>-1</sup> for the SF-MWCNT-PdNi<sub>mix</sub> and 243 - 273 mV dec<sup>-1</sup> for SF-MWCNT-PdSn<sub>mix</sub> at all ethylene glycol concentrations studied.

**Table 4.10:** Tafel slopes of the SF-MWCNT-PdNi<sub>mix</sub> and SF-MWCNT-PdSn<sub>mix</sub> electrocatalysts at 0.5 M KOH and different ethylene glycol concentrations.

(EG) Concentration Mol. L <sup>-1</sup>	SF-MWCNT-PdNi <sub>mix</sub>		SF-MWCNT-PdSn <sub>mix</sub>	
	Tafel slope (mV dec <sup>-1</sup> )	R <sup>2</sup>	Tafel slope (mV dec <sup>-1</sup> )	R <sup>2</sup>
0.50	163.07	0.9979	243.09	0.9987
0.75	162.20	0.9985	249.24	0.9979
1.0	165.16	0.9992	246.97	0.9981
1.25	163.14	0.9993	249.19	0.9971
1.50	177.00	0.9996	273.19	0.9979
1.75	218.81	0.9905	258.75	0.9971
2.0	217.06	0.9963	256.32	0.9969
3.0	217.73	0.9952	251.39	0.9960

## Chapter 4: Results and discussion

Figure 4.35 shows the dependence of  $\log j$  vs  $\log$  Ethylene glycol at various low fixed potentials. The reaction orders of ethylene oxidation are summarized in Table 4.11. The reaction order of EG as seen in Table 4.11 for the SF-MWCNT-PdNi<sub>mix</sub> and SF-MWCNT-PdSn<sub>mix</sub> electrocatalysts are approximately 1.

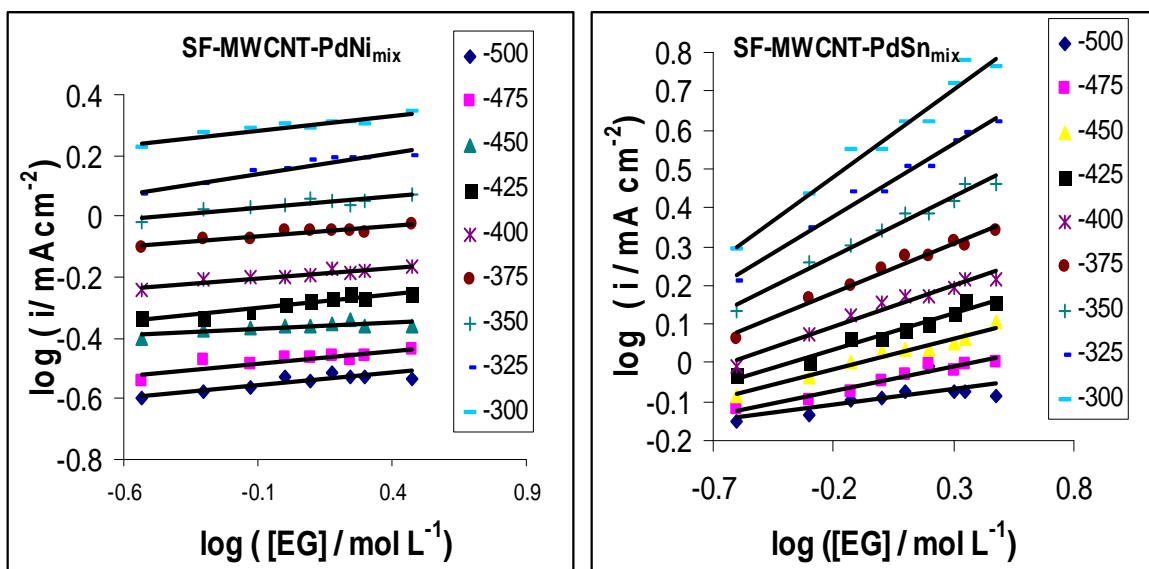


**Figure 4.35:** The log-log plot of current density vs ethylene glycol concentration in 0.5 M KOH obtained at different potentials on SF-MWCNT-PdNi<sub>mix</sub> and SF-MWCNTs-PdSn<sub>mix</sub> electrocatalysts.

## Chapter 4: Results and discussion

---

**Table 4.11:** Reaction orders with respect to  $\text{OH}^-$  and EG for SF-MWCNT-PdNi<sub>mix</sub> and SF-MWCNT-PdSn<sub>mix</sub> electrocatalysts (RSD ~ 5 %).

Potential (mV) (vs. Ag AgCl)	SF-MWCNT-PdNi <sub>mix</sub>		SF-MWCNT-PdSn <sub>mix</sub>	
	OH <sup>-</sup>	EG	OH <sup>-</sup>	EG
-500	0.08	0.70	0.11	0.67
-475	0.08	0.73	0.12	0.72
-450	0.05	0.73	0.16	0.78
-425	0.10	0.70	0.19	0.78
-400	0.07	0.72	0.21	0.88
-375	0.06	0.81	0.25	0.98
-350	0.07	0.85	0.31	1.04
-325	0.13	0.91	0.37	1.07
-300	0.10	0.90	0.46	1.07

Similarly, the impact of different concentrations of the electrolyte (KOH) at constant concentration of ethylene glycol was investigated at

## Chapter 4: Results and discussion

both electrodes. Figure 4.36 exemplifies data obtained at the SF-MWCNT-PdSn<sub>mix</sub> electrode in 0.5 M ethylene glycol solution with different KOH concentrations ranging from 0.50 to 3.0 M. At both electrodes, the peak current increased with increasing KOH concentration from 0.5 M to 3.0 M. The ethylene glycol oxidation peak potential shifted negatively with increasing KOH concentration, indicating that the electrocatalytic oxidation kinetics of ethylene glycol are enhanced by the greater availability of the OH<sup>-</sup> ions in the reaction solution, and hence a higher OH<sup>-</sup> coverage on the electrode surface.

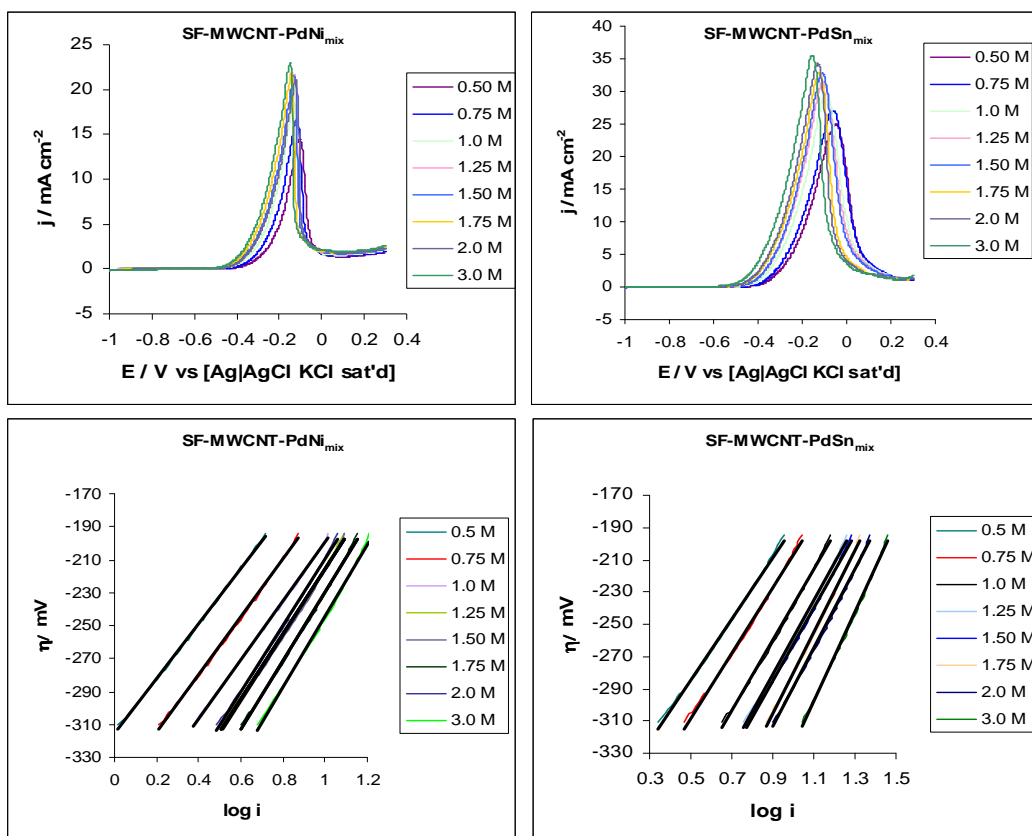


**Figure 4.36:** Linear sweep voltammograms and Tafel plots for ethanol oxidation reaction on the SF-MWCNT-PdNi<sub>mix</sub> and SF-MWCNT-

## Chapter 4: Results and discussion

---

PdSn<sub>mix</sub> in 0.5 M EG solution containing KOH solutions of various concentrations at a sweep rate of 1 mV s<sup>-1</sup>.

From the plots of  $\eta$  vs  $\log j$ , the Tafel slopes (Table 4.12) ranged between 167 - 215 mV dec<sup>-1</sup> for the SF-MWCNT-PdNi<sub>mix</sub> and 190 - 274 mV dec<sup>-1</sup> for SF-MWCNT-PdSn<sub>mix</sub> at all KOH concentrations studied. Figure 4.37 shows the dependence of  $\log j$  vs  $\log C_{\text{KOH}}$  at various low fixed potentials. The reaction order of OH<sup>-</sup> as seen in Table 4.11 for the SF-MWCNT-PdNi<sub>mix</sub> and the SF-MWCNT-PdSn<sub>mix</sub> electrocatalysts are almost in the same range.

## Chapter 4: Results and discussion

---

**Table 4.12:** Tafel slopes of the electrocatalysts at constant 0.5 M EG concentration and various KOH concentrations

<b>(EG) Concentration Mol. L<sup>-1</sup></b>	<b>SF-MWCNT-PdNi<sub>mix</sub></b>		<b>SF-MWCNT-PdSn<sub>mix</sub></b>	
	Tafel slope (mV dec <sup>-1</sup> )	R <sup>2</sup>	Tafel slope (mV dec <sup>-1</sup> )	R <sup>2</sup>
0.50	167.31	0.9993	190.34	0.9973
0.75	174.82	0.9989	202.19	0.9965
1.0	177.26	0.9994	220.42	0.9975
1.25	197.62	0.9989	231.96	0.9977
1.50	198.4	0.9987	226.07	0.9976
1.75	209.4	0.9984	251.56	0.9978
2.0	201.19	0.9985	243.44	0.9976
3.0	215.20	0.9973	274.07	0.9978

## Chapter 4: Results and discussion

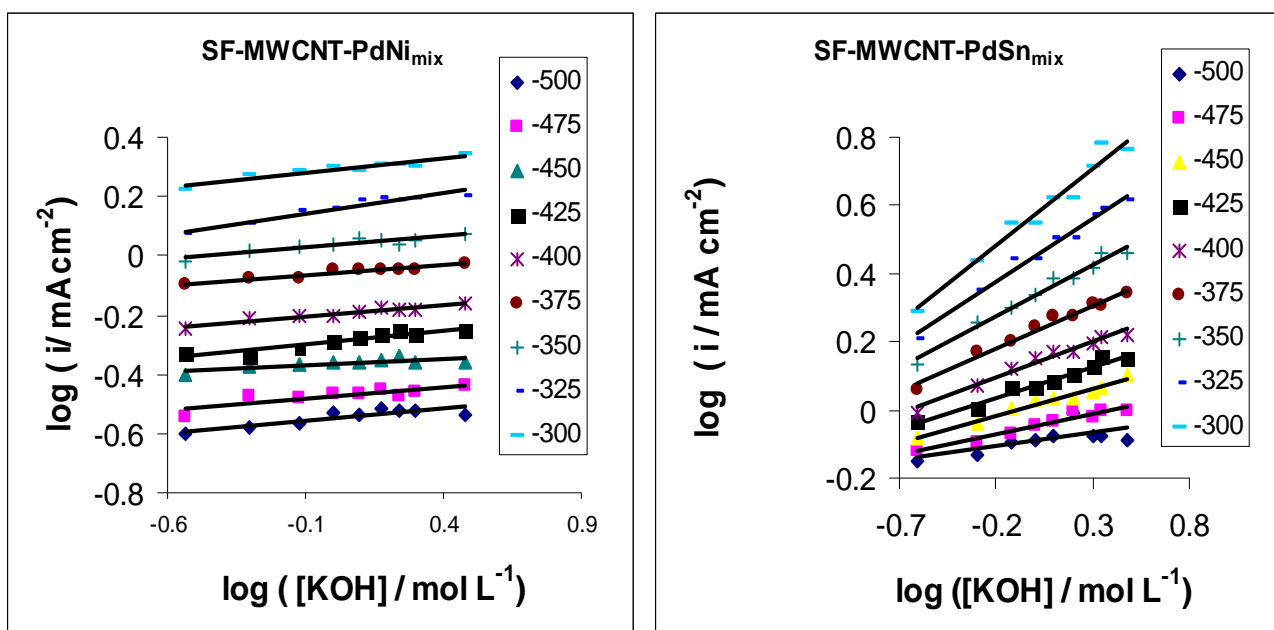


**Figure 4.37:** The log-log plot of current density vs KOH concentration in 0.5 M EG obtained at different potentials on SF-MWCNT-PdNi<sub>mix</sub> and SF-MWCNTs-PdSn<sub>mix</sub> electrocatalysts.

## **CHAPTER FIVE**

# **CONCLUSIONS AND RECOMMENDATIONS**

## Chapter 5: Conclusions and recommendations

---

This study gives the first reported synthesis of Pd, Ni and Sn electrocatalysts supported on sulfonated multi-walled carbon nanotubes ( SF-MWCNT-Pd, SF-MWCNT-Ni and SF-MWCNT-Sn) using a microwave polyol heating technique and the feasibility of using unalloyed electrocatalysts for ethanol and ethylene glycol oxidation in alkaline medium. Structural properties of the prepared electrocatalysts were investigated using FTIR, Raman spectroscopy, XRD, EDX and TEM techniques. The Raman analysis showed similar  $I_D/I_G$  ratios indicating similar defects on the graphite sheet of the MWCNT. The presence of sulphur was also observed on the EDX spectrum. The FTIR analysis showed peaks which are ascribed to the sulfonic acid groups. These confirmed that sulfonic acid groups were indeed incorporated into the MWCNT matrix.

Elemental analysis measurements for the determination of the percentage content of the sulfonic groups on the MWCNT and a study to investigate the effect of varying the sulfonic group percentage would be of great interest. It would also be of great interest to investigate the influence of changing reaction conditions such as the microwave power (W) and reaction time on the structural and catalytic properties of the electrocatalysts. Research on the manipulation of reaction conditions in order to improve electrocatalyst properties is

## Chapter 5: Conclusions and recommendations

---

attracting great interest as it influences their catalytic behaviour and will continue to be of great interest.

The electrocatalysts were successfully evaluated for the electrocatalytic behaviour towards ethanol and ethylene glycol oxidation in alkaline medium using different electrochemical techniques. Although the SF-MWCNT-PdSn<sub>mix</sub> electrocatalyst showed higher current peak density towards ethanol oxidation during the cyclic voltammetry studies, its peak potential occurred at a higher potential as compared to the other electrocatalysts indicating poor electrocatalytic activity. The chronoamperometric results showed that the SF-MWCNTs-PdNi<sub>mix</sub> and SF-MWCNT-PdSn<sub>mix</sub> are more stable than the SF-MWCNT-Pd electrocatalyst, although their performances were comparable towards the end. A linear relationship was observed in all the prepared electrocatalysts from the plot of peak current density ( $I_p$ ) against the scan rate ( $v^{1/2}$ ) showing that the ethanol electrooxidation reaction in alkaline medium is a diffusion controlled process. SF-MWCNT-PdNi<sub>mix</sub> electrocatalyst showed better electrocatalytic activity from the chronopotentiometric studies, with minimal potential oscillation and lower potentials during the polarization process. SF-MWCNT-PdNi<sub>mix</sub> also had a lower Tafel slope as compared to that of SF-MWCNT-PdSn<sub>mix</sub> during ethanol oxidation. EIS results also showed

## Chapter 5: Conclusions and recommendations

---

that the SF-MWCNT-PdNi<sub>mix</sub> has better electrocatalytic activity with a decrease in  $R_{ct}$  as the potential increases. SF-MWCNT-PdNi<sub>mix</sub> is a good candidate electrocatalyst towards the commercialisation of direct ethanol alkaline fuel cells.

The SF-MWCNT-PdSn<sub>mix</sub> electrocatalyst showed higher current peak density towards ethylene glycol oxidation during the cyclic voltammetry studies. Its peak potential occurred at a lower potential as compared to the other electrocatalysts indicating better electrocatalytic activity. The chronoamperometric results also showed that the SF-MWCNTs-PdSn<sub>mix</sub> is more stable than the SF-MWCNT-PdNi<sub>mix</sub> and SF-MWCNT-Pd electrocatalyst. A linear relationship was observed in all the prepared electrocatalysts from the plot of peak current density ( $I_p$ ) against the scan rate ( $v^{1/2}$ ) showing that the ethylene glycol electrooxidation reaction in alkaline medium is a diffusion controlled process. However, the SF-MWCNT-PdNi<sub>mix</sub> electrocatalyst showed better electrocatalytic activity from the chronopotentiometric studies, with minimal potential oscillation and lower potentials during the polarization process. The SF-MWCNTs-PdSn<sub>mix</sub> electrocatalyst had a lower Tafel slope as compared to that of SF-MWCNT-PdNi<sub>mix</sub> during ethylene glycol oxidation. EIS results also

## Chapter 5: Conclusions and recommendations

---

showed that the SF-MWCNT-PdSn<sub>mix</sub> has better electrocatalytic activity with a decrease in  $R_{ct}$  as the potential increases. SF-MWCNT-PdSn<sub>mix</sub> is a good candidate electrocatalyst towards the commercialisation of direct ethylene glycol alkaline fuel cells.

Future work will be needed to fully understand the interaction between the metal nanoparticles when using the mixed bimetallic electrocatalyst. The mechanism for ethanol and ethylene glycol oxidation in alkaline medium is still a subject of some controversy. It is therefore recommended that the in-situ measurement during the ethanol and ethylene glycol oxidation is carried out in alkaline medium in order to fully understand the reaction mechanisms.

## **CHAPTER SIX**

## **REFERENCES**

## Chapter 6: References

---

### 6. References

- [1] M. Winter, R.J. Brodd, *Chem. Rev.*, 101 (2004) 4245-4270.
- [2] V. Bambagioni, M. Bevilacqua, C. Bianchini, J. Filippi, A. Marchionni, F. Vizza, L.Q. Wang, P.K. Shen, *Fuel Cells*, 10 (2010) 582-590.
- [3] E. Antolini, E.R. Gonzalez, *J. Power Sources*, 195 (2010) 3431-3450.
- [4] Y. Chen, L. Zhuang, J. Lu, *Chin. J. Catal.*, 28 (2007) 870-874.
- [5] S.A. Ali, The Role of Fuel Cells in Generating Clean Power and Reducing Greenhouse Gas Emissions In: Syred N, Khalatov A, (Eds), *Advanced Combustion and Aerothermal Technologies: Environmental Protection and Pollution Reductions*, Springer, Netherlands, 2007, pp. 385-403.
- [6] National Fuel Cell Research Center. Fuel Cells Explained: Fuel Cell Types. 2009; Available at: [http://www.nfcr.c.uci.edu/2/FUEL\\_CELL\\_INFORMATION/FCexplained/FC\\_Types.aspx](http://www.nfcr.c.uci.edu/2/FUEL_CELL_INFORMATION/FCexplained/FC_Types.aspx). Accessed 17/07, 2009.
- [7] S.M. Haile, *Mater. Today*, 6 (2003) 24-29.
- [8] F. Barbir, *PEM Fuel Cells : Theory and practice*, Academic Press, Burlington; 2005, pp. 456-xv.

## Chapter 6: References

---

- [9] A. Boudghene Stambouli, E. Traversa, *Renew. Sust. Energ. Rev.*, 6 (2002) 295-304.
- [10] J. Larminie, A. Dicks, M.S. and McDonald, *Fuel cell systems explained*, Wiley New York; 2000.
- [11] L. Carrette, K.A.a.S. Friedrich U., *Chem. Phys. Chem.*, 1 (2000) 163-193.
- [12] R.F. Mann, J.C. Amphlett, B.A. Peppley, C.P. Thurgood, *J. Power Sources*, 161 (2006) 775-781.
- [13] V. Ramani, *Electrochem. Soc. Interface*, 15 (2006) 41-44.
- [14] EG& G services Parsons, Inc. (Ed), *Fuel Cell Handbook*, Fifth ed., Science Application International Corporation, 2000.
- [15] Ceramic fuel cell limited. *Fuel cell facts*. 2009; Available at: [http://www.cfcl.com.au./Fuel\\_Cell\\_Facts/](http://www.cfcl.com.au./Fuel_Cell_Facts/). Accessed 21/07, 2009.
- [16] Holland BJ, Zhu JG, Jamet L. *Fuel cell technology and application*. 2002; Available at: [http://www.itee.uq.edu.au/%7Eaupec/aupec01/111\\_Zhu\\_AUPEC01\\_paper%20revised.pdf](http://www.itee.uq.edu.au/%7Eaupec/aupec01/111_Zhu_AUPEC01_paper%20revised.pdf).
- [17] K. Dircks, 15th International Electric Vehicle Symposium and Exhibition, Proceeding on CD, Brussel, Belgium, 1998, (2004).

## Chapter 6: References

---

- [18] C. Lamy, J.-. Léger, S. Srinivason, Direct methanol fuel cells: From a Twentieth Century Electrochemists Dream to a 21th Century Engineering Technology, Springer, US; 2002.
- [19] C. Lamy, A. Lima, V. LeRhun, F. Delime, C. Coutanceau, J. Léger, *J. Power Sources*, 105 (2002) 283-296.
- [20] H. Wang, C. Xu, F. Cheng *Electrochem. Commun.*, 9 (2007) 1212-1216.
- [21] M.S. Ureta-Zañartu, C. Yáñez, M. Páez, G. Reyes, *J. Electroanal. Chem*, 405 (1996) 159-167.
- [22] C. Coutanceau, L. Demarconnay, C. Lamy, J.-. Léger, *J. Power Sources*, 156 (2006) 14-19.
- [23] L. An, T.S. Zhao, S.Y. Shen, Q.X. Wu, R. Chen, *Int. J. Hydrogen Energy*, 35 (2010) 4329-4335.
- [24] Z.X. Liang, T.S. Zhao, J.B. Xu, L.D. Zhu, *Electrochim. Acta*, 54 (2009) 2203-2208.
- [25] C. Bianchini, P.K. Shen, *Chem. Rev.*, 109 (2009) 4183-4206.
- [26] M.A. Abdel Rahim, H.B. Hassan, R.M. Abdel Hamid, *J. Power Sources*, 154 (2006) 59-65.
- [27] J. Kim, J.-. Park, T. Momma, T. Osaka, *Electrochim. Acta*, 54 (2009) 3412-3418.
-

## Chapter 6: References

---

- [28] A. Morita, S. Ihara, United States Patent and Trademark Office Pre-Grant Publication, (2009).
- [29] J.C. Kotz, P. Treichel, G.C. Weaver (Eds), Chemistry & Chemical Reactivity, 7th ed., Cengage Learning EMEA, 2008.
- [30] G.J.K. Acres, G.A. Hards, *Philosophical Transactions: Mathematical, Phys. and Engineering Sci*, 354 (1996) 1671-1680.
- [31] M. Wang, W. Liu, C. Huang, *Int. J. Hydrogen Energy*, 34 (2009) 2758-2764.
- [32] C. Xu, R. Zeng, P.K. Shen, Z. Wei, *Electrochim. Acta*, 51 (2005) 1031-1035.
- [33] V. Mazumder, S. Sun, *J. Am. Chem. Soc.*, 131 (2009) 4588-4589.
- [34] P.K. Shen, C. Xu, *Electrochem. Commun*, 8 (2006) 184-188.
- [35] C. Xu, P.k. Shen, Y. Liu, *J. Power Sources*, 164 (2007) 527-531.
- [36] F. Hu, C. Chen, Z. Wang, G. Wei, P.K. Shen, *Electrochim. Acta*, 52 (2006) 1087-1091.
- [37] J. Liu, J. Ye, C. Xu, S.P. Jiang, Y. Tong, *Electrochem. Commun*, 9 (2007) 2334-2339.

## Chapter 6: References

---

- [38] M. Jafarian, M.G. Mahjani, H. Heli, F. Gobal, H. Khajehsharifi, M.H. Hamed, *Electrochim. Acta*, 48 (2003) 3423-3429.
- [39] M. Jafarian, R.B. Moghaddam, M.G. Mahjani, F. Gobal, *J. Appl. Electrochem.*, 36 (2006) 913-918.
- [40] M.R. Tarasevich, Z.R. Karichev, V.A. Bogdanovskaya, E.N. Lubnin, A.V. Kapustin, *Electrochem. Commun.*, 7 (2005) 141-146.
- [41] G. Tremiliosi-Filho, E.R. Gonzalez, A.J. Motheo, E.M. Belgsir, J.-. Léger, C. Lamy, *J. Electroanal. Chem*, 444 (1998) 31-39.
- [42] Z. Ogumi, K. Matsuoka, S. Chiba, M. Matsuoka, Y. Iriyama, A.B.E. Takeshi, M. Inaba, *Electrochem.*, 70 (2002) 980-983.
- [43] A.Y. Tsivadze, M.R. Tarasevich, V.N. Andreev, V.A. Bogdanovskaya, *Russ. J. Gen. Chem.*, 77 (2007) 783-789.
- [44] V. Bambagioni, C. Bianchini, J. Filippi, W. Oberhauser, A. Marchionni, F. Vizza, R. Psaro, L. Sordelli, M.L. Foresti, M. Innocenti, *Chem. Sus. Chem.*, 2 (2009) 99-112.
- [45] A.A. El-Shafei, A.M. Abd Elhafeez, H.A. Mostafa, *J. Solid State Electrochem*, (2009) 1-6.
- [46] Y. Su, C. Xu, J. Liu, Z. Liu, *J. Power Sources*, (2009).

## Chapter 6: References

---

- [47] V. Bambagioni, C. Bianchini, A. Marchionni, J. Filippi, F. Vizza, J. Teddy, P. Serp, M. Zhiani, *J. Power Sources*, 190 (2009) 241-251.
- [48] H.T. Zheng, Y. Li, S. Chen, P.K. Shen, *J. Power Sources*, 163 (2006) 371-375.
- [49] F. Jia, K.-. Wong, L. Zhang, *J. Phys. Chem. C*, 113 (2009) 7200-7206.
- [50] F. Ksar, G. Surendran, L. Ramos, B. Keita, L. Nadjo, E. Prouzet, P. Beaunier, A. Hagège, F. Audonnet, H. Remita, *Chem. Mater.*, 21 (2009) 1612-1617.
- [51] R.N. Singh, A. Singh, Anindita, *Carbon*, 47 (2009) 271-278.
- [52] N.M. Suleimanov, S.M. Khantimerov, E.F. Kukovitsky, V.L. Matukhin, *J. Solid State Electrochem.*, 12 (2008) 1021-1023.
- [53] A.M.A. Ouf, A.M. Abd Elhafeez, A.A. El-Shafei, *J. Solid State Electrochem.*, 12 (2008) 601-607.
- [54] J. Lu, S. Lu, D. Wang, M. Yang, Z. Liu, C. Xu, S.P. Jiang, *Electrochim. Acta*, 54 (2009) 5486-5491.
- [55] C. Xu, L. Cheng, P. Shen, Y. Liu, *Electrochem commun.*, 9 (2007) 997-1001.

## Chapter 6: References

---

- [56] J. Bagchi, S.K. Bhattacharya, *Trans. Met. Chem.*, 32 (2007) 47-55.
- [57] D. Chu, J. Wang, S. Wang, L. Zha, J. He, Y. Hou, Y. Yan, H. Lin, Z. Tian, *Catal. Commun*, 10 (2009) 955-958.
- [58] L.D. Zhu, T.S. Zhao, J.B. Xu, Z.X. Liang, *J. Power Sources*, 187 (2009) 80-84.
- [59] I.G. Casella, M.R. Guascito, *Electrochim. Acta*, 45 (1999) 1113-1120.
- [60] C. Xu, Y. Hu, J. Rong, S.P. Jiang, Y. Liu, *Electrochem. Commun*, 9 (2007) 2009-2012.
- [61] F.P. Hu, P.K. Shen, *J. Power Sources*, 173 (2007) 877-881.
- [62] F. Hu, F. Ding, S. Song, P.K. Shen, *J. Power Sources*, 163 (2006) 415-419.
- [63] Q. He, W. Chen, S. Mukerjee, S. Chen, F. Laufek, *J. Power Sources*, 187 (2009) 298-304.
- [64] Z.-. Sun, X.-. Zhang, Y.-. Liang, H.-. Li, *J. Power Sources*, 191 (2009) 366-370.
- [65] C. Xu, Y. Liu, D. Yuan, *I Int. J. Electrochem. Sci.*, (2007) 674-680.

## Chapter 6: References

---

- [66] Y.-. Lee, S.-. Han, K.-. Park, *Electrochem. Commun.*, 11 (2009) 1968-1971.
- [67] R. Pattabiraman, *Appl. Catal., A: General*, 153 (1997) 9-20.
- [68] W. Zhang, P. Sherrell, A.I. Minett, J.M. Razal, J. Chen, *Energy Environ. Sci.*, 3 (2010) 1286-1293.
- [69] C.E. Banks, R.G. Compton, *Analyst*, 131 (2006) 15-21.
- [70] F. Hu, G. Cui, Z. Wei, P.K. Shen, *Electrochem. Commun.*, 10 (2008) 1303-1306.
- [71] H. Meng, F. Xie, P.K. Shen, *ECS Trans*, 1 (2006) 1-9.
- [72] M. Nie, H. Tang, Z. Wei, S.P. Jiang, P.K. Shen, *Electrochem. Commun.*, 9 (2007) 2375-2379.
- [73] H.-. Zheng, Y.-. Li, J.-. Liang, P.-. Shen, *Wuli Huaxue Xuebao, Acta Physico - Chimica Sinica*, 23 (2007) 993-996.
- [74] C.E. Banks, T.J. Davies, G.G. Wildgoose, R.G. Compton, *Chem. Commun.*, (2005) 829-841.
- [75] B.J. Landi, M.J. Ganter, C.D. Cress, R.A. DiLeo, R.P. Raffaele, *Energy Environ. Sci.*, 2 (2009) 638-654.
- [76] A. Chou, T. Böcking, N.K. Singh, J.J. Gooding, *Chem. Commun.*, (2005) 842-844.

## Chapter 6: References

---

- [77] K.I. Ozoemena, J. Pillay, T. Nyokong, *Electrochem. Commun.*, 8 (2006) 1391-1396.
- [78] J. Pillay, K.I. Ozoemena, *Electrochim. Acta*, 52 (2007) 3630-3640.
- [79] K.I. Ozoemena, D. Nkosi, J. Pillay, *Electrochim. Acta*, 53 (2008) 2844-2851.
- [80] A.T. Chidembo, K.I. Ozoemena, B.O. Agboola, V. Gupta, Wildgoose, Gregory G. and Compton, Richard G., *Energy Environ. Sci.*, 3 (2010) 228 - 236.
- [81] D. Nkosi, J. Pillay, K.I. Ozoemena, K. Nouneh, M. Oyama, *Phys. Chem. Chem. Phys.*, 12 (2010) 604-613.
- [82] S.A. Mamuru, K.I. Ozoemena, *Electrochem. Commun.*, (2010).
- [83] A. Hirsch, *Angewandte Chemie*, 114 (2002) 1933-1939.
- [84] S. Iijima, *Physica B: Condens. Matter.*, 323 (2002) 1-5.
- [85] H. Nalwa (Ed), *Nanostructured Materials and Nanotechnology, Concise Edition ed.*, Academic Press, San Diego, 2002.
- [86] R. Saito, M. Fujita, G. Dresselhaus, M.S. Dresselhaus, *Appl. Phys. Lett.*, 60 (1992) 2204-2206.

## Chapter 6: References

---

- [87] A.Y. Kasumov, H. Bouchiat, B. Reulet, O. Stephan, I.I. Khodos, Y.B. Gorbatov, C. Colliex, *Europhys. Lett.*, 43 (1998) 89-94.
- [88] S. Yin, P.K. Shen, S. Song, S.P. Jiang, *Electrochim. Acta*, 54 (2009) 6954-6958.
- [89] M.P. Siswana, K.I. Ozoemena, T. Nyokong, *Electrochim. Acta*, 52 (2006) 114-122.
- [90] Z.Q. Tian, Y.M. Liang, P.K. Shens, *J. Phys. Chem. B*, 110 (2006) 5343-5350.
- [91] C.Y. Du, T.S. Zhao, Z.X. Liang, *J. Power Sources*, 176 (2008) 9-15.
- [92] K.A. Friedrich, K.P. Geyzers, A.J. Dickinson, U. Stimming, *J. Electroanal. Chem.*, 524-525 (2002) 261-272.
- [93] F. Vigier, C. Coutanceau, A. Perrard, E.M. Belgsir, C. Lamy, *J. Appl. Electrochem.*, 34 (2004) 439-446.
- [94] R.N. Singh, A. Singh, Anindita, *J. Solid State Electrochem.*, 13 (2009) 1259-1265.
- [95] G. Garnweitner, M. Niederberger, *J. Mater. Chem.*, 18 (2008) 1171-1182.
- [96] W.X. Chen, J.Y. Lee, Z. Liu, *Chem. Commun.*, 8 (2002) 2588-2589.

## Chapter 6: References

---

- [97] A. Sarkar, A.V. Murugan, A. Manthiram, *Fuel Cells*, 10 (2010) 375-383.
- [98] S.-. Park, J.-. Chang, K.H. Young, S.K. Dae, H.J. Sung, S.H. Jin, *Catalysis Surveys from Asia*, 8 (2004) 91-110.
- [99] H. Bönemann, W. Brijoux, R. Brinkmann, E. Dinjus, T. Joußen, B. Korall, *Angewandte Chemie* (International Edition in English), 30 (1991) 1312-1314.
- [100] L. Demarconnay, S. Brimaud, C. Coutanceau, J.-. Léger, *J. Electroanal. Chem.*, 601 (2007) 169-180.
- [101] S. Brimaud, C. Coutanceau, E. Garnier, J.-. Léger, F. Gérard, S. Pronier, M. Leoni, *J. Electroanal. Chem*, 602 (2007) 226-236.
- [102] X. Wang, J. Liao, C. Liu, W. Xing, T. Lu, *Electrochem. Commun.*, 11 (2009) 198-201.
- [103] C. Yang, X. Hu, D. Wang, C. Dai, L. Zhang, H. Jin, S. Agathopoulos, *J. Power Sources*, 160 (2006) 187-193.
- [104] A.O. Neto, R.R. Dias, M.M. Tusi, M. Linardi, E.V. Spinacé, *J. Power Sources*, 166 (2007) 87-91.
- [105] C. Oliver Kappe, *Chem. Soc. Rev.*, 37 (2008) 1127-1139.
- [106] A. Vadivel Murugan, A.K. Viswanath, V. Ravi, B.A. Kakade, V. Saaminathan, *Appl. Phys. Lett.*, 89 (2006) 123120-123123.

## Chapter 6: References

---

- [107] A. Sarkar, A.V. Murugan, A. Manthiram, *Langmuir*, 26 (2010) 2894-2903.
- [108] J. Zhao, W. Chen, Y. Zheng, X. Li, Z. Xu, *J. Mater. Sci.*, 41 (2006) 5514-5518.
- [109] S. Komarneni, D. Li, B. Newalkar, H. Katsuki, A.S. Bhalla, *Langmuir*, 18 (2002) 5959-5962.
- [110] C. Leonelli, T.J. Mason, *Chemical Engineering and Processing: Process Intensification*, 49 (2010) 885-900.
- [111] J. Haber, J.H. Block, B. Delmon, *Pure & Appl. Chem.*, 67 (1995) 1257-1306.
- [112] Y. Shi, J. Liang, Q. Liu, X. Chen, *Science in China, Series A: Mathem., Phys., Astron.*, 41 (1998) 191-197.
- [113] B.D. Cullity, *Elements of X-ray Diffraction*, Addison Wesley Publication Company Inc., United State of America; 1956.
- [114] Grant P. Technical note 13, X-ray diffraction. 2004; Available at:  
<http://www.research.philips.com/technologies/projects/matanalysis/downloads/xrd.pdf>. Accessed November, 2010.
- [115] B.R. Rehani, P.B. Joshi, K.N. Lad, A. Pratap, *Indian J. Pure Appl. Phys.*, 44 (2006) 157-161.

## Chapter 6: References

---

- [116] V. Uvarov, I. Popov, *Mater. Charact.*, 58 (2007) 883-891.
- [117] Wikipedia. Transmission Electron Microscopy. 2011; Available at: [http://en.wikipedia.org/wiki/Transmission\\_electron\\_microscopy](http://en.wikipedia.org/wiki/Transmission_electron_microscopy). Accessed March/ 7, 2011.
- [118] P.S. Kounaves, Voltammetric techniques In: Settle FA, (Ed), Handbook of instrumental techniques for analytical chemistry, illustrated ed., Prentice Hall, New Jersey, 1997, pp. 712-713.
- [119] D. Armstrong (Ed), Free Radical and Antioxidant Protocols, Humana Press Inc, New Jersey, 1998.
- [120] Photometrics I. Energy Dispersive X-ray Spectroscopy (EDS). 2010; Available at: <http://www.photometrics.net/eds.html>. Accessed October/ 20, 2010.
- [121] Wikipedia. Raman Spectroscopy. 2011; Available at: [http://en.wikipedia.org/wiki/Raman\\_spectroscopy](http://en.wikipedia.org/wiki/Raman_spectroscopy). Accessed March, 2011.
- [122] HORIBA Scientific. 2010; Available at: <http://www.horiba.com/scientific/products/raman-spectroscopy/applications/>. Accessed 25/ 05, 2010.
- [123] Princeton Instruments. Raman Spectroscopy Basics. 2008; Available at: <http://www.princetoninstruments.com/library2/index.php?option=c>
-

## Chapter 6: References

---

[om\\_docman&task=cat\\_view&gid=15&Itemid=2.](#) Accessed  
September, 2010.

[124] E. Smith, G. Dent, *Modern Raman Spectroscopy, A practical approach*, John Wiley & Sons Ltd, Chichester; 2005.

[125] G. Kalita, S. Adhikari, H.R. Aryal, R. Afre, T. Soga, M. Sharon, M. Umeno, *Current Appl. Phys.*, 9 (2009) 346-351.

[126] HORIBA Jobin Yvon. Carbon Nanotubes - What information does Raman Microscopy bring? 2005; Available at: [www.jobinyvon.com](http://www.jobinyvon.com). Accessed March/ 7, 2011.

[127] W.S. Kim, S.Y. Moon, S.Y. Bang, B.G. Choi, H. Ham, T. Sekino, K.B. Shim, *Appl. Phys. Lett.*, 95 (2009).

[128] DeltaNu. Characterization of Carbon Nanotubes (CNTs) with Raman Spectroscopy, DeltaNu Application Note. 2011; Available at: [www.deltanu.com](http://www.deltanu.com). Accessed March/ 7, 2011.

[129] S. Costa, E. Borowiak-Palen, M. Kruszyńska, A. Bachmatiuk, R.J. Kaleńczuk, *Mater. Sci.- Poland*, 26 (2008) 433-441.

[130] L.G. Wade, *Organic Chemistry*, 5th ed., Prentice Hall, New Jersey; 2003, pp. 490-538.

[131] P.S. Kalsi, *Spectroscopy of organic compounds*, Wiley Eastern Limited, New Dehli; 1993, pp. 61-164.

## Chapter 6: References

---

[132] J. Coates, Interpretation of Infrared Spectra, a practical approach In: Meyers RA, (Ed), Encyclopedia of Analytical Chemistry, John Wiley & Sons Ltd, Chichester, 2000, pp. 10815-10837.

[133] Tiginyana I, Langa S, Foell H, Ursachi V. Electrochemical cells and Potentiostats. 2009; Available at: <http://www.porous-35.com/electrochemistry-semiconductors-10.html>, 2010.

[134] J. Wang, Analytical Electrochemistry, VCH publishers, New York; 1994.

[135] P. Atkins, J. de Paula (Eds), Physical Chemistry, 7th ed., Oxford University Press Inc, New York, 2002.

[136] Bott AW. Mass transport. 1996; Available at: [www.currentseparations.com/issues/14-34/cs14-34d.pdf](http://www.currentseparations.com/issues/14-34/cs14-34d.pdf). Accessed December/ 11, 2010.

[137] A.J. Bard, L.R. Faulker, Electrochemical Methods: Fundamentals and Application, 2nd ed., John Wiley & Sons, Hoboken, NJ; 2001.

[138] P.A. Christensons, A. Hamnett (Eds), Techniques and Mechanisms in Electrochemistry, 1st ed., Blackie Academic and Professional, London, 1994.

[139] J.E.B. Randles, *Trans. Faraday Soc.*, 44 (1948) 322-327.

## Chapter 6: References

---

[140] W.R. Heineman, P.T. Kissinger, Laboratory Techniques In: Kissinger PT, Heineman WR, (Eds), *Electroanalytical Chemistry*, 2nd ed., Marcel Dekker Inc, New York, 1996.

[141] E.R. Brown, R.F. Large, *Electrochemical Methods* In: Wessberger A, Rossiter B, (Eds), *Physical Methods in Chemistry*, Eds ed., Wiley-Interscience, New York, 1971.

[142] H. Dodziuk, *Cyclodextrins and their complexes : Chemistry, analytical methods ; applications, illustrated ed.*, Wiley - VCH, New York; 2006.

[143] Courtesy LD Technologies. The Chronoamperometry: The Cottrell's Equation. 2008; Available at: [www.menlatech.com/docs/chromatology.pdf](http://www.menlatech.com/docs/chromatology.pdf). Accessed December/11, 2010.

[144] Autolab Metrohm. Autolab application note 11, *Electrochemical Impedance Spectroscopy: Basic principles*. Available at: <http://www.ecochemie.nl/Applications/>. Accessed November/4, 2010.

[145] V.F. Lvovich, *Electrochem. Soc. Interface*, 18 (2009) 62-66.

[146] P. Bommersbach, M. Mohamedi, D. Guay, J. *Electrochem. Soc.*, 154 (2007) B876-B882.

[147] G. Wu, L. Li, B.-. Xu, *Electrochim. Acta*, 50 (2004) 1-10.

## Chapter 6: References

---

- [148] A. Amirudin, D. Thieny, *Prog. in Organic Coatings*, 26 (1995) 1-28.
- [149] Gamry Instruments. Basics of Electrochemical Impedance Spectroscopy. 2010; Available at: [http://www.gamry.com/App\\_Notes/EchemImpedanceSpecs.htm](http://www.gamry.com/App_Notes/EchemImpedanceSpecs.htm). Accessed December/ 11, 2010.
- [150] P.M. Gomadam, J.W. Weidner, *Int. J. Energy Res.*, 29 (2005) 1133-1151.
- [151] R.A. Durst, A.J. Bäumner, R.W. Murray, R.P. Buck, C.P. Andrieux, *Pure Appl.Chem.*, 69 (1997) 1317-1323.
- [152] Y. Zhao, X. Yang, J. Tian, F. Wang, L. Zhan, *Int. J. Hydrogen Energy*, 35 (2010) 3249-3257.
- [153] X. Li, W.-. Chen, J. Zhao, W. Xing, Z.-. Xu, *Carbon*, 43 (2005) 2168-2174.
- [154] P. Kim, J.B. Joo, W. Kim, J. Kim, I.K. Song, J. Yi, *J. Power Sources*, 160 (2006) 987-990.
- [155] E.B. Fox, H.R. Colon-Mercado, *Int. J. Hydrogen Energy*, 35 (2010) 3280-3286.
- [156] Z.-. Sun, X.-. Zhang, R.-. Liu, Y.-. Liang, H.-. Li, *J. Power Sources*, 185 (2008) 801-806.

## Chapter 6: References

---

- [157] A. Yasuda, N. Kawase, W. Mizutani, *J. Phys. Chem. B*, 106 (2002) 13294-13298.
- [158] A. Yasuda, N. Kawase, T. Matsui, T. Shimidzu, C. Yamaguchi, H. Matsui, *React. Funct. Polym*, 41 (1999) 13-19.
- [159] V. Rao, Hariyanto, C. Cremers, U. Stimming, *Fuel Cells*, 7 (2007) 417-423.
- [160] D. Yuan, C. Xu, Y. Liu, S. Tan, X. Wang, Z. Wei, P.K. Shen, *Electrochem. Commun.*, 9 (2007) 2473-2478.
- [161] S.S. Gupta, S. Singh, J. Datta, *Mater. Chem. Phys.*, 116 (2009) 223-228.
- [162] A.N. Correia, L.H. Mascaró, S.A.S. Machado, L.A. Avaca, *Electrochim. Acta*, 42 (1997) 493-495.
- [163] Khrushcheva, E.L and Tarasevich, M.R, *Russ. Chem. Rev.*, 47 (1978) 416.
- [164] Z. Bai, L. Yang, L. Li, J. Lv, K. Wang, J. Zhang, *J. Phys. Chem. C*, 113 (2009) 10568-10573.
- [165] R.S. Jayashree, J.S. Spendelow, J. Yeom, C. Rastogi, M.A. Shannon, P.J.A. Kenis, *Electrochim. Acta*, 50 (2005) 4674-4682.

## Chapter 6: References

---

- [166] A.N. Gavrilov, E.R. Savinova, P.A. Simonov, V.I. Zaikovskii, S.V. Cherepanova, G.A. Tsirlina, V.N. Parmon, *Phys. Chem. Chem. Phys.*, 9 (2007) 5476-5489.
- [167] F.C. Nart, W. Vielstich, W. in Vielstich, A. Lamm, H.A. Gasteiger (Eds), *Handbook of Fuel Cells : Electrocatalysis*, Eds ed., Wiley, West Sussex, 2003, pp. 308-315.
- [168] T. Vidaković, M. Christov, K. Sundmacher, *Electrochim. Acta*, 52 (2007) 5606-5613.
- [169] R.N. Singh, Anindita, Madhu, *J. Solid State Electrochem.*, 14 (2010) 2113-2120.
- [170] R.N. Singh, A. Singh, Anindita, *Int. J. Hydrogen Energy*, 34 (2009) 2052-2057.
- [171] R.B. de Lima, H. Varela, *Gold Bulletin*, 41 (2008) 15-22.
- [172] W. Zhou, Z. Zhou, S. Song, W. Li, G. Sun, P. Tsiakaras, Q. Xin, *Appl. Catal. B: Environmental*, 46 (2003) 273-285.
- [173] A.V. Tripković, K.D. Popović, J.D. Momčilović, D.M. Dražić, *J Electroanal. Chem*, 418 (1996) 9-20.
- [174] S.C.S. Lai, S.E.F. Kley, V. Rosca, M.T.M. Koper, *J. Phys. Chem., C*, 112 (2008) 19080-19087.

## Chapter 6: References

---

- [175] H. Wang, Z. Jusys, R.J. Behm, *J. Power Sources*, 154 (2006) 351-359.
- [176] W. Chen, J. Kim, S. Sun, S. Chen, *Phys. Chem. Chem. Phys.*, 8 (2006) 2779-2786.
- [177] M.-. Morin, C. Lamy, J.-. Léger, J.-. Vasquez, A. Aldaz, *J Electroanal. Chem*, 283 (1990) 287-302.
- [178] J. Huang, Z. Liu, C. He, L.M. Gan, *J. Phys. Chem B*, 109 (2005) 16644-16649.
- [179] W. Chen, J. Kim, S. Sun, S. Chen, *Langmuir*, 23 (2007) 11303-11310.
- [180] N.W. Maxakato, K.I. Ozoemena, C.J. Arendse, *Electroanal*, 22 (2010) 519-529.
- [181] O.A. Petrii, R.R. Nazmutdinov, M.D. Bronshtein, G.A. Tsirlina, *Electrochim. Acta*, 52 (2007) 3493-3504.
- [182] C. Xu, Z. Tian, P. Shen, S.P. Jiang, *Electrochim. Acta*, 53 (2008) 2610-2618.
- [183] J.N. Soderberg, A.C. Co, A.H.C. Sirk, V.I. Birss, *J. Phys. Chem B*, 110 (2006) 10401-10410.

## Chapter 6: References

---

- [184] M.E. Orazem, B. Tribollet (Eds), *Methods for Representing Impedance*, in *Electrochemical Impedance Spectroscopy*, Wiley, Hoboken, NJ, USA, 2008.
- [185] N.S. Mathebula, J. Pillay, G. Toschi, J.A. Verschoor, K.I. Ozoemena, *Chem. Commun.*, (2009) 3345-3347.
- [186] J. Pillay, K.I. Ozoemena, R.T. Tshikhudo, R.M. Moutloali, *Langmuir*, 26 (2010) 9061-9068.
- [187] K.I. Ozoemena, N.S. Mathebula, J. Pillay, G. Toschi, J.A. Verschoor, *Phys. Chem. Chem. Phys.*, 12 (2010) 345-357.
- [188] S.A. Mamuru, K.I. Ozoemena, T. Fukuda, N. Kobayashi, *J. Mater. Chem.*, In press (2010).
- [189] L.-.H. Leung, M.J. Weaver, *J. Phys. Chem.*, 92 (1988) 4019-4022.
- [190] B. Wieland, J.P. Lancaster, C.S. Hoaglund, P. Holota, W.J. Tornquist, *Langmuir*, 12 (1996) 2594-2601.
- [191] A. Dailey, J. Shin, C. Korzeniewski, *Electrochim. Acta*, 44 (1998) 1147-1152.
- [192] R.B. De Lima, V. Paganin, T. Iwasita, W. Vielstich, *Electrochim. Acta*, 49 (2003) 85-91.

## Chapter 6: References

---

[193] K. Matsuoka, Y. Iriyama, T. Abe, M. Matsuoka, Z. Ogumi,  
*Electrochim. Acta*, 51 (2005) 1085-1090.

[194] Z. Liu, L. Hong, *J. Appl. Electrochem.*, 37 (2007) 505-510.

### APPENDIX

Oral and poster presentations resulting from this thesis are:

#### **Poster Presentation:**

*"Microwave synthesized MWCNT/Pd-M (Ni.Sn) electrocatalyst for ethanol oxidation in alkaline medium", T Ramulifho, K I Ozoemena, M Modibedi, M Mathe, L van der Merwe, International Workshop on Advanced Materials and Technologies for Global Energy and Environmental Challenges, CSIR , South Africa, 6-8 December **2010***

#### **Oral Presentations:**

- *"Microwave-synthesised MWCNT/Pd-M (M = Ni, Sn) nanocomposites as efficient anode catalysts for ethanol oxidation in alkaline medium", Tendamudzimu Ramulifho and Kenneth I. Ozoemena, Mmalewane. Modibedi, Mkhulu K. Mathe and Liezel van der Merve, 10th International Symposium on Kinetics in Analytical Chemistry, UWC, Cape Town, 2-4 December **2009**.*

## Appendix

---

- *"Multi-walled carbon nanotubes / Pd-M (M= Ni, Sn) nanocomposites as efficient electrocatalyst for the oxidation of ethanol in alkaline medium"*, Tendamudzimu Ramulifho and Kenneth I. Ozoemena, Mmalewane. Modibedi. SA/GERMANY Science, Research and Technology Cooperation Agreement, Research project period: 2008-2010, End of program Workshop, 7 - 8 September, Rhodes University, **2010**.
- *"Carbon Nanotube-Modified Metallophthalocyanines and Metal Nanoparticles as Efficient Platforms for Fuel Cells"* Kenneth I. Ozoemena, Tendamudzimu Ramulifho, Solomon A. Mamuru, Mmalewane Modibedi, and Mkhulu K. Mathe. The 61<sup>st</sup> Annual Meeting of the International Society of Electrochemistry, 26 September – 01 October, France, **2010**.
- *Nanocarbon-Supported Electroactive Nanostructures in Energy Storage and Conversion Systems*, K. Ozoemena, T. Ramulifho, S. A. Mamuru, A. S. Adekunle, M. Modibedi and M.K. Mathe, International Workshop on Advanced Materials and Technologies for Global Energy and Environmental Challenges, CSIR South Africa, 6-8 December **2010**